JPL Publication 93-26, Vol. 3

Summaries of the Fourth Annual JPL Airborne Geoscience Workshop October 25–29, 1993

Volume 3. AIRSAR Workshop

Jakob van Zyl
Editor

October 25, 1993

National Aeronautics and
Space Administration

Jet Propulsion Laboratory
California Institute of Technology
Pasadena, California

This publication was prepared by the Jet Propulsion Laboratory, California Institute of Technology, under a contract with the National Aeronautics and Space Administration.

ABSTRACT

This publication contains the summaries for the Fourth Annual JPL Airborne Geoscience Workshop, held in Washington, D. C. on October 25–29, 1993. The main workshop is divided into three smaller workshops as follows:

- The Airborne Visible/Infrared Imaging Spectrometer (AVIRIS) workshop, on October 25–26. The summaries for this workshop appear in Volume 1.
- The Thermal Infrared Multispectral Scanner (TIMS) workshop, on October 27. The summaries for this workshop appear in Volume 2.
- The Airborne Synthetic Aperture Radar (AIRSAR) workshop, on October 28–29. The summaries for this workshop appear in Volume 3.

FOREWORD

In the text and the figure captions of some of the papers for the AVIRIS and AIRSAR Workshops, reference is made to color slides. A pocket containing a set of all the slides mentioned in those papers appears at the end of this volume.

CONTENTS

Volume 1: AVIRIS Workshop

Volume 2: TIMS Workshop

Volume 3: AIRSAR Workshop

N95- 23939

INTERFEROMETRIC SYNTHETIC APERTURE RADAR IMAGERY OF THE GULF STREAM

T. L. Ainsworth[1,2], M. E. Cannella[1,3], R. W. Jansen[1], S. R. Chubb[1],
R. E. Carande[4], E. W. Foley[5], R. M. Goldstein[4] and G. R. Valenzuela[1]

[1] Naval Research Laboratory, Washington, D.C. 20375;
[2] AlliedSignal Technical Services Corporation, Camp Springs, MD 20746;
[3] Syracuse University, Syracuse, NY 13244;
[4] Jet Propulsion Laboratory, California Institute of Technology, Pasadena, CA 91109;
[5] Naval Surface Weapons Center, Bethesda, MD 20084

1. INTRODUCTION

The advent of interferometric synthetic aperture radar (INSAR) imagery brought to the ocean remote sensing field techniques used in radio astronomy. Whilst details of the interferometry differ between the two fields, the basic idea is the same: Use the phase information arising from positional differences of the radar receivers and/or transmitters to probe remote structures. The success of airborne INSAR methods (Goldstein *et al.*, 1987) provided ample incentive to investigate numerous other applications, *e.g.* topographic mapping (Zebker *et al.*, 1986), surface ocean currents (Goldstein *et al.*, 1989) and internal waves (Thompson *et al.*, 1993). In this paper, we apply for the first time INSAR methods to the Gulf Stream boundary. A primary advantage of the INSAR technique when applied to ocean surfaces is the ability to observe the motion of surface scatterers.

The interferometric image is formed from two complex synthetic aperture radar (SAR) images. These two images are of the same area but separated in time. Typically the time between these images is very short — approximately 50 msec for the L-band AIRSAR. During this short period the radar scatterers on the ocean surface do not have time to significantly decorrelate. Hence the two SAR images will have the same amplitude, since both obtain the radar backscatter from essentially the same object. Although the ocean surface structure does not significantly decorrelate in 50 msec., surface features do have time to move. It is precisely the translation of scattering features across the ocean surface which gives rise to phase differences between the two SAR images. This phase difference is directly proportional to the range velocity of surface scatterers. The constant of proportionality is dependent upon the interferometric mode of operation. In our case, the total phase difference between the two SAR images is

$$\Delta\phi = \frac{2\pi\ell}{v_{air}\lambda} u_{range} \quad ,$$

where ℓ is the spacing between the radar receivers, λ is the radar wavelength, v_{air} is the aircraft velocity and u_{range} is the component of the scatterer's velocity in the range direction. The motion of the scatterers may arise from ocean currents, internal wave motions, winds or most generally all of the above. Identifying these different components of u_{range}, without recourse to additional information, is a formidable task.

One immediately sees several possible limitations to the INSAR technique. The time between images must be short enough that the ocean surface does not decorrelate, otherwise the phase difference contains no new information. Also the time between images must be long enough so that the surface features have time to move and thus provide a phase difference. We implicitly require that the SAR images have been corrected for the aircraft sidewards drift and yaw, both of which will produce (unwanted) phase differences. Therefore as a practical matter the phase difference arising from the surface motion should be greater than the errors in compensating for aircraft motion — the signal-to-noise ratio should be large. Perhaps more irksome than the above is the problem of large surface velocities, when the phase difference is greater than 2π. The interferometric image determines the phase differences modulo 2π, therefore many velocities map onto the same phase difference. Typically, range velocities of scatterers of approximately 0.0 m/sec., 2.7 m/sec., 5.4 m/sec., *etc.* all yield a zero phase difference in the interferometric image. One possible means of lifting this phase ambiguity is to use multi-frequency and/or multi-baseline interferometry. These methods have been discussed by Carande, 1992 and Carande *et al.*, 1991. Therefore the interpretation of INSAR images may require other information, additional assumptions and/or modeling.

2. GULF STREAM IMAGES

The particular interferometric images which we have analyzed are from the 1990 AIRSAR flight of July 20th, previously identified as G-Stream NI 120-1 (Kobrick, 1990; Valenzuela *et al.*, 1991). The complex interferometric image is the product of one complex SAR image with the complex conjugate of the other. Therefore the amplitude of the INSAR image is the product of the individual SAR image amplitudes. The phase of the INSAR image is the phase difference (modulo 2π) between the two SAR images. The amplitude and phase of the INSAR image are shown in Figure 1. The amplitude image shows no detailed structure and provides only hints of large features. In contrast the phase image clearly depicts the Gulf Stream boundary. The Gulf Stream boundary is the one large feature that may be seen in the amplitude image. In addition, the phase image clearly shows the Research Vessel Cape Henlopen, her wake and other smaller surface structures. We have interpreted the dark-light banding as internal wave motion. The orientation of these images is independently verified by the ship's wake and log — she was southbound at 10 knots when the INSAR image was taken.

This comparison of INSAR phase and amplitude images may downplay too much the value of complex SAR imagery. Milman *et al.*, 1990 have developed and applied ambiguity function techniques to complex SAR images to obtain information about surface velocities. However, the amplitude of SAR images conveys no relevant information about velocities (other than velocity bunching effects) and, as seen in Figure 1, little information about small-scale surface features.

The complementary nature of SAR and INSAR images produces a powerful oceanographic remote sensing tool. INSAR is sensitive to surface velocities whereas SAR amplitudes depend strongly on the surface shape. Presumably these two features (shape and velocity) are, in at least some cases, correlated. Therefore employing the additional information which interferometry provides will assist the interpretation of the region surveyed.

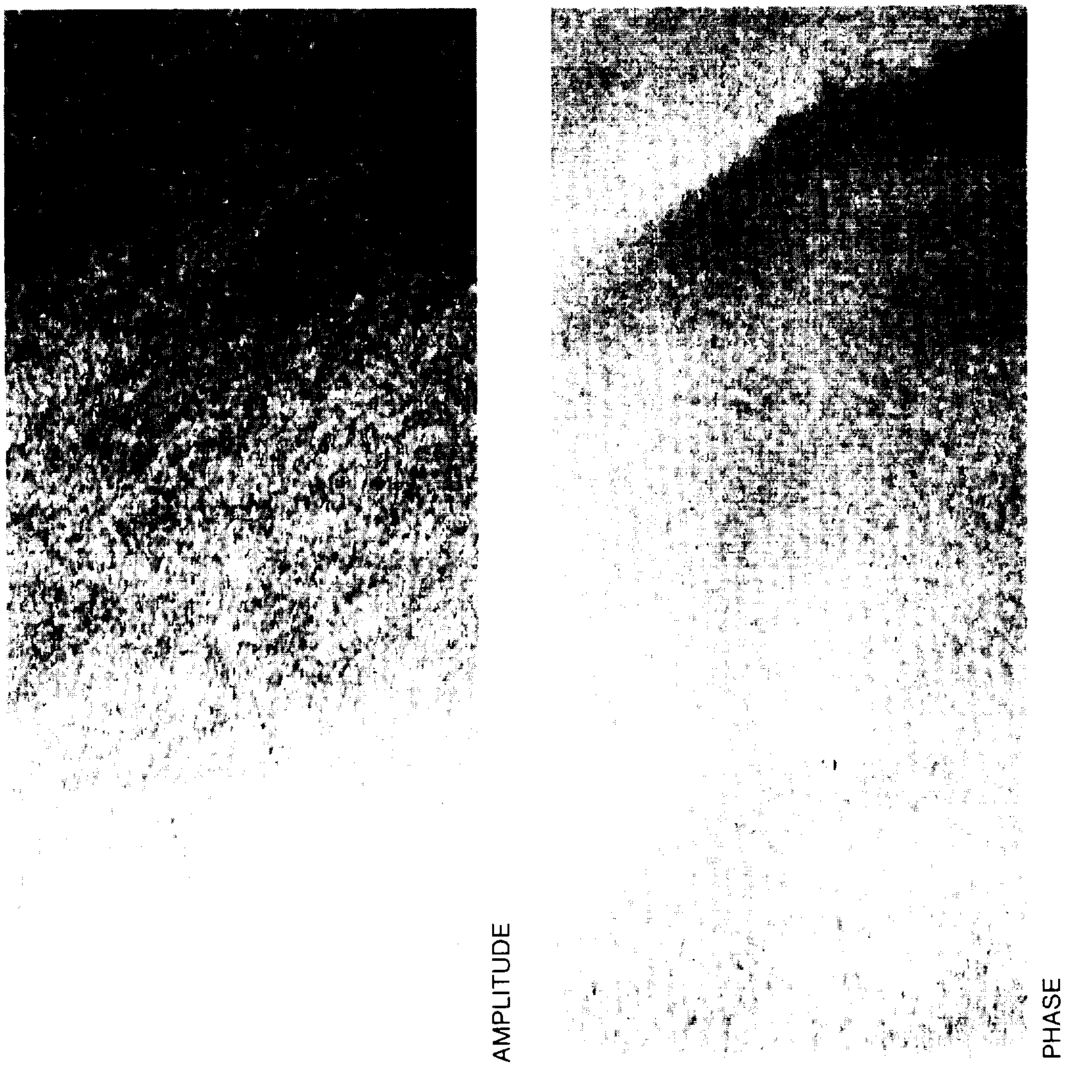

Figure 1: The INSAR amplitude (left) and phase (right) images for run G-Stream NI 120-1 taken July 20, 1990 are displayed. The area of each image is approximately 5 km in azimuth and 10 km in range. See text for additional discussion.

3. GROUND TRUTH INFORMATION AND MODELING

Ground truth information is available in the form of buoy measurements of the wave spectrum and direction. Two buoys were deployed both before and after the INSAR image of Figure 1 was taken. We have Fourier analyzed the phase image to determine the spectrum of the wave-like structures seen throughout the image. The frequency and direction are directly compared to the buoy data. The Henlopen's wake also may aid in our interpretation of surface features. Thus the available ground truth in conjunction with the INSAR image provides useful constraints for modeling Gulf Stream boundary features.

We are currently modeling both INSAR and SAR radar return from ocean surfaces. This is an ongoing project and results will be reported at a future date.

4. CONCLUSIONS

Our initial investigation has yielded several interesting characteristics of INSAR imagery: The wave spectrum is clearly seen in the phase image but not in the amplitude. The boundary of the Gulf Stream is a strong linear feature — barely resolved in the amplitude image — which dominates the phase image. Similarly, the Henlopen's wake is easily seen in the phase image. Of course, the ship is clearly resolved in both the amplitude and phase images.

ACKNOWLEDGEMENTS

We thank J. S. Lee and D. Schuler from NRL for many helpful insights and informative discussions. We also thank S. Madsen from JPL for performing the initial image processing.

REFERENCES

Carande, R. E., R. M. Goldstein, Y. Lou, T. Miller and K. Wheeler, 1991, "Dual-frequency Along-track Interferometry: A Status Report," *Proceedings of the Third Airborne Synthetic Aperture Radar Workshop,* JPL Publication 91-30, Jet Propulsion Laboratory, Pasadena, California, pp. 109–116.

Carande, R. E., 1992, "Dual Baseline and Frequency Along-track Interferometry," *Proceedings of IGARSS '92,* pp. 1585–1588.

Goldstein, R. M. and H. A. Zebker, 1987, "Interferometric Radar Measurements of Ocean Surface Currents," *Nature,* **328,** pp. 707–709.

Goldstein, R. M., T. P. Barnett and H. A. Zebker, 1989, "Remote Sensing of Ocean Currents," *Science,* **246,** pp. 1282-1285.

Kobrick, M., 1990, "AIRSAR Data Digest Summer 1990," *JPL D-8123* (internal document), Jet Propulsion Laboratory, Pasadena, CA.

Milman, A. S., A. O. Scheffler and J. B. Bennett, 1990, *J. Geophys. Res.,* **98,** pp. 911–925.

Thompson, D. R. and J. R. Jensen, 1993, "Synthetic Aperture Radar Interferometry Applied to Ship-generated Internal Waves in the 1989 Loch Linnhe Experiment," *J. Geophys. Res.,* **98,** pp. 10259–10269.

Valenzuela, G. R., R. P. Mied, A. R. Ochadlick, M. Kobrick, P. M. Smith, F. Askari, R. J. Lai, D. Sheres, J. M. Morrison and R. C. Beal, 1991, "The July 1990 Gulf Stream Experiment," *Proceedings of IGARSS '91,* pp. 119–122.

Zebker, H. A. and R. M. Goldstein, 1986, "Topographic Mapping from Interferometric Synthetic Aperture Radar Observations," *J. Geophys. Res.,* **91,** pp. 4993–4999.

MAC-91: POLARIMETRIC SAR RESULTS ON MONTESPERTOLI SITE

N95-23940

S. Baronti (*), S . Luciani (**), S. Moretti (***),
S. Paloscia (*), G. Schiavon (**) and S. Sigismondi (***)

(*) Istituto di Ricerca sulle Onde Elettromagnetiche - CNR
Via Panciatichi 64, 50127 Firenze (I)
(**) Dipartimento di Ingegneria Elettronica, Università Tor Vergata
Via della Ricerca Scientifica, 00133 Roma (I)
(***) Dipartimento di Scienze della Terra, Università di Firenze
Via La Pira 4, 50121 Firenze (I)

1. INTRODUCTION

The polarimetric Synthetic Aperture Radar (SAR) is a powerful sensor for high resolution ocean and land mapping and particularly for monitoring hydrological parameters in large watersheds. There is currently much research in progress to assess the SAR operational capability as well as to estimate the accuracy achievable in the measurements of geophysical parameters with the presently available airborne and spaceborne sensors. An important goal of this research is to improve our understanding of the basic mechanisms that control the interaction of electromagnetic waves with soil and vegetation. This can be done both by developing electromagnetic models and by analyzing statistical relations between backscattering and ground truth data. A systematic investigation, which aims at a better understanding of the information obtainable from the multi-frequency polarimetric SAR to be used in agro-hydrology, is in progress by our groups within the framework of SIR-C/X-SAR Project and has achieved a most significant milestone with the NASA/JPL Aircraft Campaign named MAC-91. Indeed this experiment allowed us to collect a large and meaningful data set including multi-temporal multi-frequency polarimetric SAR measurements and ground truth.
This paper presents some significant results obtained over an agricultural flat area within the Montespertoli site, where intensive ground measurements were carried out. The results are critically discussed with special regard to the information associated with polarimetric data.

2. EXPERIMENT DESCRIPTION

During the Multisensor Airborne Campaign (MAC-91), the site of Montespertoli (Italy) was imaged on three different dates (22 June, 29 June and 14 July) by the airborne JPL polarimetric SAR (AIRSAR) operating at P-, L- and C- band (Canuti et al., 1992). Three passes were performed during each flight data, in order to cover the most significant sub-areas with different incidence angles θ between 20° and 50°. Nominal pixel sizes obtained on the 16 looks images were 6.6 m in range and 12 m in azimuth. The test site covers the basins of two small rivers and contains a relatively large flat area, along the border of the Pesa river, which includes agricultural fields of various crops (i.e. alfalfa, colza, corn, sorghum, sunflower, wheat) bare soils, olive-yard, vineyards and a few small forests. The area was equipped with two trihedral corner reflectors of 180 cm and one of 240 cm, supplied by the JPL, and deployed along the Pesa river. In addition, a few "extended homogeneous targets", namely three plots of bare soil with different surface roughness, one field of alfalfa and one of sunflower, had been specifically prepared, in the same sub area, to act as "distributed" calibrators. The ground data, which were collected on selected fields at the same time as the remote sensing measurements, regarded all the significant vegetation and soil parameters, such as leaf area index (LAI), plant water content (PWC), dimensions of leaves and stalks, soil moisture content and roughness. During the experiment the average gravimetric soil moisture of the first 5 cm layer changed from about 15-20 % (on

June 22) to about 10% (on July 14). At the same time the leaf area index (m^2/m^2) of sorghum and corn increased from ~ 0.5 to ~ 3.5, that of sunflower from ~ 0.5 to ~ 3.5. Alfalfa leaf area index ranged from ~ 0 to ~ 4. Wheat and colza were in the ripening stage and therefore their LAI was almost 0; some of these fields were harvested at the time of the last flight.

3. DATA ANALYSIS

Calibrated (amplitude and phase) polarimetric data, collected over the agricultural area on alfalfa, corn, colza, sunflower, sorghum, bare soil, olives, vineyard and on a few forested areas, at incidence angles of 35° and 50°, have been analyzed.

Background - Scattering sources may be grouped in broad categories, each associated to typical scattering behaviors, as shown in recent works (e.g. Ulaby et al. 1990, Van Zyl 1989). In particular: a) Soil response is a surface scattering effect. This effect is important for bare soils and, in general, at low frequencies, where many agricultural crops are rather transparent. σ°_{RL} is appreciably higher than σ°_{RR} and σ°_{HV} is low. At lower frequencies (P and L band) $\sigma^\circ_{VV} > \sigma^\circ_{HH}$, as predicted by the Small Perturbation surface scattering model (Ulaby et al. 1982), while at higher frequencies (C band) $\sigma^\circ_{VV} \approx \sigma^\circ_{HH}$. b) Vertical structures, like forest trunks and crop stalks, produce double-bounce scattering. In general, this mechanism is important at P band for forests and at L band for some agricultural crops like corn and sunflower. σ°_{HV} is low, as in the soil scattering case, but, differently from the soil, σ°_{HH} is generally higher than σ°_{VV} and the large difference between σ°_{RL} and σ°_{RR} disappears. c) Ensembles of inclined cylindrical structures, like forest branches and crop stems, produce volume scattering with an appreciable presence of multiple scattering. The differences $\sigma^\circ_{HH} - \sigma^\circ_{HV}$ and $\sigma^\circ_{VV} - \sigma^\circ_{HV}$ are much lower than those for soil and vertical structures. In circular polarization, $\sigma^\circ_{RL} \approx \sigma^\circ_{RR}$. d) Ensembles of inclined planar structures, like leaves, also produce volume scattering; however, an appreciable amount of single "facet" scattering is present. $\sigma^\circ_{HH} - \sigma^\circ_{HV}$ and $\sigma^\circ_{VV} - \sigma^\circ_{HV}$ differences are relatively low, similarly to the cylinder case, but at circular polarization, the "facet" effect generates appreciable positive $\sigma^\circ_{RL} - \sigma^\circ_{RR}$ differences. The scatterer dimensions have important effects too. Let branches and stems be represented as ensembles of cylinders with the length proportional to the radius. For a canopy of equal cylinders, the backscatter coefficient changes with the cylinder length (expressed in wavelengths) and shows a maximum (Karam et al. 1992). It follows that, for each band, there is a range of cylinder dimensions generating a dominant contribution to the backscatter. For leaves, which can be described as discs, scattering is dependent on thickness and moisture content (Ferrazzoli et al. 1993).

4. SURFACE TYPE DISCRIMINATION

Some significant backscattering features of agricultural surfaces can be inferred from Fig. 1 which represents the cross-polarized backscattering coefficient (σ°_{HV}) of well developed (Plant Water Content - PWC > 1 Kg/m^2) crops measured at L-band and $\theta = 35°$, as a function of the corresponding σ°_{HV} at C-band. At L-band there is a continuous increase of backscatter as the dimensions of scattering elements increase from the 'small leaf' crops such as alfalfa (A) and sorghum (S) to the bigger olive-yards (O) and forest trees (T), passing through 'broad leaf' crops such as sunflower (F) and colza (R). At C-band, bare soil can be discriminated from crops among which colza, which has a well ramified structure, has the highest backscattering value.The relatively strong capability of C-band backscattering to discriminate agricultural surfaces is improved if circular polarization data are used as well (Baronti et al. 1993). Indeed, bare soils and plants characterized by relatively large leaves, like sunflower, corn, sorghum, show a "facet" scattering with $\sigma^\circ_{RL} > \sigma^\circ_{RR}$. while, in the other fields, $\sigma^\circ_{RL} \approx \sigma^\circ_{RR}$. However colza crops show rather high backscatter at both RR and RL polarizations, due to their scattering elements (stems, pods) which are numerous and relatively large, while the elements of wheat and alfalfa crops produce lower backscattering. It must be noted that, unlike L-band, discrimination is feasible also in the case of moderate growth. Figure 2 shows $\sigma°_{HV}$ versus $\sigma°_{HH}$ measured at P-band and $\theta = 35°$. According to the previous considerations the scattering in HV pol. is mainly due to inclined and relatively large cylindrical elements, like branches of forest, oliveyard and vineyard, while the agricultural vegetation is rather transparent. Three classes of $\sigma°_{HV}$ values may be identified corresponding to: forests (T), olive-yard and vine-yard (O and V) and agricultural fields (A). Accordingly P-band backscattering, which is dominated by the tree branches and the soil trunk interaction, appears rather effective in discriminating broad classes of surfaces (forest, olive-yard, vine-yard, agricultural fields) but their utility in discriminating the various agricultural crops is poor. At L-band, where scattering is mainly due to stems and large leaves, the SAR data appear more suitable for separating the 'broad leaf' crops (corn and colza) from other crops; this discrimination is improved using C-band data which are particularly sensitive to small stems and leaves (Coppo et al. 1989). Note that a discrimination between alfalfa and wheat fields does not appear feasible at C-band; however, recent works indicate that it becomes possible by means of both active and passive remote sensing systems if higher frequencies (X- and K- bands) are used (Ferrazzoli et al. 1992).

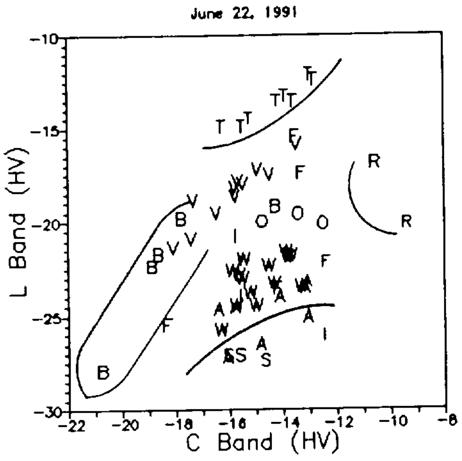

Figure 1 - Backscattering Coefficient ($\sigma°$) at L-band vs.$\sigma°$ at C-band (HV pol. θ=35°) Labels: B=bare soil, T=forest, V=vine-yard, O=olive-yard, W=wheat, A= alfalfa, S=sorghum, F=sunflower, R=colza, I=uncropped

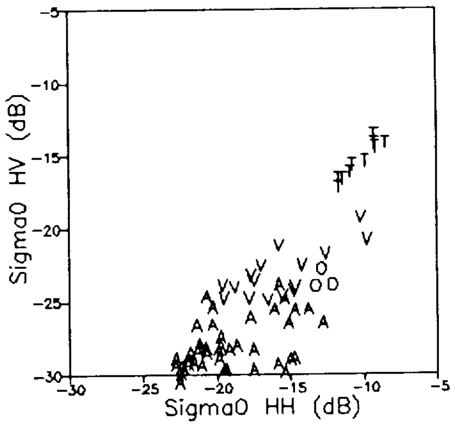

Figure 2 - $\sigma°_{HV}$ vs. $\sigma°_{HH}$ at P-band, θ=35°

SENSITIVITY TO SOIL MOISTURE AND VEGETATION BIOMASS

Soil Moisture - The measurement of soil moisture (SMC) with radar has been the subject of much research over the past years. However, a reliable extraction of such information from SAR data is still questionable in that the signal is strongly influenced by surface roughness and vegetation cover. In our case data collected at L and C-band show very little correlation with SMC even at $\theta = 35°$. A slightly better result has been obtained at P-band where the $\sigma°_{HH}$ has shown a sensitivity to SMC equal to 1.0 dB/% SMC and a correlation coefficient equal to 0.7.

Herbaceous crops - In this experiment the agricultural vegetation was rather transparent at P-band while, at C-band, it generated considerable scattering effects even in the case of moderate growth. Indeed, the highest correlations with plant growth have been noted at L-band. On the other hand $\sigma°_{HV}$, which is low for bare soils and is mainly associated to the presence of inclined stems and large leaves, is a relatively good growth indicator. Figure 3 shows L-band σ°_{HV} as a function of the Plant Water Content (PWC, kg/m^2). Samples of sorghum (S), corn (C), sunflower (F) and bare soil have been included. Very rough (ploughed) bare soils are labeled 'PB', while moderately rough (tilled or rolled) bare soils are labeled 'TB'. The correlation is generally good; the lowest σ°_{HV} values are associated with moderately rough bare soils and with sorghum fields at a very early stage of growth, while the highest values are associated with well developed sunflower crops.Ploughed bare soils show relatively high values,indicating that the roughness plays a role similar to that of vegetation growth. The dynamic range is notable, in the order of 10 dB. The plant growth may be also related to $\sigma^\circ_{HH} - \sigma^\circ_{VV}$ at L-band. In fact, for bare soils, $\sigma^\circ_{HH} < \sigma^\circ_{VV}$ while, for developed crops, the soil plant double bounce scattering, which may be rather important at L-band, produces a positive $\sigma^\circ_{HH} - \sigma^\circ_{VV}$ difference.

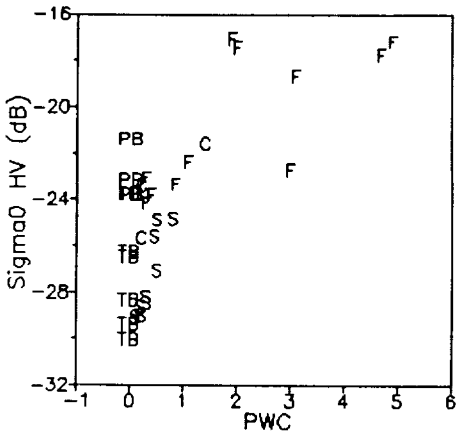

Figure 3- σ°_{HV} vs. PWC (Kg/m^2) at L-band, θ=50°

CONCLUSIONS

Polarimetric SAR measurements carried out over forests, oliveyards, vineyards and agricultural fields indicate that P-band data are effective in discriminating among broad surface categories, L-band data allow identification of well developed sunflower, corn and colza crops, and C-band data discriminate among different kinds of herbaceous crops even in the case of moderate growth. A fairly good sensitivity of σ°_{HV} and $\sigma^\circ_{HH} - \sigma^\circ_{VV}$ to the Plant Water Content of some agricultural species is observed at L-band.

ACKNOWLEDGMENT

This work was partially supported by the Italian Space Agency

REFERENCES

Baronti, S. F. Del Frate, P. Ferrazzoli and S. Paloscia, "Interpretation of Polarimetric MAC-91 data over Montespertoli Agricultural area," Proc of the 25th Intern. Symposium, Remote Sensing and Global Change, Graz (Austria), 1993.

Canuti, P., G. D'Auria, P. Pampaloni, and D. Solimini "MAC-91 on Montespertoli: an experiment for agro-hydrology", Proc. of the IGARSS Symposium, Houston, Texas, 1992, 1744-1746.

Coppo, P., P.Ferrazzoli, G.Luzi, P.Pampaloni, G.Schiavon, D.Solimini 1989, "Microwave remote sensing of land surfaces with airborne active and passive sensors," Proc. of the IGARSS Symp., Vancouver (Canada), 1989, 806-809.

Ferrazzoli, P.,D. Solimini, G. Luzi, and S. Paloscia, "Model analysis of backscatter and emission from vegetated terrains," J. of Electromagnetic Waves and Applications, vol. 5, 175-193, 1991

Ferrazzoli, P., L. Guerriero, S. Paloscia, and P. Pampaloni, "Modeling X and Ka band emission from leafy vegetation," Proc. of the URSI Microwave Signature Conf., Igls-Innsbruk, 1992, 2B14-2B17.

Karam, M.A., A.K. Fung, R.H. Lang, and N.S. Chauhan, "A microwave scattering model for layered vegetation," IEEE Trans. Geosci. Remote Sensing, vol. GE-30, 767-784, 1992.

Ulaby, F.T., R.K Moore, and A.K. Fung, Microwave Remote Sensing: Active and Passive. Vol.II - Surface Scattering and Emission Theory, Addison-Wesley, Reading, Massachusetts, 1982.

Ulaby, F.T., and C. Elachi, editors, Radar polarimetry for geoscience applications, Norwood, MA: Artech House, 1990

Van Zyl, J.J., "Unsupervised classification of scattering behavior using radar polarimetry data", IEEE Transactions on Geoscience and Remote Sensing , vol. GE-27, pp. 36-45. 1989.

N95- 23941

AIRSAR VIEWS OF AEOLIAN TERRAIN

Dan G. Blumberg and Ronald Greeley
Department of Geology
Arizona State University
Tempe Az. 85287-1404

1. OVERVIEW

Remote sensing observations of terrestrial dune morphologies provide information on sand transport, climate, and soil processes associated with aeolian processes. In this study AIRSAR images of the Stovepipe Wells Dune Field, California, were examined to assess the degree to which dune types can be determined from radar images and the factors leading to the formation of four different dune types in one locality. The images were acquired during the Geologic Remote Sensing Field Experiment (GRSFE; Evans et al., in press) and later. These images provide a unique opportunity to enhance the knowledge of how radar images allow discrimination of dune forms.

2. RADAR DATA

Radar images were obtained in September 1989 and May 1992 by the Jet Propulsion Laboratory synthetic aperture radar - AIRSAR. The images have a resolution of ~12 m per pixel and are acquired in C-band ($\lambda = 5.6$ cm), L-band ($\lambda = 24$ cm), and P-band ($\lambda = 67$ cm). All images were calibrated using POLCAL (van Zyl et al., 1992). Although the entire Stokes matrix is saved for the images and any polarization can be extracted, only the co- and cross-polarized data were extracted (HH; VV; HV-VH). Figure 1 (See Slide 12) shows an image of the total power return at Stovepipe Wells for C, L, and P-band in HH polarization.

The illumination was from the west and the flight direction from north to south. The look angle was 45°.

3. OBSERVATIONS

The Stovepipe Wells Dune field covers an area of ~100 km^2 in northern Death Valley, California (117°06 W 36° 39 N). Four dune types, each characteristic of a different wind regime, occur at Stovepipe Wells: reverse dunes, star dunes, transverse, and linear dunes. In addition to dunes, C-band images reveal a mantle of sand around the dune field. Field observations show that local saline crusts in the sand mantle cause microscale roughness variations that give a mottled radar backscatter cross section that is prominent in C-band but less pronounced in P and L-bands.

3.1 Reverse dunes

The reverse dunes are low (typically < 5 m high), formed by temporal reversals of the wind direction through the valley (N - S). The reverse dunes are observed in the radar images as dark and bright linear features on the northeast part of the field. The dunes appear as dark narrow streaks aligned east-west with bright interdune regions. The low reverse dunes are not seen in P-band, but are visible in C-band. They are best observed in the H-H images, and not seen in the cross-polarized image.

3.2 Star dunes

The star dunes have a maximum height of 40 m above the surrounding surface and are formed by polymodal winds transporting sand to the center of the dune field. Star dunes have at least three flanks which create a trihedral corner reflector effect in radar images. The result is an extremely bright speckle from the interdune zone facing the antenna. These dunes are easily recognized in AIRSAR images of Stovepipe Wells because of the quasi-speckular return from the corner between the dune flanks. The quasi-speckular signature is visible in all wavelengths.

3.3 Transverse Dunes

Transverse dunes are found in the northern part of the dune field. These are formed by unimodal winds blowing from the north. The winds from the south (that are partly responsible for the reverse dunes) are blocked by a mountain and by the large star dunes. The transverse dunes appear in the radar images as alternating bright and dark stripes. These dunes exhibit bright lee slopes and dark narrow stoss slopes. Transverse dunes are visible in all wavelengths but are not seen in the cross-polarized data.

3.4 Linear dunes

In the west part of the dune field there is a set of linear dunes which are formed by bi-directional winds coming from the northeast and southeast. Blom and Elachi (1981) state that the interdune spacing needs to be at least 3 to 4 picture elements wide to be able to detect linear dunes. The interdunal spacing of these dunes is greater than 4 pixels. In the 1992 image these dunes appear as narrow reflective streaks. Because the linear dunes are in the very near range, their form is more difficult to resolve in this image than other dune types.

3.5 Vegetated dunes

Very sparse vegetation exists at the Stovepipe Wells Dune Field. The vegetation is primarily in clusters over the sand mantle and in an area where the dune forms change from reverse to star dunes. While vegetation can be seen in all images it is most pronounced in the cross-polarized images. Comparison of the vegetation in the radar images to aerial photographs from 1948 do not show any spatial change in the vegetation pattern.

4. Conclusion

The Stovepipe Wells Dune Field provides a unique opportunity to observe several dune forms in one scene. These forms include reverse dunes, star dunes, transverse, and linear dunes. A sand mantle surrounds the dune field and can also be observed in the radar image. Dune types were discriminated best in co-polarized channels.

Three major wind directions are responsible for the various dune forms. Wind from the north and south are responsible for the reverse dunes, winds from north the for the transverse dunes, and the north - south and westerly winds form the star dunes. The winds also reflect the topographic configuration of this part of the valley.

Vegetation over the dunes was most pronounced in the cross-polarized images. Lancaster et al. (1992) finds that cross-polarized images are most useful in differentiating active from inactive dunes. This is because the vegetation backscatter signature is present over inactive dunes.

Future studies should include multiple look and incidence angles to determine if the dune forms can still be seen at other angles.

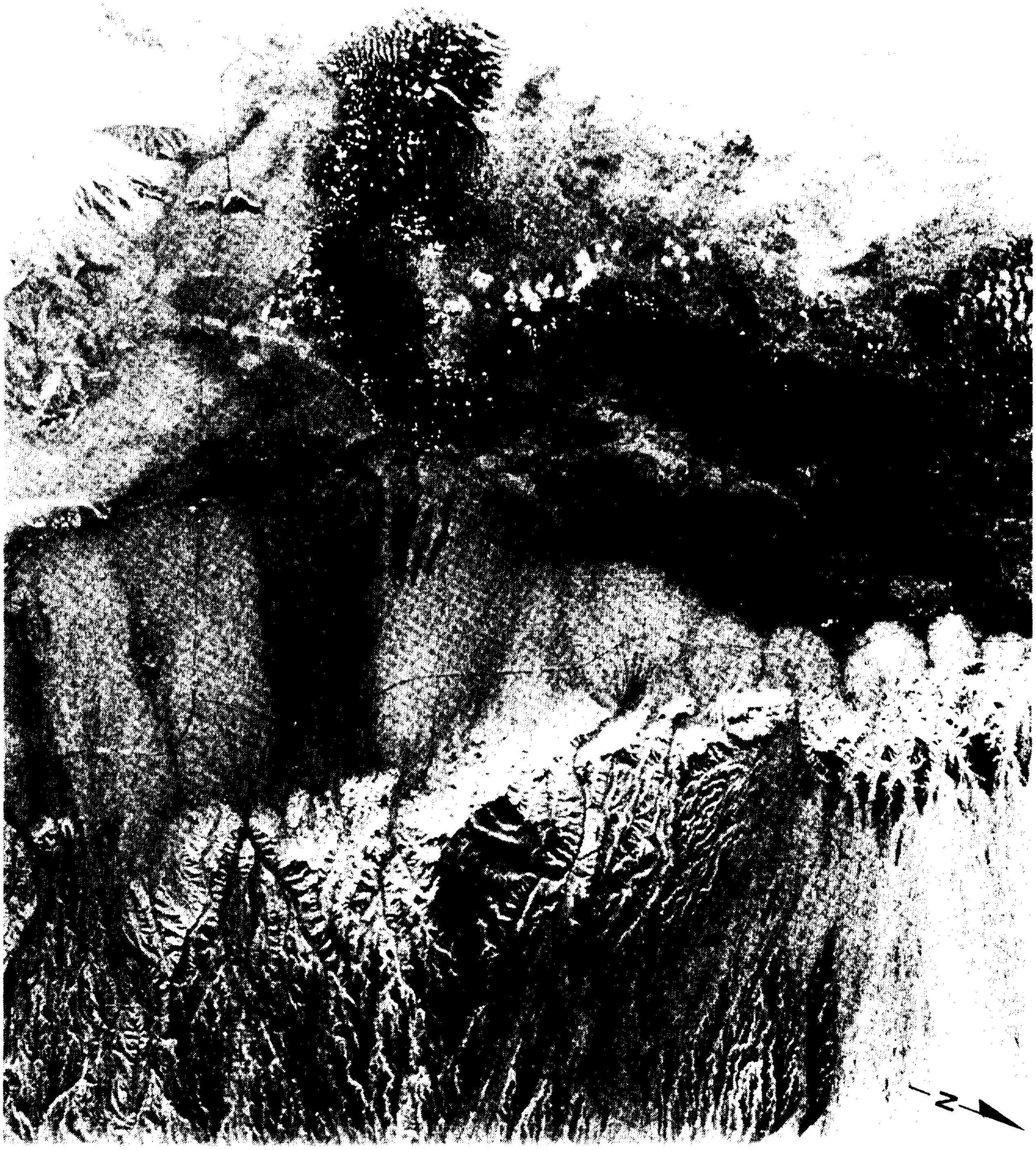

Figure 1. AIRSAR image of Stovepipe Wells Dune Field, Death Valley, California. The image shows total power for C, L, and P-bands

References cited:

Blom R. and C. Elachi, 1987, "Spaceborne and Airborne Imaging Radar Observations of Sand Dunes", *J. Geophys. Res.*, 86 (B4), 3061-3073.

Evans D.L., T.G. Farr, M. Vogt, C. Bruegge, J. Conel, R.E. Arvidson, S. Petroy, J.J. Plaut, M. Dale-Bannister, E. Guiness, R. Greeley, N. Lancaster, L. Gaddis, J. Garvin, D. Deering, J. R. Irons, F. Kruse, D. J. Harding, submitted, "The Geologic Remote Sensing Field Experiment", *IEEE Transaction of Geoscience and Remote Sensing*.

Lancaster N., L. Gaddis, and R. Greeley, 1992, "New Airborne Imaging Radar Observations of Sand Dunes: Kelso Dunes", California, *Remote Sens. Environ.*, 39, pp. 233-238.

van Zyl J.J., C.F. Burnette, H.A. Zebker, A. Freeman, J. Holt, 1992, *Polcal Users Manual*, JPL D-7715 version. 4.0., pp. 48.

N95- 23942

GLACIOLOGICAL STUDIES IN THE CENTRAL ANDES USING AIRSAR/TOPSAR

Richard R. Forster, Andrew G. Klein, Troy A. Blodgett
and Bryan L. Isacks
Cornell University
Department of Geological Sciences
Snee Hall
Ithaca, New York 14853-1504

1. INTRODUCTION

The interaction of climate and topography in mountainous regions is dramatically expressed in the spatial distribution of glaciers and snowcover. Monitoring existing alpine glaciers and snow extent provides insight into the present mountain climate system and how it is changing, while mapping the positions of former glaciers as recorded in landforms such as cirques and moraines provide a record of the large past climate change associated with the last glacial maximum. The Andes are an ideal mountain range in which to study the response of snow and ice to past and present climate change. Their expansive latitudinal extent offers the opportunity to study glaciers in diverse climatic settings from the tropical glaciers of Peru and Bolivia to the ice caps and tide-water glaciers of sub-polar Patagonia.

SAR has advantages over traditional passive remote sensing instruments for monitoring present snow and ice and differentiating moraine relative ages. The cloud penetrating ability of SAR is indispensable for perennially cloud covered mountains. Snow and ice facies can be distinguished from SAR's response to surface roughness, liquid water content and grain size distribution. The combination of SAR with a coregestered high-resolution DEM (TOPSAR) provides a promising tool for measuring glacier change in three dimensions, thus allowing ice volume change to be measured directly. The change in moraine surface roughness over time enables SAR to differentiate older from younger moraines.

Polarimetric SAR data have been used to distinguish snow and ice facies (Shi et al., 1991) and relatively date moraines (Forster et al., 1992). However, both algorithms are still experimental and require ground truth verification. We plan to extend the SAR classification of snow and ice facies and moraine age beyond the ground truth sites to throughout the Cordillera Real to provide a regional view of past and present snow and ice. The high resolution DEM will enhance the SAR moraine dating technique by discriminating relative ages based on moraine slope degradation (Bursik, 1991).

2. 1993 FIELD CAMPAIGN

The 1993 South American AIRSAR campaign acquired data at four sites in the Peruvian and Bolivian Andes. TOPSAR data was acquired at all sites. Three of the four sites, the Quelccaya Ice Cap, the Cordillera Blanca, both in Peru, and the Cordillera Real, Bolivia were targeted for their numerous modern glaciers and Pleistocene glacial landforms. The fourth, Potosi, Bolivia was chosen for its well preserved multiple moraines and alluvial outwash plains. The Cordillera Real was chosen as the ground truth site because of the easy access to its glaciers.

Ground truth data were acquired on two glaciers in the Cordillera Real during the AIRSAR flight. The two glaciers reside on adjacent mountains of the Cordillera north-east of La Paz. We recorded the following data from the Chacaltaya glacier: surface roughness profiles, snow depth transacts, and snow pit profiles of density, temperature,grain size distribution, and wetness. Measurements were taken on two days previous to the flight, the day of the flight and the day after the flight. Metrological data were recorded on the flight day and the following day. French collaborators from ORSTOM took a set of similar measurements on their research glacier, the Zongo glacier, during the AIRSAR flight. Four corner reflectors (manufactured in Bolivia) were deployed and their positions determined with GPS on and around the Chacaltaya glacier for co-regestation. The entire Cordillera was imaged with six swaths, five parallel to the mountain range and one oblique, optimizing the viewing geometry of the two neighboring ground truth glaciers.

During the two weeks after the SAR flight we collected samples from original surfaces of moraine boulders at several locations in the Cordillera Real and at the Potosi site for ^{36}Cl cosmogenic ray dating. This will provide numerical dates for the SAR derived moraine chronology.

3. ANTICIPATED RESULTS

The measured surface roughness and dielectric properties (snow wetness, grain size distribution and density) of the snow and ice will be used to interpret the polarization signatures obtained from different snow facies present on the glaciers. We will also map the snow facies boundaries on the test glaciers and extrapolate these results to glaciers throughout the Cordillera. We anticipate this research will provide the ground work for establishing a three dimensional base line for future monitoring of annual snowline and glacier positions over a regional setting. This DEM will be used for comparison with our present digitized topography and SPOT derived DEMs. The high resolution DEM derived from TOPSAR combined with a regional moraine chronology will allow detailed glacier reconstruction and ice volume calculations for known times during the Pleistocene. The AIRSAR coverage of the Cordillera Real will overlap with a SIR-C/X-SAR site providing an instrument and temporal comparison. Data from the Patagonian SIR-C/X-SAR supersite along with a similar ground campaign will allow a direct comparison of polarimetric SAR response to high elevation tropical glaciers and mid-latitude low elevation glaciers.

4. REFERENCES

Bursik, M., 1991, Relative dating of moraines based on landform degradation, Lee Vining Canyon, California. *Quaternary Research*, 35, pp. 451-455.

Forster, R. R., Fox, A. N., Isacks, B. I., 1992, Preliminary results of polarization signatures for glacial moraines in the Mono Basin, Eastern Sierra Nevada, *Summaries of The Third Annual JPL Airborne Geosciences Workshop*, JPL Publication 92-14 vol. 3, pp. 40-42.

Shi, J., Dozier, J., Rott, H., Davis, R. E., 1991, Snow and glacier mapping in alpine regions with polarimetric SAR. *Proceedings IGARSS' 91*, IV, pp.2311-3214.

N95- 23943

ESTIMATION OF BIOPHYSICAL PROPERTIES OF UPLAND SITKA SPRUCE (*PICEA SITCHENSIS*) PLANTATIONS.

Robert M. Green

Department of Geography, University College of Swansea,
Singleton Park, Swansea, SA2 8PP, U.K.

1. INTRODUCTION.

It is widely accepted that estimates of forest above-ground biomass are required as inputs to forest ecosystem models (Kasischke and Christensen, 1990), and that SAR data have the potential to provide such information (e.g. Kasischke *et al.*, 1991; LeToan *et al.*, 1992). This study describes relationships between polarimetric radar backscatter and key biophysical properties of a coniferous plantation in upland central Wales, U.K. Over the test site topography was relatively complex and was expected to influence the amount of radar backscatter.

2. TEST SITE AND DATA

As part of the NASA MAC Europe (Curran and Plummer, 1992) the JPL AIRSAR was flown over the Tywi forest, in central Wales, U.K. This is an area of coniferous forest plantations, consisting of Sitka spruce (*Picea sitchensis*), Lodgepole pine (*Pinus contorta var. latofoliar*) and Japanese larch (*Larix kaempfei*), surrounding the Llyn Brianne reservoir. It is an upland region characterized by variable topography of up to 500m above mean sea level with some valley slopes of 45° or more. For this study only areas of Sitka spruce were analyzed since this was the dominant species with the widest range of planting dates on a variety of slope/aspect orientations relative to the SAR. All the species are densely stocked with planting spacing typically 2 metres. The ground data comprised results of an intensive field survey for a limited number of stands; and for a much larger area, the planting date of forest compartments was known from stocking maps.

The AIRSAR images consisted of a slant range pixel resolution of 3.4m and incidence angle ranged from approximately 20° near-range to between 55° and 60° far-range. The Stokes matrix data were analyzed using POLTOOL, a polarimetric SAR data processing package. P-band data were subject to interference at all polarization combinations and were consequently not used in the analysis. This is a disappointing situation since some authors have found P-band data to be most sensitive to forest biomass (e.g. LeToan *et al.*, 1992).

2. BACKSCATTER RELATED TO STEM BIOMASS ESTIMATES

Estimates of key biophysical parameters were derived for forest stands within the Cefn Fannog plantation managed by the U.K. Forestry Commission. Data available from the Forestry Commission included surveys performed in 0.01ha plots at regular intervals in the area. From standard forestry mensuration data the average basal area, stem volume and stem biomass for each stand were derived. The average intensity of backscatter (amplitude) for a group of pixels corresponding to a forest stand was extracted from the AIRSAR imagery, synthesized into HH, HV and VV polarizations using POLTOOL.

16

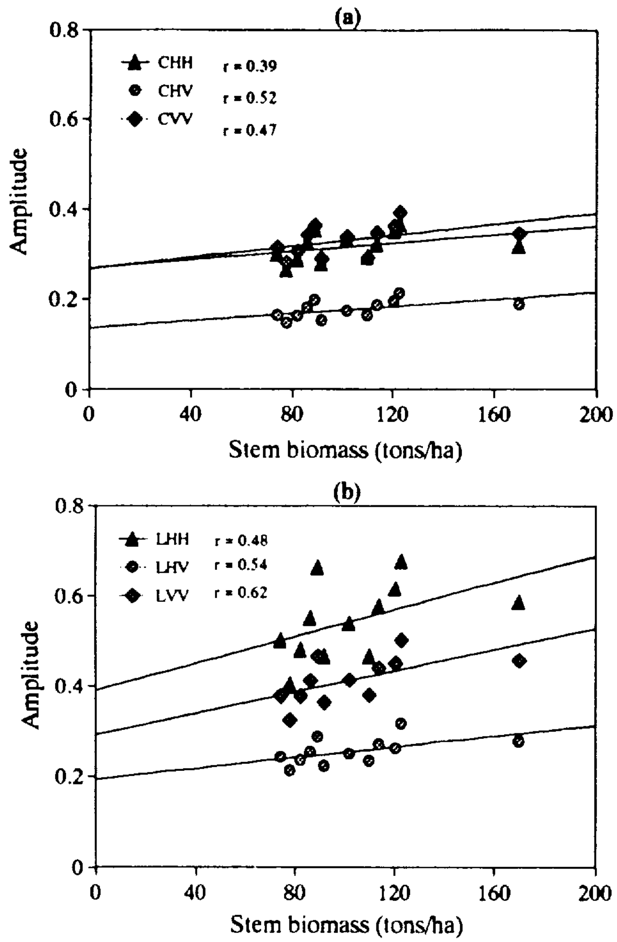

Figure 1. Plots of amplitude versus average stand biomass using data synthesized into HH, HV, and VV polarizations in (a) C-band, and (b) L-band.

Figure 1 shows plots of C-, and L-band backscatter versus stem biomass. The amount of C-band backscatter was lower than L-band. Luckmann and Baker (1993), using the same data set, attribute this to a lack of scatterers at the same size as C-band wavelengths. In Figure 1a the best-fit lines do not show any significant increasing relationships in any of the polarization combinations. This is to be expected if it is assumed that C-band scattering takes place in the upper levels of the canopy, since all the stands which were sampled had uniform canopy characteristics. The L-band plots (Figure 1b) show positive relationships. The highest correlation coefficient was derived for the VV polarization data (r=0.62, significant at the 95% level of confidence). Stronger relationships may have been obtained with the longer wavelength P-band data.

3. BACKSCATTER RELATED TO STAND AGE.

Over large areas it is logistically impossible to carry out intensive field surveys in order to derive biomass estimates. However, accurate Forestry Commission stock maps exist for the whole of the Tywi forest containing information regarding the planting dates of forest stands. Stand age was used as a surrogate for biomass and only unthinned stands

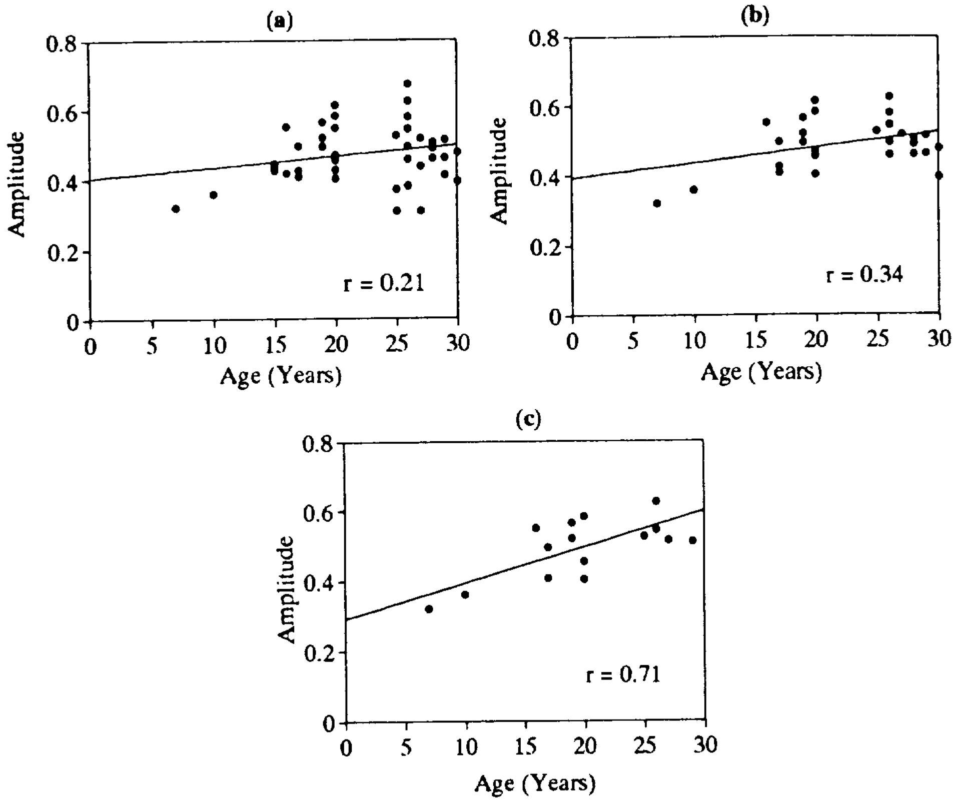

Figure 2. Plots of L-band HH amplitude versus stand age for (a) all stands; (b) stands on steep slopes facing away from the SAR removed; (c) stands on level ground removed.

were considered in the analysis ensuring, as far as possible, uniform canopy structure and density of boles.

Figure 2a shows a plot of L-band HH polarization backscatter versus stand age. There was a general increase in backscatter until the age of 25 years. There was then significant variability in backscatter illustrated by a weak negative relationship. However, it was to be expected that as trees reach maturity that the amount of backscatter will increase at a slower rate until a saturation point is reached (Groom *et al.*, 1992). It was expected that topographic variations will influence the amount of backscatter . In order to reduce the effect of abnormally low backscatter, all stands at an aspect of between 90° and 180° relative to the SAR look direction and with slope angles greater than 5° were eliminated (Figure 2b), i.e. stands on steep slopes facing away from the sensor were excluded from the analysis. Some of the variability disappeared and the correlation rose to r=0.34.

Much of the variability that still existed was found to be the backscatter from those stands that were situated on flat ground (slope angles typically less than 1°). These stands were located in a basin surrounding a natural lake. Productivity of Sitka spruce stands is related to soil water content, which varies as a function of slope angle (Coutts and Philipson, 1978). Stands situated on well drained slopes tend to have higher growth rates and hence more biomass compared to stands of a similar age in areas of poorly drained soils. Therefore topography indirectly determined the amount of biomass production. When stands situated on slope angles of less than 1° were eliminated from the data set the resulting relationship (Figure 2c) resembled those derived by previous authors from forests in different environments, and the r-value again increased (r=0.71). Therefore in this instance, age is not a good surrogate for biomass unless other environmental information is taken into account.

4. CONCLUSION.

This study has shown preliminary results of analysis of radar backscatter in a dense spruce forest plantation in an upland environment, although these conclusions need to be validated with larger data sets. It was found that:

1. A significant relationship exists between L-band VV backscatter and stem biomass estimates derived from intensive field survey.
2. Topographic variation influences the amount of backscatter directly as a result of viewing geometry and indirectly as a determinant of biomass production. This latter point limits the use of age as a surrogate for biomass.

5. ACKNOWLEDGEMENTS.

This research was funded by NERC studentship GT4/91/TLS/62. I am grateful to the U.K. Forestry Commission for supplying the ground data, the sponsors of MAC Europe for supplying the AIRSAR data, the Commission of the European Communities for the POLTOOL software, and Giles Foody for comments during the editing stages.

6. REFERENCES.

Coutts, M. P. and Philipson, M. P., 1978, "Tolerance of Tree Roots to Waterlogging. 1. Survival of Sitka spruce and Lodgepole pine," *New Phytology*, vol. 80, pp. 63-69.

Curran, P. J. and S. Plummer, 1992, "Remote Sensing of Forest Productivity," *NERC News*, vol. 20, pp. 22-23.

Groom, G. B., Mitchell, P. L., Baker, J. R., Settle, J. J. and Cordey, R. A., 1992, "Relationships of Backscatter to Physical Characteristics of Pine Stands in Thetford Forest, U.K.," *MAESTRO-1/AGRISCATT, Radar Techniques for Forestry and Agricultural Applications. Final Workshop, ESA, ESTEC, Noordwijk, The Netherlands*, 1, pp. 137-141.

Kasischke, E. S. and Christensen, N. L., 1990, "Connecting Forest Ecosystem and Microwave backscatter models," *International Journal of Remote Sensing*, Vol. 11, no. 7, pp. 1277-1298.

Kasischke, E. S., Bourgeau-Chevez, L. L., Christensen, N. L., and Dobson, M. C., 1991, "The Relationship Between Above-ground Biomass and Radar Backscatter as Observed in Airborne SAR Imagery," *Proceedings of the third AIRSAR workshop, May 23-24, 1991, Pasadena, JPL Pub. 91-30*, JPL, Pasadena, pp. 11-21.

LeToan, T., Beaudoin, A., Riom, J. and Guyon, D., 1992, "Relating Forest Biomass to SAR data," *IEEE Transactions on Geoscience and Remote Sensing*, Vol. 30, pp. 403-411.

Luckmann, A.J., and Baker, J.R., 1993, "AIRSAR Observations of a Temperate Forest and Modelling of Topographic Effects," Presented at the 25th International Symposium, Remote Sensing and Global Environment Change, Graz, Austria, 4-8 April 1993.

N95- 23944

FOREST INVESTIGATIONS BY POLARIMETRIC AIRSAR DATA IN THE HARZ MOUNTAINS *

M. Keil, D. Poll, J. Raupenstrauch, T. Tares**, R. Winter
German Aerospace Research Establishment (DLR),
D–82234 Oberpfaffenhofen, Germany
** Helsinki Univ. of Technology, Lab. of Space Technology,
SF–02150 Espoo, Finland

1. INTRODUCTION

The Harz Mountains in the North of Germany have been a study site for several remote sensing investigations since 1985, as the mountainous area is one of the forest regions in Germany heavily affected by forest decline, especially in the high altitudes above 800 m. In a research programme at the University of Berlin, methods are developed for improving remote sensing assessment of forest structure and forest state by additional GIS information, using several datasets for establishing a forest information system (Kenneweg, Schardt, Sagischewsky, 1992).

The Harz has been defined as a testsite for the SIR–C / X–SAR mission which is going to deliver multifrequency and multipolarizational SAR data from orbit. In a pilote project led by DLR–DFD, these data are to be investigated for forestry and ecology purposes. In a preparing flight campaign to the SIR–C / X–SAR mission, "MAC EUROPE 1991", performed by NASA/JPL, an area of about 12 km by 25 km in the Northern Harz was covered with multipolarizational AIRSAR data in the C–, L– and P–band, including the Brocken, the highest mountain of the Harz, with an altitude of 1142 m.

The multiparameter AIRSAR data are investigated for their information content on the forest state, regarding the following questions:
- information on forest stand parameters like forest types, age classes and crown density, especially for the separation of deciduous and coniferous forest,
- information on the storm damages (since 1972) and the status of regeneration,
- information on the status of forest destruction because of forest decline,
- influence of topography, local incidence angle and soil moisture on the SAR data.

Within the project various methods and tools have been developed for the investigation of multipolarimetric radar backscatter responses and for discrimination purposes, in order to use the multipolarization information of the compressed Stokes matrix delivered by JPL.

2. AVAILABLE DATA

The AIRSAR scenes were flown at July 12th, 1991. Two profiles were heading North with looking angles of 45 deg. and 55 deg., two profiles heading South, with the same looking angles. Therefore data are available representing an illumination of the mountains from the East and from the West, each profile cut into North and South scene (Keil et al., 1993).

Parallel to the survey, 70 test areas in the upper Harz have been checked at the ground for forest type and tree composition, age class, crown density, topographic features and ground cover. A LANDSAT TM scene from July 10th 1991 (two days before the AIRSAR flight) and a digital elevation model is available for comparison. Within a cooperation with the Technical University of Berlin, infrared colour photos can be used. A large progress for investigation was reached by short when about 140 polygons from airphoto interpretation of forest state and from forest management data could be integrated within this cooperation. The data overlay is based on a geocoding of three AIRSAR scenes performed by Johanneum Research, Graz, including terrain correction.

3. TOOLS FOR INVESTIGATION OF POLARIZATION DATA

In order to study signatures of polarimetric backscatter, several extensions of the available POLTOOL software by JPL were found necessary. Thus, for the synthesis of polarimetric information of target areas, an input mask file was coupled with the SYNTHESIS software based on arbitrary closed polygons (Tares, 1993).

Besides several other tools for visualization and statistical evaluations, the following representation was found very useful: The possible discrimination of two forest stands on certain polarization states can not be checked by comparing mean backscatter amplitudes alone. Thus, a deduction of standard deviation, assuming Gaussian distribution, was performed for the marked forest reference areas and given polarization states directly from the Stokes matrix (Tares, 1993). As ellipticity seemed not to have a dominant influence for discrimination, a two dimensional representation was used mainly: For co-polarization and cross-polarization, the stand-averaged backscatter amplitude +- standard deviation can be presented in dependence of orientation angle.

By known mean values M and standard deviation Sdev for two landcover classes a and b, an expected accuracy of a Bayesian classification for one feature can be estimated using the separability index (Dobson et al., 1992):

$$S(a,b) = \mathrm{abs}(M(a)-M(b)) / (\mathrm{Sdev}(a) + \mathrm{Sdev}(b)).$$

For Gaussian distribution, values of $S > 1.5$ correspond to a classification accuracy better than 90%. The new developed program "discrimination" enables a separability optimization by changing both orientation angles and ellipticity angles for pairs of forest classes(Tares,1993).

The statistical evaluations were used to prepare classification investigations. In order to take into account the speckle and textural information, first classification approaches were performed using the EBIS system (an "evidenced based interpretation system") by Lohmann, 1991, developed and installed at DLR. By this system there are supported distribution functions described by multinomial statistics besides Gaussian distributions.

4. PRESENT RESULTS

From visual interpretation and statistical evaluations, several characteristics could be deduced for the AIRSAR data of the Harz study site.

L-band data seem to deliver the best single band information for separation of deciduous and coniferous stands, when two or three characteristic polarization states can be used. This is due to the fact, that polarization response vary much more for spruce stands than for deciduous stands with changing orientation angle (showing a maximum near HH and a minimum near VV for co-polarization of spruce). Age classes are difficult to delineate in L-band alone, cultures and clearings can be detected well (Raupenstrauch, 1993). The high-level spruce stands with lower crown density can be distinguished against the denser stands in the North, for which the different texture gives also important information.

The three polarizations at P-band show the highest differenciation within the forest areas. Two influences besides crown and stem parameters seem to overlay forest information: P-band shows the strongest relations to the topography. P-HH and P-VV, not P-HV, reflect information not correlated with forest stand parameters; investigations are planned to check how far soil types, soil moisture and ground cover are responsible for that.

Weakest influences by topography are shown in the C-band. The polarization information is smaller than in L- and P-band, leading to a low differentiation between deciduous and coniferous trees. There is a higher potential for the differentiation of regeneration states (clearings / cultures) and additional information for age class separation (thickets / timber).

An example of polarimetric signatures for three different stand types is shown in Fig. 1. The spruce and the deciduous stand can be distinguished in L- and P-band, not in C-band, the orientations VV and HV seem best for that separation. VV-polarization has proved the most informative orientation for C-band, e.g. for the separation of cultures from spruce, pole and old timber (Keil et al., 1993).

For the present classifications by EBIS, datasets of L-HH, L-VV and L-HV as well as C-VV and P-HV proved a suitable base. Important for classification was the use of local incidence information which is available now in the co-registrated incidence angle mask.

5. REFERENCES

Dobson, M. C., L. Pierce, K. Sarabandi, F. T. Ulaby, T. Sharik, 1992, "Preliminary Analysis of ERS-1 SAR for Forest Ecosystem Studies", IEEE Trans. on Geoscience and Remote Sensing, Vol. 30, No. 2, pp. 203-211.

Keil, M., J. Raupenstrauch, T. Tares, R. Winter, 1993, "Investigations of Forest Information Content of Polarimetric AIRSAR Data in the Harz Mountains", 25th International Symposium, Remote Sensing and Global Environmental Change (ERIM), 4-8 April 1993, Graz, Austria (in press).

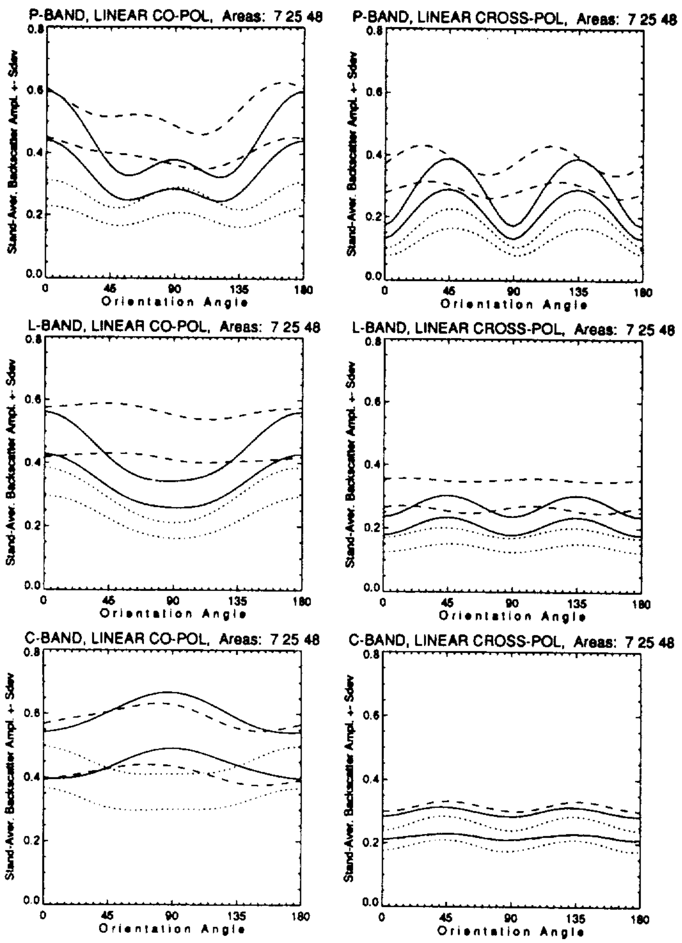

Fig. 1. Polarization signatures for three stands: ——— spruce, pole and old timber, mainly closed, slope E 5 deg. – – – deciduous stand, old timber, slope SW, 20–30 deg. . . . . culture (spruce), open, 0 deg.

Kenneweg, H.,M. Schardt, H. Sagischewski,1992, "Observation of forest damages in the Harz Mountains by Means of Satellite Remote Sensing", European "International Space Year" Conference 1992, Munich, Germany, 30 March – 4 April 1992, ESA – ISY 1, Vol II, pp. 805–810.

Lohmann, G., 1991, "An Evidential Reasoning Approach to the Classification of Satellite Images", Diss. T.U. München, DLR-FB 91-29, Oberpfaffenhofen.

Raupenstrauch, J., 1993, "Untersuchungen zum Informationsgehalt von Multi-polarisations- und Multifrequenz-SAR-Daten, insbesondere für forstliche Fragestellungen, unter Verwendung von anderen Fernerkundungs- und von Zusatzdaten", thesis for diploma, Ludwig Maximilian University of Munich.

Tares,T., 1993, "AIRSAR Software – Programs for Preprocessing of JPL Compressed Polarimetric SAR Data", Internal Report, DLR, Oberpfaffenhofen.

COMPARISON OF INVERSION MODELS USING AIRSAR DATA FOR DEATH VALLEY, CALIFORNIA

Kathryn S. Kierein-Young

Center for the Study of Earth from Space (CSES)
Cooperative Institute for Research in Environmental Sciences (CIRES)
University of Colorado, Boulder, Colorado 80309-0449
and
Department of Geological Sciences
University of Colorado, Boulder, Colorado 80309

1. INTRODUCTION

Polarimetric Airborne Synthetic Aperture Radar (AIRSAR) data were collected for the Geologic Remote Sensing Field Experiment (GRSFE) over Death Valley, California, USA, in September 1989 (Evans and Arvidson, 1990; Arvidson et al, 1991). AIRSAR is a four-look, quad-polarization, three frequency instrument. It collects measurements at C-band (5.66 cm), L-band (23.98 cm), and P-band (68.13 cm), and has a GIFOV of 10 meters and a swath width of 12 kilometers. Because the radar measures at three wavelengths, different scales of surface roughness are measured. Also, dielectric constants can be calculated from the data (Zebker et al, 1987).

The scene used in this study is in Death Valley, California and is located over Trail Canyon alluvial fan, the valley floor, and Artists Drive alluvial fan. The fans are very different in mineralogic makeup, size, and surface roughness. Trail Canyon fan is located on the west side of the valley at the base of the Panamint Range and is a large fan with older areas of desert pavement and younger active channels. The source for the material on southern part of the fan is mostly quartzites and there is an area of carbonate source on the northern part of the fan. Artists Drive fan is located at the base of the Black Mountains on the east side of the valley and is a smaller, young fan with its source mostly from volcanic rocks. The valley floor contains playa and salt deposits that range from smooth to Devil's Golf Course type salt pinnacles (Hunt and Mabey, 1966).

2. CALIBRATION

The AIRSAR data were calibrated to allow extraction of accurate values of rms surface roughness, dielectric constants, sigma-zero backscatter, and polarization information. The data were calibrated in two ways, assuming a flat surface, and using a digital elevation model to remove topographic effects. Both calibrations used in-scene trihedral corner reflectors to remove cross-talk, and to calibrate the phase, amplitude, and co-channel gain imbalance (van Zyl, 1990). The altitude of the aircraft was measured incorrectly because the plane was flying over the Panamint mountains and imaging the valley floor. This was corrected in the calibration in both cases. A digital elevation model (DEM) was generated by digitizing four USGS topographic quads using Arc/Info. This DEM was registered to the radar scene and used in the calibration to remove the effects of topography (van Zyl et al, 1992). The near-range part of the image contains Trail Canyon fan which slopes away from the radar look direction and has the largest topographic effect. Artists Drive fan, in the far range, has a gentle slope which did not effect the calibration greatly. The corner reflectors used in the calibration were located on Trail Canyon fan. In the calibration without the DEM correction, the calibrated polarization signatures for the corner reflectors were not ideal. However, once the DEM was used, the calibrated signatures were much better. Figure 1 shows before and after DEM calibration polarization signatures for a corner reflector in C-band. Also, the sigma-zero values changed slightly with the DEM correction. Areas that face away from the radar look direction due to topography have DEM corrected sigma-zero values that are greater than (less negative) those that are DEM uncorrected. Areas that face toward the radar look direction have DEM corrected sigma-zero values that are less than (more negative) those that are DEM uncorrected. Areas that are flat, without topography, have sigma-zero values that are the same in both calibrations.

3. INVERSION AND ANALYSIS

The first-order small perturbation model (Evans et al, 1992; van Zyl et al ,1991; Barrick and Peake, 1967) was used to estimate the surface power spectral density and the dielectric constant at every pixel by performing an inversion using the AIRSAR data. This model is valid only for very smooth surfaces. Results from the small perturbation model inversion are three values, one for each of the radar frequencies, that describe the power spectral density of the surface and a value for the dielectric constant at each frequency. The power spectrum of a geologic surface is approximately linear in log-log space. Fitting the three points from the inversion with a line using a least-squares method produces slope and intercept values that allow calculation of the fractal dimension of the surface and a rms surface roughness value. The slope of the power spectrum is related to the two-dimensional fractal dimension of the surface. The fractal dimension of a surface describes the scaling properties of the topography (Mandelbrot, 1982). A surface may have a fractal dimension between 2 and 3 and as the fractal dimension increases, heights of nearby points become more independent (Brown and Scholz, 1985). The intercept of the power spectrum can be directly related to a rms surface roughness using forward modelling. Using the fractal dimension and rms surface roughness calculated from the radar inversion power spectrum, a synthetic three dimensional plot can be made that represents the surface (Huang and Turcotte, 1989; Kierein-Young and Kruse, 1992).

A modified small perturbation model (van Zyl, personal communication; Zebker et al, 1991) was also used to estimate the rms surface height and dielectric constant at every pixel by performing an inversion using the AIRSAR data. This model modifies the small perturbation model to extend the validity range to all surfaces by including an empirically derived function that approximates the change in roughness with backscatter. Two versions of the modified small perturbation model inversion were used. The first assumes a constant value for the slope of the power spectrum. The second method uses, at every pixel, the power spectrum slope obtained from the small perturbation model inversion. Results from both the modified small perturbation models are values for the rms surface roughness and dielectric constant for each frequency.

4. RESULTS AND CONCLUSIONS

The results from the three inversion models are shown in Table 1 compared with field data for five sites. These five sites consist of three alluvial fan units, a playa, and Devil's Golf Course type salt pinnacles. The active fan site is from the most active channel on Trail Canyon fan, the desert pavement site is also from Trail Canyon fan, and the third site is from Artists Drive fan. Field surface roughness data were obtained from digitized helicopter stereo pairs (Farr, personal communication) of each site and from an USGS Open File Report (Schaber and Berlin, 1993). Field dielectric measurements were made with a C-Band dielectric probe. In general, the results from the small perturbation model underestimates the value of surface roughness. In both of the modified small perturbation models, the surface roughness values generally increase with frequency. The roughness values in the model with a constant power spectrum slope value (y) are larger than those from the model using the power spectrum slope from the small perturbation model. The P-Band data seem to match the field data more closely than the other bands. However, this may be because of the dielectric values. The dielectric values are most reasonable in the small perturbation model. The dielectric values in the modified models are too high except in P-Band. The modified small perturbation model was tried assuming a dielectric constant equal to 3.0 for every pixel. This inversion produced surface roughness values that were too large in most cases.

Using inversion models to obtain surface roughness and dielectric constants from AIRSAR data produces quantitative results that are reasonably accurate. The small perturbation model tends to give the overall best results for dielectric constants. C-band and L-band data in the modified small perturbation model tend to produce dielectric constants that are too high. P-band data in the modified model produces the best overall results for both surface roughness and dielectric constant. The results from the modified model with a constant power spectrum slope are similar to those of the model with variable power spectrum slopes. Since surfaces do show differences in their power spectrum slopes, it is more accurate to include this variation in the inversion model. The results of these inversion models can be used to help in determining the active surficial processes and the age of alluvial fan surfaces. Combining the inversion results with data from other sensors can help to determine why roughness characteristics are spatially variant (Kierein-Young and Kruse, 1991). For example, the north part of Trail Canyon fan has a lower surface roughness than the rest of the fan. This difference is due to a different, more easily eroded source material.

5. ACKNOWLEDGEMENTS

Portions of this work were supported under a NASA Graduate Student Researchers Grant NGT-50728. Portions of this work were supported under the SIR-C project by NASA/JPL contract 958456. Field work was supported by a grant from the Department of Geological Sciences, University of Colorado.

6. REFERENCES

Arvidson et al., 1991. GRSFE CD-ROM and documentation, version 1: USA_NASA_PDS_GR_0001, Planetary Data System, NASA (9 CD-ROMs).

Barrick, D. E., and W. H. Peake, 1967. Scattering form surfaces with different roughness scales: Analysis and interpretation, Research Rept. No. BAT-197A-10-3, Battelle Memorial Institute, Columbus Laboratories, Columbus, Ohio, AD 662751.

Evans, D. L., and Arvidson, R. E., 1990. The Geologic Remote Sensing Field Experiment (GRSFE): Overview of initial results: in Proceedings, IGARSS '90, University of Maryland, College Park, Md., The Institute of Electrical and Electronics Engineers, Inc. (IEEE), New York, p. 1347.

Evans, D. L., T. G. Farr, and J.J. van Zyl, 1992. Estimates of surface roughness derived from synthetic aperture radar (SAR) data, IEEE Transactions on Geoscience and Remote Sensing, V. 30, No. 2, pp. 382-389.

Huang, J. and D. L. Turcotte, 1989. Fractal mapping of digitized images: Application to the topography of Arizona and comparisons with synthetic images, Journal of Geophysical Research, V. 94, No. B6, pp. 7491-7495.

Hunt, C. B. and D. R. Mabey, 1966. Stratigraphy and structure in Death Valley, California. U. S. Geological Survey Profession Paper 494-A, 162p.

Kierein-Young, K. S.and F. A. Kruse, 1992. Extraction of quantitative surface characteristics from AIRSAR data for Death Valley, California, in Summaries of the third annual JPL Airborne Geoscience Workshop, V. 3, pp. 46-48.

Kierein-Young, K. S. and F. A. Kruse, 1991. Quantitative Investigations of Geologic Surfaces utilizing Airborne Visible/Infrared Imaging Spectrometer (AVIRIS) and Polarimetric Radar (AIRSAR) Data for Death Valley, California, in Proceedings of the Eighth Thematic Conference on Geologic Remote Sensing, V.1, pp. 495-506.

Mandelbrot, B. B., 1982. The Fractal Geometry of Nature, W. H. Freeman, San Francisco, California.

Schaber, G. G. and G. L. Berlin, 1993. Death Valley, California: Surface micro-relief statistics and radar scatterometer data, U. S. Geological Survey Open-file Report 93-272, 43p.

van Zyl, Jakob J., 1990. Calibration of Polarimetric Radar Images Using Only Image Parameters and Trihedral Corner Reflector Responses, IEEE Transactions on Geoscience and Remote Sensing, V. 28, No. 3, pp.337-348.

van Zyl, Jakob J., Charles F. Burnette and Tom G. Farr, 1991. Inference of surface power spectra from inversion of multifrequency polarimetric radar data, Geophysical Research Letters, V. 18, No. 9, pp. 1787-1790.

van Zyl, J. J., B.D. Chapman, P. C. Dubois, and A. Freeman, 1992. Polcal User's Manual, JPL D-7715 version 4.0.

Zebker, Howard A., Jakob J. van Zyl, and Daniel N. Held, 1987. Imaging Radar Polarimetry From Wave Synthesis, Journal of Geophysical Research, V. 92, No. B1, pp. 683-701.

Zebker, H. A., J. J. van Zyl, S. L. Durden, and L. Norikane, 1991. Calibrated imaging radar polarimetry: Technique, examples, and applications, IEEE Transactions on Geoscience and Remote Sensing, V. 29, No. 6, pp. 942-961.

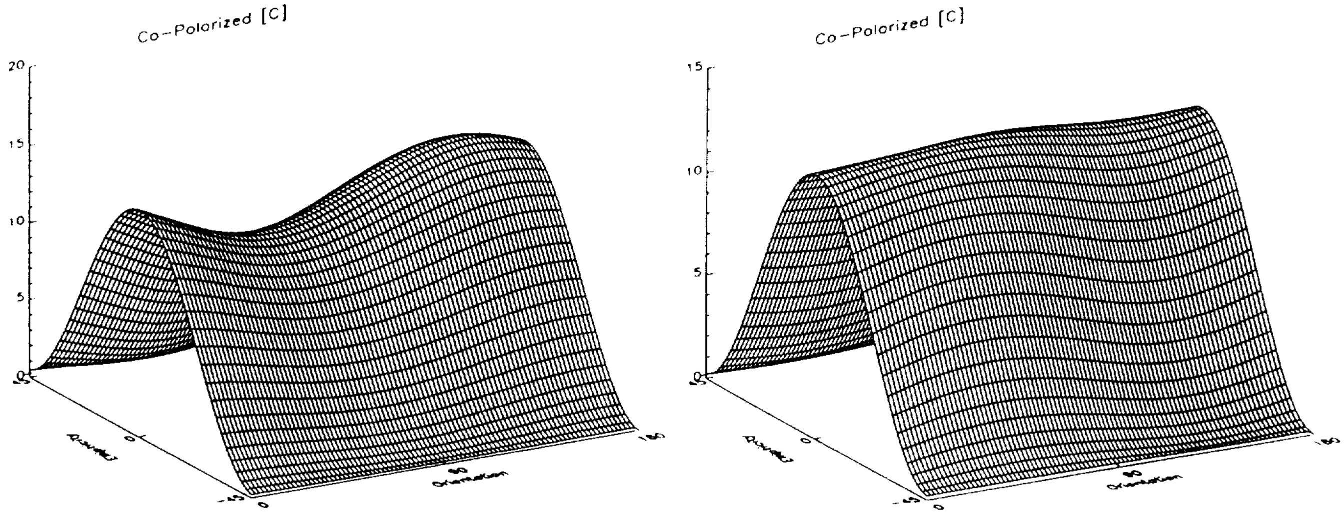

Figure 1. Co-polarized C-band corner reflector polarization signatures without DEM correction (left) and with DEM correction (right).

Table 1. AIRSAR inversion model results.

			SPM		MSPM y=2.55		MSPM y=SPM		Field	
Surface		RMS	fd	e	RMS	e	RMS	e	RMS	e
Active Fan	C	6.5	2.13	4.0	2.7	66.8	2.1	68.4	17.4	3.1
	L			3.6	6.7	27.3	5.0	27.3		
	P			3.0	10.9	4.2	10.3	3.6		
Desert Pvt Fan	C	2.0	2.18	10.3	1.4	26.9	1.2	25.7	9.8	3.0
	L			8.8	2.7	12.3	2.6	10.8		
	P			3.0	10.7	1.5	6.9	1.4		
Artists Dr. Fan	C	1.0	2.405	2.4	2.6	46.1	2.6	28.7	11.5	2.8
	L			2.3	2.5	10.0	3.4	13.6		
	P			2.7	9.4	2.1	11.8	4.3		
Playa	C	2.3	2.105	4.8	1.5	28.3	1.0	28.3	7.6	5.3
	L			10.9	0.9	26.1	0.5	20.8		
	P			2.5	6.2	3.9	9.9	3.3		
Devil's Golf Cs.	C	19.0	2.03	3.0	NGP	NGP	NGP	NGP	12.0	2.4
	L			2.5	12.1	50.7	5.7	27.5		
	P			3.0	30.3	17.7	28.2	39.4		

RMS = root mean square surface roughness in cm
fd = fractal dimension
e = dielectric constant
NGP = no good points

N95-23946

GEOLOGIC MAPPING USING INTEGRATED AIRSAR, AVIRIS, AND TIMS DATA

Fred A. Kruse

Center for the Study of Earth from Space (CSES) and Department
of Geological Sciences, University of Colorado, Boulder 80309-0449

I. INTRODUCTION

The multi-sensor aircraft campaign called the "Geologic Remote Sensing Field Experiment" (GRSFE), conducted during 1989 in the southwestern United States, collected multiple airborne remote sensing data sets and associated field and laboratory measurements (Arvidson et al., 1991). The GRSFE airborne data sets used in this study include the airborne Synthetic Aperture Radar (AIRSAR), the Airborne Visible/Infrared Imaging Spectrometer (AVIRIS), and the Thermal Infrared Multispectral Scanner (TIMS) (See Table 1). Each sensor's unique characteristics were used for this study in a combined analysis scheme for geologic mapping. AIRSAR was used to map structures and landforms, AVIRIS was used to map mineralogy, and TIMS was used to map lithology. Visual data integration using IHS transforms and combined numerical analysis using derived geophysical and geologic parameters with "multispectral" techniques resulted in improved geologic mapping over that possible using each data set individually.

TABLE 1. GRSFE Sensor Specifications

Sensor	**Wavelength range**	**Number of channels**	**Sampling Interval**	**Spatial Resolution**
AIRSAR	P, L, C bands 68.13, 23.98, 5.66 cm	3 (Quad pol)	NA	6-12 m
AVIRIS	0.41 - 2.45 µm	224	10 nm	20 m
TIMS	8.2 - 11.7 µm	6	400 - 800 nm	20 m

II. LOCATION AND GEOLOGY

The extreme northern end of Death Valley (northern Grapevine Mountains) California and Nevada, USA, has been studied in detail using field data and several remote sensing data sets (Kruse, 1988, Kruse et al., 1993). Bedrock in the area consists of limestones, dolomites, sandstones and their metamorphic equivalents along with quartz syenite, a quartz monzonite porphyry stock, and quartz monzonite dikes (Wrucke et al, 1984, Kruse, 1988). The igneous rocks are cut by narrow north-trending mineralized shear zones and slightly broader northwest-trending zones of disseminated quartz, pyrite, sericite, chalcopyrite, and fluorite mineralization (QSP alteration) as well as several small areas of quartz stockwork. Skarn, composed mainly of brown andradite garnet intergrown with calcite, epidote, and tremolite, occurs around the perimeter of the quartz monzonite stock. Tertiary volcanic rocks are abundant around the periphery of the study area. Quaternary deposits include Holocene and Pleistocene fanglomerates, pediment gravels, and alluvium.

III. AIRSAR DATA

The JPL P-, L-, and C-band airborne imaging radar polarimeter data (AIRSAR) were calibrated using Trihedral corner reflectors placed during the GRSFE experiment. The corner reflectors were not physically in the northern Grapevine Mountains scene, but in an adjacent scene in the same flightline. Calibration consisted of calibration of phase, cross-talk, co-channel imbalance, and absolute radiometry using software developed at JPL (van Zyl et al., 1992).

The AIRSAR data were converted to radar backscattering coefficient (σ^0) to allow extraction of backscatter signatures for areas indicated as having varying surface roughness on a PLC (RGB) color composite image. Selected backscatter signatures from the northern Grapevine Mountains site are shown in Figure 1. The backscatter signatures show that in general those rocks and fans that contain altered material are smoother than those that do not. This establishes a link between surface morphology and composition for these particular units. Some fans of differing composition (volcanic fans and mixed composition granitic fans) with similar spatial relations to unaltered bedrock, however, have similar backscatter signatures. A rock face perpendicular to the look direction of the AIRSAR acts, as expected, nearly as a corner reflector.

Figure 1. Radar backscatter signatures (σ^0) for selected rock units.

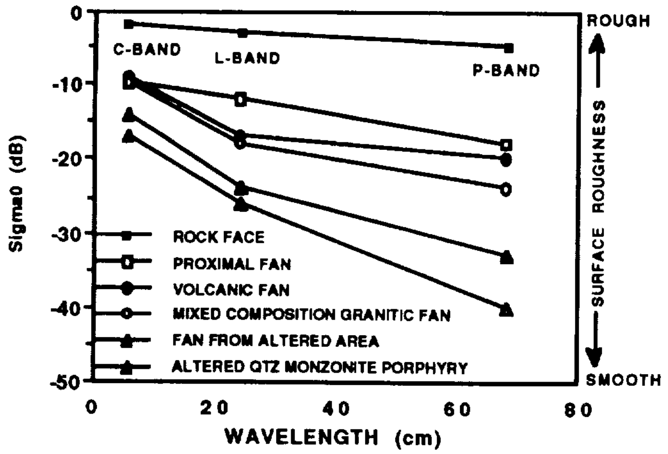

The AIRSAR data were also inverted to rms surface roughness and fractal dimension using a first-order small perturbation model (Kierein-Young, 1993). The surface roughness was calculated from the intercept of a log-log plot of the power spectral density for the PLC data and the fractal dimension from the slope. The distribution of smooth versus rough areas generally corresponded to that observed during the interactive extraction of frequency signatures above. Again, the altered areas were shown to be relatively smooth. Density sliced images of the rms roughness, however, allowed quantitative spatial mapping of several ranges of roughness.

IV. AVIRIS DATA

AVIRIS is an imaging spectrometer measuring reflected light in 224 narrow (10 nm-wide) bands between approximately 0.4 -2.45 μm (Porter and Enmark, 1987). Numerous studies have used these data for mineralogic identification and mapping based on the presence of diagnostic spectral features. Field spectra of known targets (one light, one dark) were used to calibrate the AVIRIS data to reflectance with the empirical line method (Kruse et al., 1993). Spectral signatures were extracted using interactive display and analysis software allowing identification of individual minerals and mineral mixtures (Kruse et al., 1993). An expert system was used to identify spectral endmembers and linear spectral unmixing was used to produce quantitative image-maps showing their spatial distribution. Thematic mineral maps provide detailed surface compositional information regarding secondary minerals (alteration and weathering). The results illustrate the fracture-controlled nature of most of the alteration.

V. TIMS DATA

TIMS is an aircraft scanner measuring six channels in the 8-12 μm range (Palluconi and Meeks, 1985). Silicate minerals have diagnostic emissivity minima in this spectral region (Lyon, 1965). TIMS data acquired at 13:22 local time were calibrated to radiance using gain and offset values for every scanline calculated using Planck's radiation law with the TIMS internal reference values and channel spectral responses. The radiance values were next converted to emissivity using the "model emittance" or "black body" technique described by Kahle (1987), assuming that the emissivity in TIMS band 6 was equal to 0.93. No atmospheric correction was made, however, examination of individual TIMS spectra, indicates that the emissivity calibration was adequate without the atmospheric correction, probably because of the extremely arid nature of the study area.

Color composites were made from the calibrated TIMS bands and emissivity spectra were extracted from the calibrated data for areas with known rock compositions. The principal feature of these spectra is the presence of a subtle emissivity minimum in TIMS band 3 (9.18 μm) caused by the fundamental silicon-oxygen stretching vibrations of quartz and other silicate minerals. Although the emissivity features are subdued in the TIMS spectra, the shift in the minimum from TIMS band 3 to TIMS band 4 associated with decreased silica content can be observed for several silica-poor rock units. When 4/3, 5/4, and 3/2 (RGB) emissivity ratios are used together in a color-ratio-composite image, the silica-rich areas are obvious red areas on the image, while the areas with less silica appear green to blue-green. The designed ratios and image colors were used to produce lithological maps.

VI. IMAGE INTEGRATION FOR VISUAL INTERPRETATION

All of the data sets were co-registered to a map base using a DEM. Combinations of the diverse data sets were then made using the Intensity, Hue, Saturation (IHS) transform (Gillespie et al.,1986). In this procedure, the color image to be overlain is transformed from the RGB coordinate system into the IHS system, the intensity is replaced by a single-band base image, and the new IHS coordinates are transformed back to RGB. This preserves the colors from the original color image while allowing use of the base image to modulate the brightness. Several image combinations were made that enhanced the usefulness of the data for geologic mapping. The geology and alteration maps produced in the field were overlain on the radar data. These images allowed verification of the field mapping. Additionally, the alteration overlay on the radar data showed previously unrecognized structural control of alteration. TIMS data overlain on L-band AIRSAR showed additional associations of lithology and structure. The most useful image utilizing combined radar and optical remote sensing, however, was the combination of the P-, L-, C-band (RGB) image with the AVIRIS mapping results. These images and the σ^0 signatures show that roughness information is linked to composition obtained from the optical remote sensing. For example, the areas that appear smooth at P- and L-band and rough at C-band are judged to have 5 cm-scale surface relief. The AVIRIS analysis indicates that these areas also have abundant alteration minerals (sericite). One interpretation of these associations might be that the altered areas have reduced the surface relief relative to surrounding rocks. This is supported by field work, which shows that these areas correspond to highly altered rocks that have been weathered to a desert-pavement-like surface.

VII. COMBINED ANALYSIS OF DERIVED DATA SETS

The coregistered derivative data sets were combined into a "data cube" for statistical and multispectral analysis. Derived data sets used included surface roughness and fractal dimension from the AIRSAR data, mineral abundance images from the AVIRIS data, and emissivity ratio images from the TIMS data. "Spectral" and supervised classification methods were used on the combined data set to produce image maps showing broad geomorphic units with common roughness, lithological, and alteration characteristics. These images support the previous link between surface roughness and composition while providing spatial maps showing the associations and distribution.

VIII. CONCLUSIONS

The integrated multispectral images are providing new geologic information that can be used for lithologic and structural mapping to assist development of geologic models. The AIRSAR data provide information about the surface morphology of rocks and soils and the scale of surface roughness. They allow definition of geomorphic units which indicate that there is a link between surface morphology and composition for some units. The AVIRIS data allowed direct compositional mapping of surface mineralogy. The TIMS extended spectral signatures provide compositional information not contained in the visible, near-infrared or short wave infrared data. The TIMS spectra and images were useful for mapping lithological differences between igneous rock types because

TIMS is particularly sensitive to silica content. They also showed several areas of very high silica concentrations corresponding to silicified (altered) outcrop. The integrated multispectral images provide a case study of the characteristics of these diverse data sets and their capabilities for geologic mapping. The combined analyses of these data demonstrates that improved lithological, mineralogical, and structural mapping is possible using remote sensing, even where extensive, detailed ground mapping has been completed.

The next step in this study is to use the GRSFE and other data sets to extend the analysis to a regional scale. Extension of the study area to include much of the northern Death Valley region is in progress. SIR-C data will be used in conjunction with AVIRIS and TIMS to produce detailed geologic maps that will allow development of regional geologic models for the evolution of igneous, metamorphic, and sedimentary rocks and recent geologic surfaces.

IX. ACKNOWLEDGEMENTS

Portions of this work were supported by NASA Grants NAGW-1143 and NAGW-1601. Additional support for analysis of AIRSAR data was provided by NASA/JPL grant 958456.

X. REFERENCES

Arvidson et al., 1991, GRSFE CD-ROM and documentation, version 1: USA_NASA_PDS_GR_0001, Planetary Data System, NASA (9 CD-ROMs).

Gillespie, A. R., Kahle, A. B., and Walker, R. E., 1986, Color enhancement of highly correlated images. I. Decorrelation and HSI contrast stretches: Remote Sensing of Environment, v. 20, p. 209-235.

Kahle, A. B., 1987, Surface emittance, temperature, and thermal inertia derived from Thermal Infrared Multispectral Scanner (TIMS) data for Death Valley, California, Geophysics, v 52, no. 7, p. 858-874.

Kierein-Young, K. S., 1993, Comparison of inversion models using AIRSAR data for Death Valley, California, in Summaries, 4th Airborne Geoscience Workshop, 25-29 October, 1993, Washington, D. C., (in press).

Kruse, F. A., 1988, Use of Airborne Imaging Spectrometer data to map minerals associated with hydrothermally altered rocks in the northern Grapevine Mountains, Nevada and California: Remote Sensing of Environment, V. 24, No. 1, p. 31-51.

Kruse, F. A., Lefkoff, A. B., and Dietz, J. B., 1993, Expert System-Based Mineral Mapping in northern Death Valley, California/Nevada using the Airborne Visible/Infrared Imaging Spectrometer (AVIRIS): Remote Sensing of Environment, Special issue on AVIRIS, May-June 1993, p. 309 - 336.

Lyon, R. J. P., 1965, Analysis of rocks by spectral infrared emission (8 to 25 microns): Economic Geology, v. 60, p. 715-736.

Palluconi, F. D. and G. R. Meeks, 1985, Thermal Infrared Multispectral Scanner (TIMS): An investigator's guide to TIMS data, JPL Publication 85-32, Jet Propulsion Laboratory, Pasadena, CA, 14 p.

Porter, W. M., and Enmark, H. T., 1987, A system overview of the Airborne Visible/Infrared Imaging Spectrometer (AVIRIS): in Proceedings, 31st Annual International Technical Symposium, Society of Photo-Optical Instrumentation Engineers, v. 834, p. 22-31.

Wrucke, C. T., Werschky, R. S., Raines, G. L., Blakely, R. J., Hoover, D. B., and Miller, M. S., 1984, Mineral resources and mineral resource potential of the Little Sand Spring Wilderness Study Area, Inyo County, California: U.S. Geological Survey Open File Report 84-557, 20 p.

van Zyl, J. J., Chapman, B. D., Dubois, P. C., and , Freeman, A., 1992, POLCAL User's Manual, Version 4.0, JPL D-7715, Jet Propulsion Laboratory, Pasadena, CA.

N95- 23947

STATISTICS OF MULTI-LOOK AIRSAR IMAGERY: A COMPARISON OF THEORY WITH MEASUREMENTS

J.S. Lee, K.W. Hoppel and S.A. Mango

Remote Sensing Division, Code 7230
Naval Research Laboratory
Washington DC 20375-5351

1. INTRODUCTION

The intensity and amplitude statistics of SAR images, such as L-Band HH for SEASAT and SIR-B, and C-Band VV for ERS-1 have been extensively investigated for various terrain, ground cover and ocean surfaces. Less well-known are the statistics between multiple channels of polarimetric or interferometric SARs, especially for the multi-look processed data. In this paper, we investigate the probability density functions (PDFs) of phase differences, the magnitude of complex products and the amplitude ratios, between polarization channels (i.e. HH,HV, and VV) using 1-look and 4-look AIRSAR polarimetric data. Measured histograms are compared with theoretical PDFs which were recently derived based on a complex Gaussian model (Lee et al., 1993).

NASA/JPL 1-look and 4-look AIRSAR data of Howland Forest and San Francisco were used for comparison. Histograms from 1-look SAR data agreed with theoretical PDFs. However, discrepancies were found when matching the 4-look polarimetric data with the 4-look PDFs. Instead, We found that the 3-look PDFs matched better. The problem was traced to the averaging of correlated 1-look pixels. We also verified these theoretical PDFs for forest, ocean surfaces, park areas and city blocks. This indicates that ground cover and terrain with different scattering mechanisms can be represented with this statistical model.

2. THE COMPLEX GAUSSIAN MODEL

A polarimetric radar measures the complete scattering matrix S of a medium at a given incidence angle. For a reciprocal medium, the three unique complex elements are S_{hh}, S_{hv}, and S_{vv}. Circular Gaussian Conditions (Goodman, 1985) are assumed. The circular Gaussian assumption has been verified by Sarabandi(1992) using 1-look polarimetric SAR data.

The multi-look AIRSAR processor compresses polarimetric data by averaging Mueller matrices of 1-look pixels in the azimuth direction. Due to oversampling, the neighboring 1-look pixels of AIRSAR data are somewhat correlated. For mathematical simplicity, the PDFs for multi-look phase difference, etc. were derived under the assumption of statistical independence.

3. MULTI-LOOK PHASE DIFFERENCE DISTRIBUTION

Let n be the number of looks, and $S_1(k)$ and $S_2(k)$ be the *kth* 1-look samples of any two components of the scattering matrix. For polarimetric and interferometric radars, the multi-look phase difference is obtained by

$$\psi = Arg[\frac{1}{n}\sum_{k=1}^{n} S_1(k)\, S_2^*(k)] \tag{1}$$

Under the circular Gaussian assumption, the multi-look phase distribution were derived by multiple integrations of special functions (Lee et al., 1993). The multi-look phase difference PDF is

$$p(\psi) = \frac{\Gamma(n+1/2)\,(1-|\rho_c|^2)^n \beta}{2\sqrt{\pi}\,\Gamma(n)\,(1-\beta^2)^{n+1/2}} + \frac{(1-|\rho_c|^2)^n}{2\pi} F(n, 1; 1/2; \beta^2), \tag{2}$$

with

$$\beta = |\rho_c|\, Cos(\psi-\theta), \quad -\pi < \psi \le \pi \tag{3}$$

where $F(n, 1; 1/2; \beta^2)$ is a Gauss hypergeometric function, and θ and $|\rho_c|$ are the phase and the magnitude of the complex correlation coefficient defined as

$$\rho_c = \frac{E[S_1 S_2^*]}{\sqrt{E[|S_1|^2]\, E[|S_2|^2]}} = |\rho_c|\, e^{i\theta} \tag{4}$$

The 1-look (n=1) PDF can be obtained by applying mathematical identities of the hypergeometrical function (Lee et al.,1993). The 1-look PDF obtained is identical to that of Kong (1988) and Sarabandi (1992). The PDF of Eq.(2) depends only on the number of looks and the complex correlation coefficient. The peak of the distribution is located at $\psi=\theta$. A plot of standard deviation versus $|\rho_c|$ is given in Fig. 1, which verifies a similar but less accurate figure (Zebker, 1992) computed with interferometric radar data. As shown in Fig. 1, multi-look processing effectively reduces the phase error, especially when n=16 and 32.

4. DISTRIBUTION OF THE MAGNITUDE OF THE NORMALIZED MULTI-LOOK COMPLEX PRODUCT

The magnitude of product of S_1 and S_2 is an important measure in polarimetric SAR, and it is the magnitude of interferogram from an interferometric SAR. The normalized magnitude is defined as

$$\xi = \frac{|\frac{1}{n}\sum_{k=1}^{n} S_1(k)\, S_2^*(k)|}{\sqrt{E[|S_1|^2]\, E[|S_2|^2]}} \tag{5}$$

The PDF of ξ (Lee et al.,1993) is

$$p(\xi) = \frac{4 n^{n+1} \xi^n}{\Gamma(n)\,(1-|\rho_c|^2)}\, I_0\left(\frac{2|\rho_c| n\xi}{1-|\rho_c|^2}\right) K_{n-1}\left(\frac{2n\xi}{1-|\rho_c|^2}\right) \tag{6}$$

where $I_0(\ )$ and $K_n(\ )$ are modified Bessel functions. The PDF for the unnormalized magnitude can be easily obtained from Eq.(6) by using Eq. (5). The standard deviations of this PDF is plotted versus the correlation coefficient in Fig. 2. This plot indicates that the magnitude of complex product can be used as a discriminator, especially for large n.

5. MULTI-LOOK AMPLITUDE RATIO DISTRIBUTIONS

The amplitude ratio between S_{hh} and S_{vv} has been an important discriminator in the study of polarimetric radar returns. Let the normalized ratio

$$v=\sqrt{\left(\sum_{k=1}^{n}|S_1(k)|^2/E[|S_1|^2]\right)/\left(\sum_{k=1}^{n}|S_2(k)|^2/E[|S_2|^2]\right)} \qquad (7)$$

The multi-look amplitude ratio PDF (Lee et al., 1993) is

$$p(v)=\frac{2\Gamma(2n)\,(1-|\rho_c|^2)^n\,(1+v^2)\,v^{2n-1}}{\Gamma(n)\,\Gamma(n)\,[(1-v^2)^2-4|\rho_c|^2v^2]^{n+1/2}}\,,\quad 0\le v<\infty \qquad (8)$$

For n=1, we have the 1-look amplitude distribution, which is identical to the results of Kong(1988), when his PDF is properly normalized.

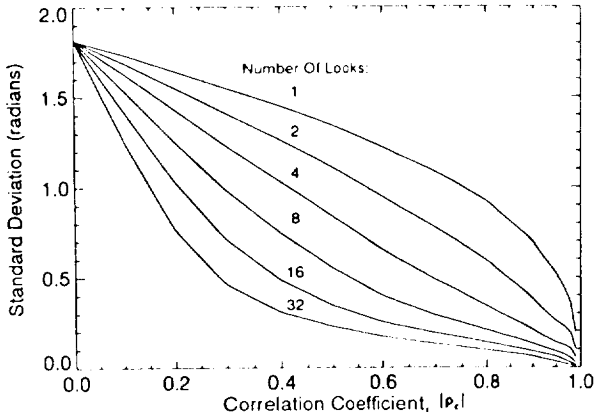

Fig. 1 Phase difference standard deviations versus the correlation coefficient, $|\rho_c|$, for the number of look from n= 1, 2, 4, 8, 16 and 32. The value of θ=0.

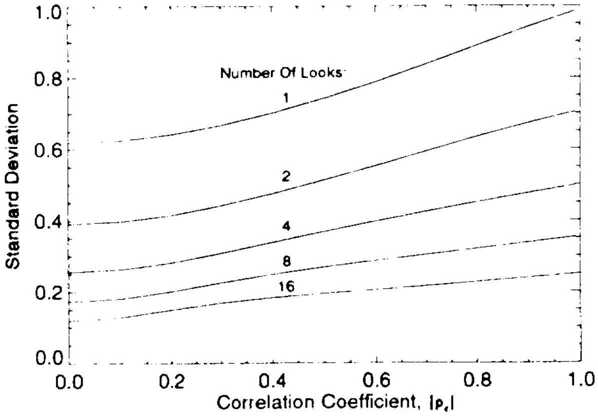

Fig. 2 Standard deviations of Normalized magnitude of multi-look interferogram versus correlation coefficient, $|\rho_c|$, for the number of look from n= 1, 2, 4, 8 and 16.

6. COMPARISON OF THEORETICAL PDFs WITH AIRSAR MEASUREMENTS

In this section, the AIRSAR polarimetric data was used to compute histograms of phase differences, normalized products and amplitude ratios to verify this complex Gaussian model. Homogeneous regions of forest were selected, and the complex correlation coefficient (i.e., θ and $|\rho_c|$) and histograms were computed. We have checked the 1-look C-Band and L-Band data, and found that the agreements between histograms and their corresponding PDFs are good. However, discrepancies exist in the 4-look data. Using 4-look Howland Forest data (CM1084), the match between the histogram and the 4-look phase difference PDF are not as good (Fig. 3A). A better match was found with a 3-look PDF (Fig. 3B). Histograms of amplitude and normalized product are also shown good agreements with 3-look PDFs. To save space, only the case of HH to VV ratio is shown in Fig. 3C.

The problem was traced to the averaging of correlated 1-look neighboring pixels during the multi-look processing. To verify it, we use 1-look data of Howland Forest (HR1084C) and perform the 4-look processing by averaging four pixels separated by two pixels in the azimuth direction. Since the correlation between every other pixels is much less than that between its immediate neighbors, statistical independence is assured. The results are shown in Fig.4 for all three variables under study. The agreement with 4-look PDFs is very good. We can conclude that due to the correlation of 1-look data, the 4-look AIRSAR data has the characteristics of a 3-look.

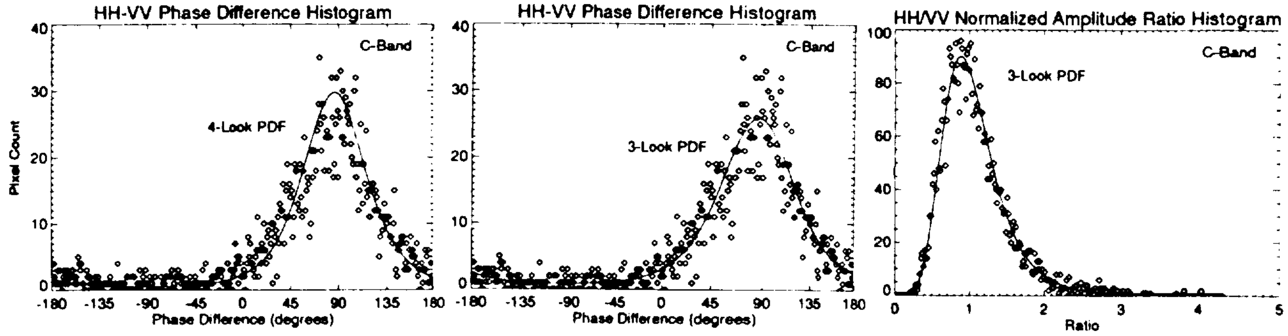

Fig. 3 Experimental results using 4-look AIRSAR data of Howland Forest (CM1804) with $|\rho_c|=0.491$ and $\theta=84.9°$. (A) The histogram of phase difference between HH and VV and the theoretical 4-look PDF. (B) The same histogram but with a 3-look PDF. The match is better. (C) The histogram of normalized amplitude ratio, HH/VV and the 3-look PDF.

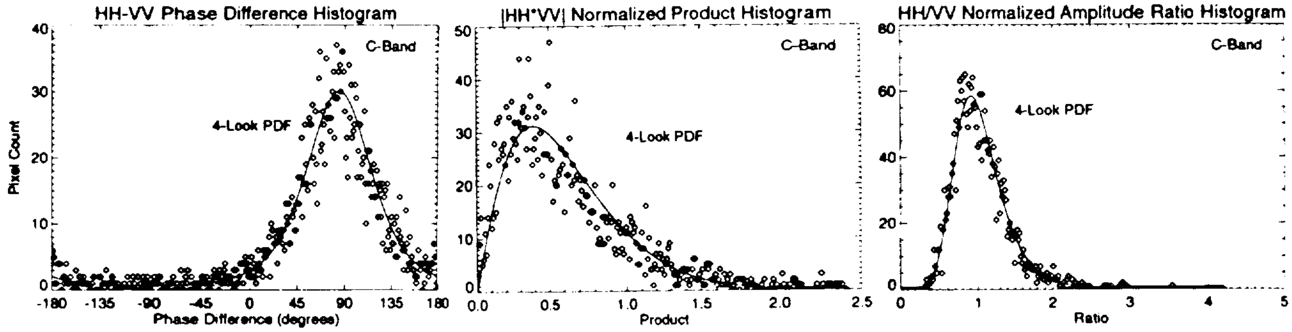

Fig. 4 Using 1-look AIRSAR data (HR1084C), the 4-look data were computed by averaging pixels separated by a distance of two pixels. (A) HH-VV phase difference histogram and the 4-look PDF. The agreement is good. (B) The histogram of normalized $|HH^*VV|$ and the 4-look PDF. (C) The histogram of normalized $|HH|/|VV|$ and the 4-look PDF.

REFERENCES

[1] Goodman, J.W., 1985, *Statistical Optics*, John Wiley and Sons, New York, 1985.

[2] Kong, J.A., et al., 1988, " Identification of Terrain Cover Using the Optimal Polarimetric Classifier," J. Electro. Waves Applic., 2(2) 171-194.

[3] Lee, J.S., K.W. Koppel, S.A. Mango and A.R. Miller, 1993,"Intensity and Phase Statistics of Multi-look Polarimetric SAR Imagery," Proceedings of IGARSS'93.

[4] Sarabandi, K., 1992, "Derivations of Phase Statistics from the Mueller Matrix", Radio Science, 27(5), 553-560.

[5] Zebker, H. A., and Villasenor, J.,1992, "Decorrelations in Interferometric Radar Echoes," IEEE Geoscience and Remote Sensing, vol.30, no. 5, 950-959.

AIRSAR DEPLOYMENT IN AUSTRALIA, SEPTEMBER 1993: MANAGEMENT AND OBJECTIVES

A. K. Milne
Centre for Remote Sensing and GIS
University of New South Wales
PO Box 1
Kensington, NSW 2033

I. J. Tapley
CSIRO Division of
Exploration and Mining
Private Bag, P.O.
Wembley, WA 6014

1. INTRODUCTION

Past co-operation between the NASA Earth science and Applications Division and the CSIRO and Australian university researchers has led to a number of mutually beneficial activities. These include the deployment of the C-130 aircraft with TIMS, AIS, and NS001 sensors in Australia in 1985; collaboration between scientists from the USA and Australia in soils research whcih has extended for the past decade; and in the development of imaging spectroscopy where CSIRO and NASA have worked closely together and regularly exchanged visiting scientists. In may this year TIMS was flown in eastern Australia on board a CSIRO-owned aircraft together with a CSIRO-designed CO_2 laser spectrometer.

The Science Investigation Team for the Shuttle Imaging Radar (SIRC-C) Program includes one Australian Principal Investigator and ten Australian co-investigators who will work on nine projects related to studying land and near-shore surfaces after the Shuttle flight scheduled for April 1994.

This long-term continued joint collaboration was progressed further with the deployment of AIRSAR downunder in September 1993. During a five week period, the DC-8 aircraft flew in all Australian states and collected data from some 65 individual test sites (Figure 1).

2. MANAGEMENT

The deployment preparations were directed by a management team comprising representatives of the CSIRO Office of Space Science Applications (COSSA); CSIRO Division of Exploration and mining; the University of New South Wales and the Australian Mining Industry Research Association, with NASA HQ and COSSA acting as the signatories for the mission.

In April 1993 a five-day Radar Image Processing and Applications workshop was held in Sydney for the participating investigators. In addition to presenting a theoretical background to the processing of multi-polarised data sets, the workshop sought to outline SAR calibration and ground sampling procedures; evaluate current applications of SAR in geology, vegetation, soils and soil moisture and sea-state investigations; examine the interferometric mode of SAR for surface mapping and to provide participants with hands on experience in basic image processing of radar data. Guest speakers and workshop leaders included Craig Dobson from the University of Michigan, Anthony Freeman from JPL and Fred Kruse from the University of Colorado.

During the deployment data was acquired for:

i) NASA/Australian collaborative projects;

ii) SIR-C calibration investigations;

iii) specific CSIRO-based research programs; and

iv) a series of individual investigations for government agencies and private sector sponsors.

Towards the end of 1994 an evaluation workshop will be held to discuss the results of the mission and allow individual investigators to present their findings.

3. SCIENCE OBJECTIVES

Radar remote sensing technology is comparatively untried, unresearched and unproven in Australian terrains. SIR-A and SIR-B data in the early 1980's did provide limited opportunities to investigate and map selected geological and vegetational patterns (Richards et al. 1987).

One of the major objectives of this deployment is to determine the contribution of AIRSAR and TOPSAR datasets to landform determination and structural mapping in regolith dominated terrains. One CSIRO research project sponsored by mineral exploration companies has the following aims:

i) To differentiate surficial regolith materials on the basis of their surface roughness and dielectric characteristics, especially weathered rock outcrop, lag gravels, soils and vegetation in both mafic and felsic terrains, and to quantitatively analyse the radar frequency information and the polarimetric signatures that describe each land component. Information describing these surface variables should allow recognition of the three fundamental regimes of a weathered landscape, that is residual, erosional and depositional. It is anticipated that the processed radar data will provide significant information concerning the degree of weathering, wind and/or water erosion processes, and on interpretation of patterns of sedimentation and relative disposition within the dispositional units;

ii) To display subtle geomorphological features (micro-relief) involving relief escarpments, drainage and various landforms which may be surface indicators of subsurface geological structures of exploration significance;

iii) To investigate the capability of polarimetric radar data to map sub-surface geometries and subtle hidden structures in areas of thinly-covered, gently dipping strata;

iv) To determine the optimum viewing and imaging parameters for future use of satellite and airborne radars for regolith-landform and geological mapping in the Australian semi-arid and arid zones; and

v) To generate high resolution digital elevation models of the study areas using TOPSAR radar interferometry. The models will be used to geometrically rectify the AIRSAR polarimetric and ERS-1 SAR data respectively and to assist definition of landform regimes, regolith characteristics, sources of materials and local regolith stratigraphy. These topographic datasets will be registered to other remotely-sensed, geological, geophysical and geochemical datasets and used for fault mapping and identification, terrain analysis and terrain processes analysis, and establishing geochemical dispersion processes and patterns.

Another major objective includes investigating the use of radar for vegetation mapping in forests, woodlands and rangeland environments and for testing models developed to account for the full interaction of backscatter from different tree morphologies over diffuse ground. A number of investigations are centred in the Northern Territory extending along a transect from near Darwin in the north to Katherine in the south. This transect provides a climatically determined gradient which brings a transition from wetlands, tropical forests and woodlands, savanna grassland to semi-arid and deserts. The accurate discrimination of these biomes and their boundary effects are seen as crucial to the spatial modelling of ecosystems at both a local and a global scale.

Land degradation processes associated with salinity and altered groundwater conditions will be studied in a number of sites throughout Australia. One site, Kerang in Central Victoria, will be used as a major calibration site for the forthcoming SIR-C mission as well as for hydrogeology.

A joint NASA/Australia project in the Great Sandy Desert region of Western Australia will use both AIRSAR and TOPSAR data for detailed reconstruction of Australia's palaeoclimate and palaeohydrology during the Late Quaternary period. It is anticipated that these datasets will assist in:

- mapping ancient shoreline ridges defining the extent and height of former lakes;

- mapping lacustrine units and distinct flood sedimentation units such as slackwater deposits; and

- identifying levee systems of prior streams and the presence of strandline deposits within dunal corridors.

TOPSAR will be crucial for determining local slope, reconstructing the drainage network and modelling flood estimation and extent, surfrace run-off and landform development.

4. CONCLUSIONS

The Australia deployment has provided a core group of Australian researchers an exciting opportunity to exploit the unique capabilities of both AIRSAR and TOPSAR datasets. The benefits of radar remote sensing technology to earth system sciences now depends on the regular availability of these precision datasets from operational spaceborne systems.

5. REFERENCES

Richards, J.A., B.C. Forster, A.K. Milne, J.C. Trinder, and G.R. Taylor, 1987, "Australian multi-experimental assessment of SIR-B (AMAS). Final Report to NASA and JPL, March 1987," pp. 11 plus appendices.

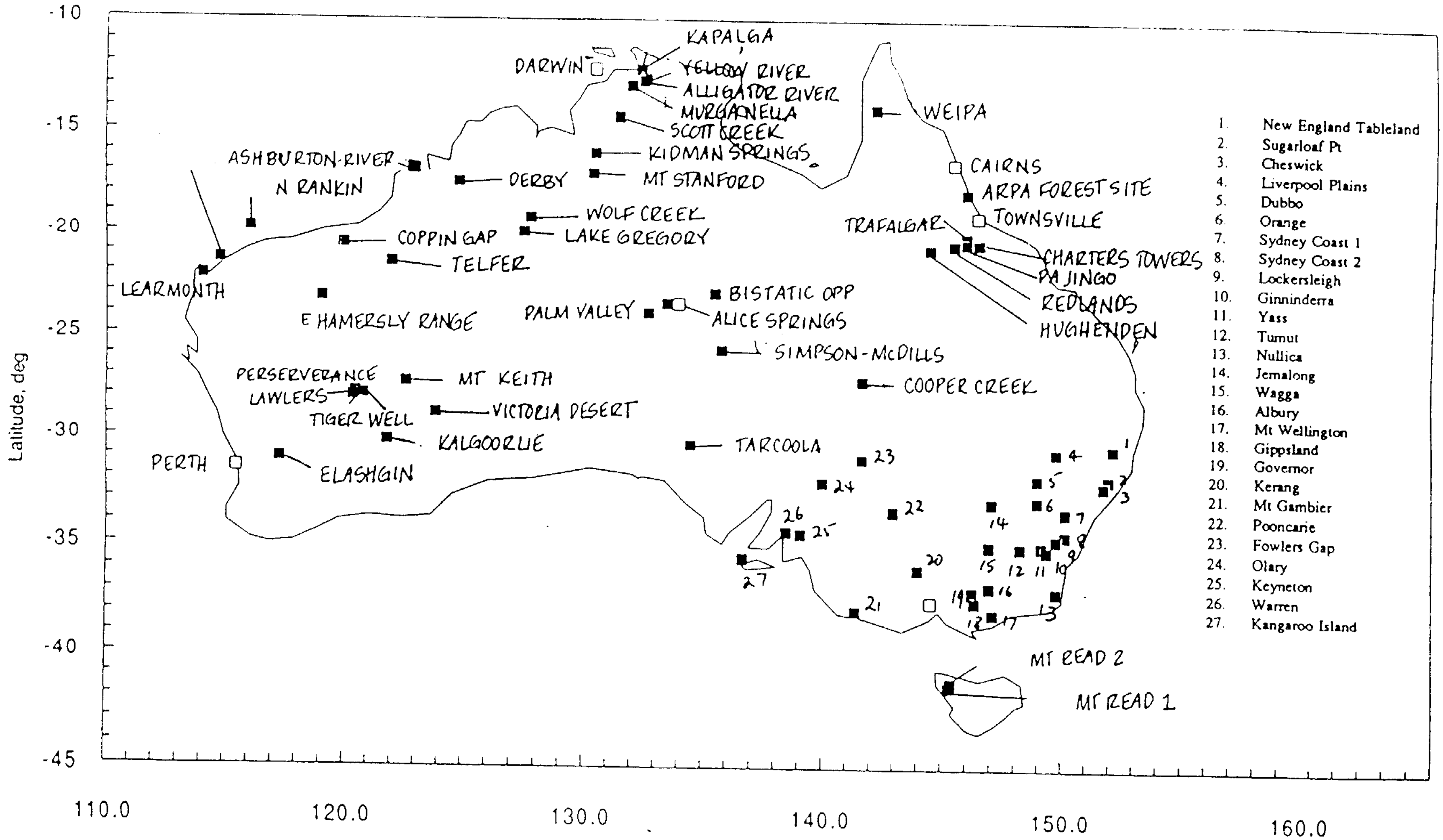

Figure 1. Location of AIRSAR Test Sites for the Australian Deployment, September 1993. Sites in South-eastern Australia.

Site names for South-eastern Australia are listed at the side.

N95- 23949

CURRENT AND FUTURE USE OF TOPSAR DIGITAL TOPOGRAPHIC DATA FOR VOLCANOLOGICAL RESEARCH

Peter J. Mouginis-Mark, Scott K. Rowland and Harold Garbeil

Planetary Geosciences
Department Geology and Geophysics, SOEST
University of Hawaii
Honolulu, Hawaii 96822

Introduction

In several investigations of volcanoes, high quality digital elevation models (DEMs) are required to study either the geometry of the volcano or to investigate temporal changes in relief due to eruptions. Examples include the analysis of volume changes of a volcanic dome (Fink et al., 1990), the prediction of flow paths for pyroclastic flows (Malin and Sheridan, 1982), and the quantitative investigation of the geometry of valleys carved by volcanic mudflows (Rodolfo and Arguden, 1991). Additionally, to provide input data for models of lava flow emplacement, accurate measurements are needed of the thickness of lava flows as a function of distance from the vent and local slope (Fink and Zimbelman, 1986). Visualization of volcano morphology is also aided by the ability to view a DEM from oblique perspectives (Duffield et al., 1993).

Until recently, the generation of these DEMs has required either high resolution stereo air photographs or extensive field surveying using the Global Positioning System (GPS) and other field techniques. Through the use of data collected by the NASA/JPL TOPSAR system, it is now possible to remotely measure the topography of volcanoes using airborne radar interferometry (Zebker et al., 1992). TOPSAR data can be collected day or night under any weather conditions, thereby avoiding the problems associated with the derivation of DEMs from air photographs that may often contain clouds. Here we describe some of our initial work on volcanoes using TOPSAR data for Mt. Hekla (Iceland) and Vesuvius (Italy). We also outline various TOPSAR topographic studies of volcanoes in the Galapagos and Hawaii that will be conducted in the near future, describe how TOPSAR complements the volcanology investigations to be conducted with orbital radars (SIR-C/X-SAR, JERS-1 and ERS-1), and place these studies into the broader context of NASA's Global Change Program.

TOPSAR

The TOPSAR instrument is a C-band (5.6 cm wavelength) radar flown on board a NASA DC-8 aircraft (Zebker et al., 1992; Evans et al., 1992). Topographic data collected by TOPSAR have a spatial resolution of 5 to 10 m, with a vertical accuracy of 1 to 5 m depending upon the relief of the target — smoother surfaces (i.e., at the pixel-scale, those surfaces that have a uniform relief) will have lower height errors than mountainous areas because of the greater uncertainty in characterizing an inhomogeneous pixel with a single height value. TOPSAR swaths are 30 km x 6.4 km in size. These topographic data are acquired concurrently with radar backscatter images at C-band, L-band (24 cm) and P-band (68 cm), which enable surface textures and structure to be investigated in a manner comparable to conventional radar analyses of volcanoes (e.g., Gaddis et al., 1989, 1990; Campbell et al., 1989).

TOPSAR measurements differ significantly from DEMs derived from the interpolation of digitized contour maps. In TOPSAR data sets, a height measurement is made at each pixel and therefore the TOPSAR DEM provides a truer representation of the surface relief. We note, however, that in its current configuration TOPSAR does not have any absolute geodetic control, so that each TOPSAR scene must be referenced to a geodetic grid before absolute elevations and regional slopes (i.e., those slopes measured along or across the entire swath) can be resolved.

Mt. Hekla and Vesuvius

We illustrate the use of TOPSAR data for volcanological research with examples derived from data collected over Mt. Hekla (Iceland) and Vesuvius (Italy) in the summer of 1991.

For Hekla volcano, the thickness of lava flows can be measured from TOPSAR data (Fig. 1), and these thickness measurements can be used with existing numerical models of lava rheology to infer yield strengths of 5000 to 30,000 Pa. (Rowland et al., 1992), comparable to lavas of similar composition (basaltic andesite) elsewhere. In all cases, the calculated yield strength of a flow increases with distance from the vent (reflecting the greater amount of cooling of the furthest-traveled lava), although average flow thickness remains fairly constant. TOPSAR data also permit the geometry of a moberg ridge (which is a volcanic feature formed by a subglacial eruption) to be determined (Fig. 2). Although only a few examples of moberg ridges around Hekla were imaged by TOPSAR, it would be possible to use TOPSAR to measure the volume of many ridges, thereby enabling the amount of lava erupted from different vents to be determined (Evans et al., 1992).

TOPSAR data for Vesuvius, Italy, permit the geometry of the volcano flanks to be determined (Mouginis-Mark and Garbeil, 1993). There is a large number of valleys on the flanks of the older portion (Mt. Somma) of Vesuvius. These valleys are primarily water-carved in origin, but they have also been used as pathways for pyroclastic flows. TOPSAR enables a slope map of the flanks to be derived, and valley geometry to be measured. Slope maps can provide valuable input when examining the likelihood that different areas will be affected by volcanic hazards such as pyroclastic flows, lava flows, and lahars. We have found the slopes of the flanks of Mt. Somma to be typically ~13 - 24° at lower elevations, ~25 - 36° closer to the rim, with a maximum value of > 48° on the inner walls of the craters.

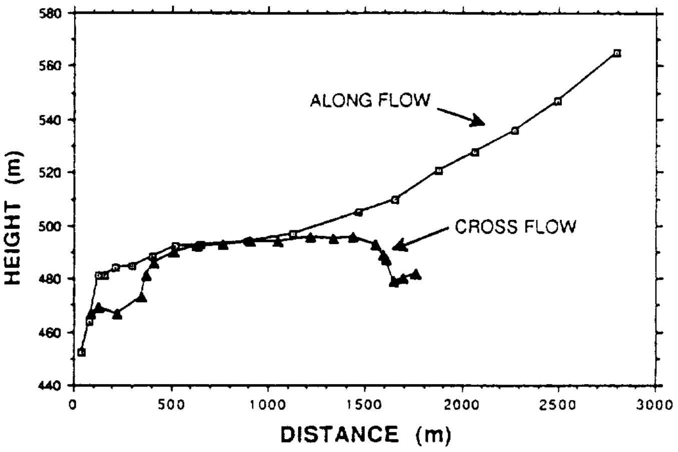

Fig. 1: TOPSAR profiles across and along a single lava flow erupted from Mt. Hekla, Iceland.

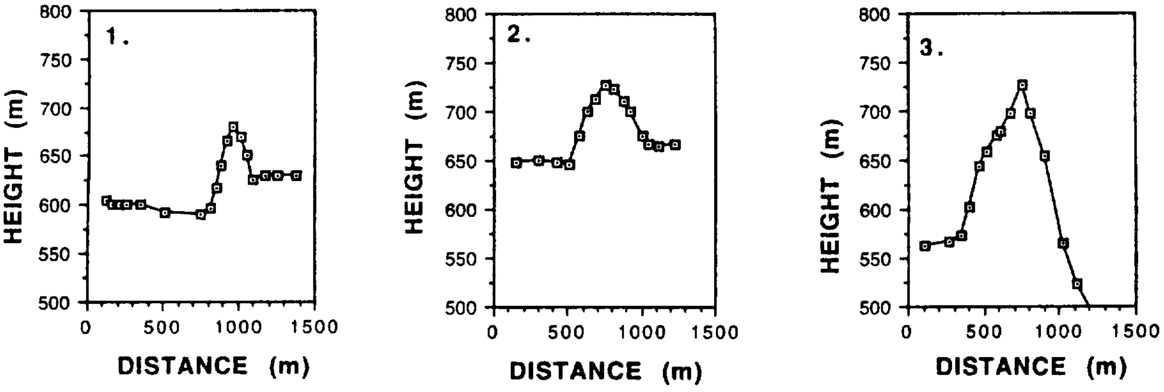

Fig. 2: 3 profiles across a single moberg ridge close to Mt. Hekla, Iceland, derived from TOPSAR data. Length of moberg ridge perpendicular to these profiles is ~3800 m.

Profiles down the length of individuals valleys (Fig. 3a) can also be determined. Potentially, it may be possible to use TOPSAR data to recognize different lithologic units (either different in the mechanical properties or absolute age) by this method, since the degree of erosion of materials on a given slope should vary as a function of strength and/or age. In order to explore the physical basis for these relationships, a more rigorous study would be required to identify and evaluate the possible significant variables (e.g., Knighton, 1974). The profiles across a valley at different distances from the rim of Mt. Somma (Fig. 3b) also show that the geometry of the valley varies from one place to another. From our morphologic data, there appears to be a trend towards proportionally deeper valleys with increasing slope. In general, for each valley, on slopes > 30° depth can be twice that on slopes < 10°. This may be interpreted to be an indication of the lower erosive action of the flows (either debris flows or running water) on the lower slopes than on steep slopes, or of deposition on the lower slopes.

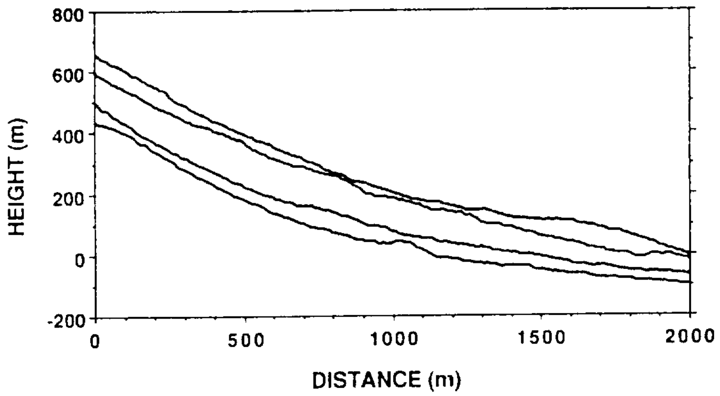

Fig. 3a (Left, at top): Profiles for individual valleys on the flanks of Mt. Somma. Fig. 3b (left, at bottom) Cross-sections through a single valley on flanks of Mt. Somma, as determined from TOPSAR data. Only a few representative cross-sections are shown, but the original data were obtained at every 250 m down the flanks.

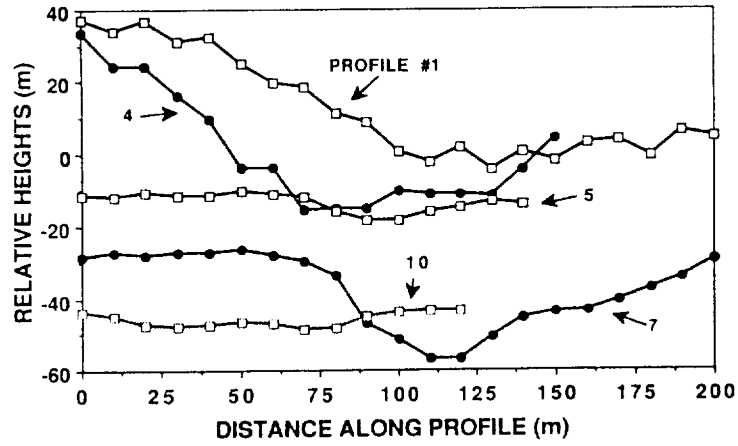

Future TOPSAR data sets

To date, only a few TOPSAR data sets have been collected over volcanoes; the most useful are the data for the western Galapagos Islands. These volcanoes constitute one of the Space Shuttle Radar (SIR-C/X-SAR) "Super-Sites", and are also one of the targets for the JERS-1 Verification Program. Use of the TOPSAR DEM, as well as the AIRSAR multi-wavelength backscatter images and the JERS-1 SAR data, will therefore aid in the analysis of these orbital data sets.

Several structural and volcanological investigations of the Galapagos volcanoes have been conducted using air photographs (Chadwick and Howard, 1991) and satellite images (Munro and Mouginis-Mark, 1990; Rowland and Munro, 1992), but the detailed topography of the islands is poorly known. Fernandina and Isabela Islands were imaged in May 1993 by TOPSAR, but at the time of writing the analysis of these data has not been initiated. The use of TOPSAR data to investigate the spatial distribution of rift zones through the generation of slope maps, the measurement of lava flow thickness on different slopes, and the calculation of volumes of cinder cones and summit calderas, should all significantly improve our knowledge of these infrequently visited volcanoes.

Two TOPSAR deployments over Kilauea Volcano, Hawaii, are planned for September and October 1993. These flights will enable the derivation of a "topographic difference map", which should permit the quantitative measurement of the volume of new lava erupted during the intervening month. This will allow an average effusion rate for the volcano to be determined, as well as facilitate the study of the growth of a compound lava flow field. Finally, as part of the Decades Volcano program (Bennett et al., 1992), planning is under way for a TOPSAR deployment to Santa Maria Volcano, Guatemala, as well as the collection of ERS-1 orbital SAR data from the temporary ground receiving station in Atlanta, USA. Some time in the future we hope to use TOPSAR to aid the analysis of the Santiaguito lava dome, and help with the production of new hazard maps through the construction of detailed topographic maps.

Acknowledgments

This research was supported by NASA grants NAGW-1162 and NAGW-2468 from NASA's Office of Mission to Planet Earth.

References

Bennett EHS, Rose WI, Conway FM (1992) Santa Maria, Guatemala: A Decade Volcano. Eos 73: 521 - 522

Campbell BA, Zisk SH, Mouginis-Mark PJ (1989) A quad-pol radar scattering model for use in remote sensing of lava flow morphology. Remote Sens Environ 30: 227 - 237

Chadwick WW, Howard KA (1991) The pattern of circumferential and radial eruptive fissures on the volcanoes of Fernandina and Isabela islands, Galapagos. Bull Volcanol 53: 257 - 275

Duffield W, Heiken G, Foley D, McEwen A (1993) Oblique synoptic images, produced from digital data, display strong evidence of a "new" caldera in SW Guatemala. J Volcanol Geotherm Res 55: 217 - 224.

Evans DL, Farr TG, Zebker HA, van Zyl JJ, Mouginis-Mark PJ (1992) Radar interferometric studies of the Earth's topography. Eos 73: 553 and 557 - 558

Fink JH, Malin MC, Anderson SW (1990) Intrusive and extrusive growth of the Mt. St. Helens lava dome. Nature 348: 435 - 437

Fink JH, Zimbelman JR (1986) Rheology of the 1983 Royal Gardens basalt flows, Kilauea Volcano, Hawaii. Bull Volcanol 48: 87 - 96

Gaddis L, Mouginis-Mark P, Singer R, Kaupp V (1989) Geologic analyses of Shuttle Imaging Radar (SIR-B) data of Kilauea Volcano, Hawaii. Geol Soc Amer Bull 101: 317 - 332

Gaddis LR, Mouginis-Mark PJ, Hayashi JN (1990) Lava flow surface textures: SIR-B radar image texture, field observations, and terrain measurements. Photogram Eng Remote Sensing 56: 211 - 224

Knighton AD (1974) Variation in width-discharge relation and some implications for hydraulic geometry Geol Soc Amer Bull 85: 1069 - 1076

Malin MC, Sheridan MF (1982) Computer-assisted mapping of pyroclastic flows. Science 217: 637 - 640

Mouginis-Mark, PJ and Garbeil, H. (1993) Digital topography of volcanoes from radar interferometry: An example from Mt. Vesuvius, Italy. Submitted to Bulletin Volcanology.

Munro DC, Mouginis-Mark PJ (1990) Eruptive patterns and structure of Isla Fernandina, Galapagos Islands from SPOT-1 HRV and Large Format Camera images. Int J Remote Sensing 11: 15011 - 1174

Rodolfo KS, Arguden AT (1991) Rain-lahar generation and sediment-delivery systems at Mayon Volcano, Philippines. In: Sedimentation in Volcanic Settings, SEPM Sp. Pub. No. 45: 71 - 87

Rowland SK, Munro DC (1992) The caldera of Volcan Fernandina: a remote sensing study of its structure and recent activity. Bull Volcanol 55: 97 - 109

Rowland, SK, Garbeil, H. and Mouginis-Mark, PJ (1992). Yield strengths of recent Hekla lavas. Fall 1992 AGU Abstracts, p. 648.

Zebker HA, Madsen SN, Martin J, Wheeler KB, Miller T, Lou Y, Alberti G, Vetrella S, Cucci A (1992) The TOPSAR interferometric radar topographic mapping instrument. IEEE Trans Geosci Rem Sen 30: 933 - 940.

N95- 23950

PRELIMINARY ANALYSIS OF THE SENSITIVITY OF AIRSAR IMAGES TO SOIL MOISTURE VARIATIONS

Rajan Pardipuram, William L. Teng
Hughes STX Corporation, Lanham, MD 20706

James R. Wang, Edwin T. Engman
NASA, Goddard Space Flight Center,
Greenbelt, MD 20771

Introduction

Synthetic Aperture Radar (SAR) images acquired from various sources such as Shuttle Imaging Radar B (SIR-B) and airborne SAR (AIRSAR) have been analyzed for signatures of soil moisture (Dobson et al., 1986, Wang et al., 1986, Rao et al., 1992). The SIR-B measurements have shown a strong correlation between measurements of surface soil moisture (0-5 cm) and the radar backscattering coefficient σ^0, (Wang et al., 1986). The AIRSAR measurements, however, indicated a lower sensitivity (Rao et al., 1992). In this study, an attempt has been made to investigate the causes for this reduced sensitivity.

Measurements

Polarimetric AIRSAR data were acquired over the Little Washita watershed near Chickasha, Oklahoma during June 10-18, 1992. A total of 8 days of flights were made during this period. There was a series of heavy rainfall prior to June 10. No rainfall was reported between June 10 and 18. Soil moisture samples in the top 5 cm layer were collected at a number of fields during the time of the flights. The average soil moisture was ~0.26 gm/cm^3 on the first day of flight (June 10) and ~0.13 gm/cm^3 on the last day of flight (June 18).

Two areas covered by the AIRSAR flights were selected for the study, one southwest of the watershed (site 1), and the other northeast of the watershed (site 2). Three sets of images (C, L, and P-bands) for the two areas, acquired on three different dates, June 10, 14, and 18, were analyzed. In order to obtain a broader perspective on the sensitivity of the SAR images to soil moisture variations, a finite strip of 200 pixels in the cross track and 1024 pixels in the along track directions were chosen from each image. The strips from each scene were chosen such that they cover approximately the same area on the ground.

Results

The results from the analysis for site 1 are shown in Figures 1 and 2. Each data point in these figures represents an average of 200 pixels in the cross track and 8 pixels in the along track directions. Averaging was performed to reduce the effect of speckle and noise.

Figures 1 and 2 indicate the variations of σ_{hh}^{o}, at all three frequencies, for the June 10 and 18 images. These figures show that (1) the average value of σ_{hh}^{o} changed only by about 1 dB, 2.5 dB, and 3 dB, for C, L, and P-bands, respectively from June 10 to 18, whereas soil moisture changed by ~0.13 gm/cm^3 during the same period; and (2) amplitude variations within the strips are much higher in comparison (on the order of 5-8 dB). Since soil moisture is not expected to differ by a significant amount within a strip, the wide amplitude fluctuations indicate that the radar backscatter of the AIRSAR images is sensitive to other surface features. The general pattern of the amplitude variations of σ_{hh}^{o} is the same for both the June 10 and 18 images, which suggests that these variations are caused by surface features which did not change from June 10 to 18. However, at this point, it is not clear which surface feature/features are causing these variations. Comparison of responses of the three frequencies shows that P-band has the highest variation (standard deviation of ~ 2.2) and C-band the lowest (standard deviation of ~ 0.6).

Images of site 2 were also analyzed to determine if they indicate similar trends. However, a disturbing feature was observed in the C-band images. Figures 3 and 4 indicate the variations of σ^{o} values for C-band, for June 10 and 18, respectively. These figures show that, while σ_{hh}^{o} is higher than σ_{vv}^{o} on June 10, σ_{vv}^{o} is higher than σ_{hh}^{o} on June 18. This pattern was not noticed in the case of L and P-bands. This feature is probably caused by an error in the calibration procedure; therefore, these images were not used for the analysis.

Conclusions

An attempt was made to examine the causes for the lower sensitivity of AIRSAR images to soil moisture variations in comparison with that of SIR-B images. Based on the results obtained, it can be inferred that σ^{o} values are less sensitive to soil moisture than to other surface features. Further analysis of these images is required to identify those surface features which predominate the radar backscatter in the case of AIRSAR.

Some of the C-band images indicated a change in the dominant polarization with time. This change is not expected to occur over a typical agricultural area and could be due to a potential problem in the calibration.

References

Dobson, M. C. and F. T. Ulaby, "Preliminary Evaluation of the SIR-B Response to Soil Moisture, Surface Roughness, and Crop Canopy Cover," IEEE Trans. Geosci. and Remote Sensing, GE-24(4), pp. 517-526, 1986.

Rao, K. S., W. L. Teng, and J. R. Wang, "Terrain Effects on Backscattering Coefficients Derived from Multifrequency Polarimetric SAR Data," IGARSS'92, vol. 1, pp 86-88, Houston, Texas, 1992.

Wang, J. R., E. T. Engman, J. C. Shiue, M. Rusek and C. Steinmeier, "The SIR-B Observations of Microwave Backscatter Dependence on Soil Moisture, Surface Roughness, and Vegetation Covers," IEEE Trans. Geosci. and Remote Sensing, GE-24(4), pp. 510-516, 1986.

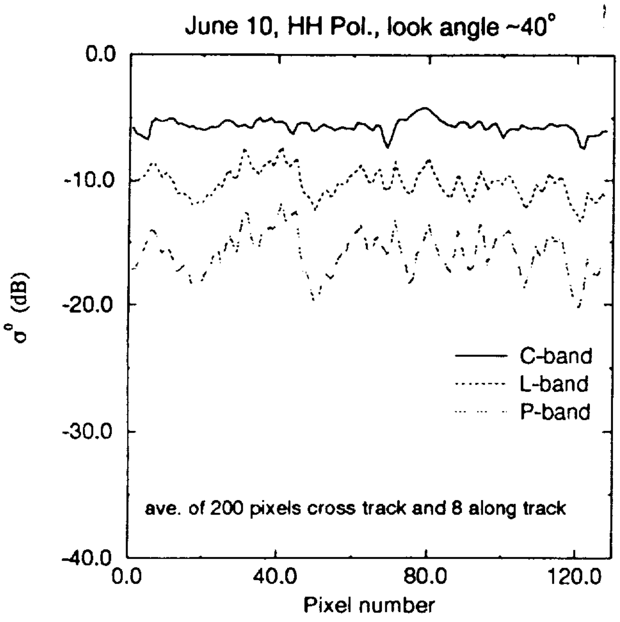

Figure 1. The along track variation of σ_{HH}^{o} at the look angle of 40°, for C, L, and P-bands (June 10, 1992).

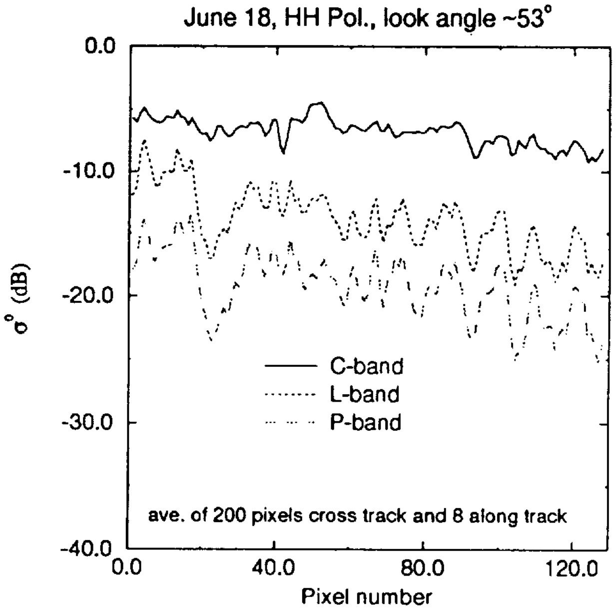

Figure 2. The along track variation of σ_{HH}^{o} at the look angle of 53°, for C, L, and P-bands (June 18, 1992).

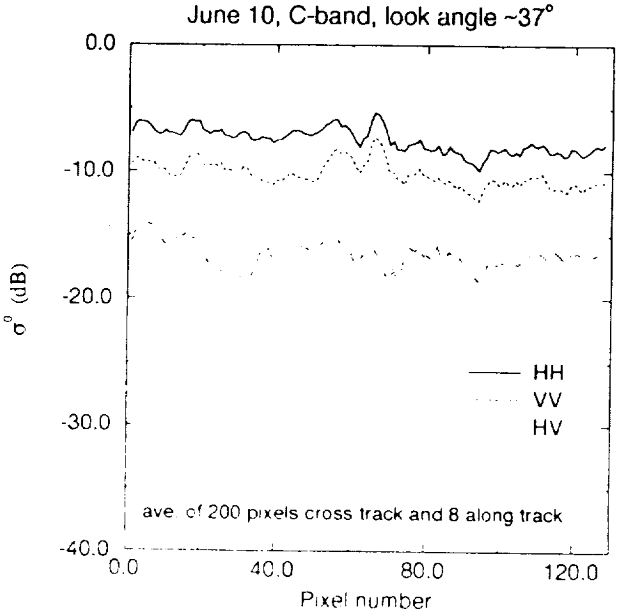

Figure 3. The along track variation of C-band σ^{o} values, at the look angle of 37°, for HH, VV, and HV polarizations (June 10, 1992).

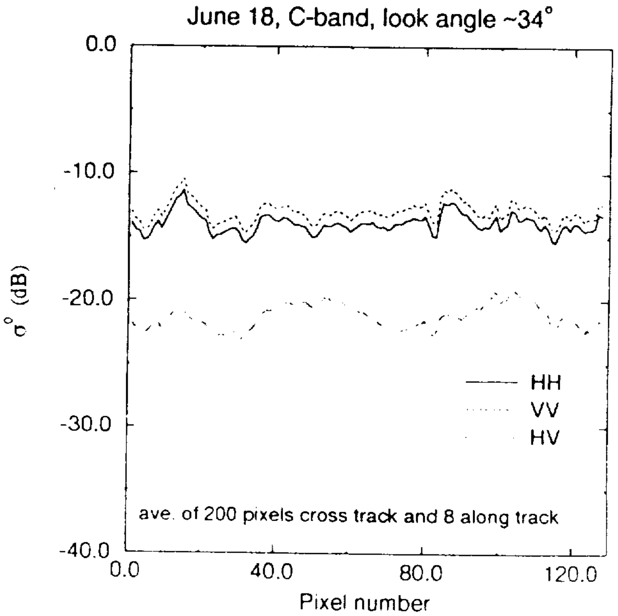

Figure 4. The along track variation of C-band σ^{o} values at the look angle of 34°, for HH, VV, and HV polarizations (June 18, 1992).

UNUSUAL RADAR ECHOES FROM THE GREENLAND ICE SHEET

E. J. Rignot, J. J. van Zyl, S. J. Ostro, and K. C. Jezek†

Jet Propulsion Laboratory, California Institute of Technology, Pasadena, CA 91109

†Byrd Polar Research Center, Ohio State University, Columbus, OH 43210

1. INTRODUCTION

In June 1991, the NASA/Jet Propulsion Laboratory airborne synthetic-aperture radar (AIRSAR) instrument collected the first calibrated data set of multifrequency, polarimetric, radar observations of the Greenland ice sheet (Rignot et al., 1993). At the time of the AIRSAR overflight, ground teams recorded the snow and firn (old snow) stratigraphy, grain size, density, and temperature (Jezek and Gogineni, 1992) at ice camps in three of the four snow zones identified by glaciologists to characterize four different degrees of summer melting of the Greenland ice sheet (Benson, 1962). The four snow zones are: 1) the dry-snow zone, at high elevation, where melting rarely occurs; 2) the percolation zone, where summer melting generates water that percolates down through the cold, porous, dry snow and then refreezes in place to form massive layers and pipes of solid ice; 3) the soaked-snow zone where melting saturates the snow with liquid water and forms standing lakes; and 4) the ablation zone, at the lowest elevations, where melting is vigorous enough to remove the seasonal snow cover and ablate the glacier ice. There is interest in mapping the spatial extent and temporal variability of these different snow zones repeatedly by using remote sensing techniques. The objectives of the 1991 experiment were to study changes in radar scattering properties across the different melting zones of the Greenland ice sheet, and relate the radar properties of the ice sheet to the snow and firn physical properties via relevant scattering mechanisms. Here, we present an analysis of the unusual radar echoes measured from the percolation zone.

2. EXPERIMENTAL RESULTS

Figure 1 shows average values of the radar reflectivity σ^0_{RL} (i.e., receiving right-circular polarized signals and transmitting left-circular polarized signals) obtained by averaging the radar measurements recorded by AIRSAR at the Crawford Point site in the percolation zone along the flight path as a function of the incidence angle of the radar illumination θ. At 5.6 and 24 cm, σ^0_{RL} is higher than unity at 18°, and decreases toward higher incidence angles. At 68 cm, σ^0_{RL} is ten times lower, and shows kilometer-scale spatial variations. Figure 1 also shows the circular polarization ratio, $\mu_C = \sigma^0_{RR}/\sigma^0_{RL}$, and the linear polarization ratio $\mu_L = \sigma^0_{HV}/\sigma^0_{HH}$ obtained at the Crawford Point site. These ratios of echo power in orthogonal senses are defined to be equal to zero for specular backreflection from a perfectly smooth dielectric surface. μ_C is larger than unity at 5.6 and 24 cm for incidence angles larger than 30° and 45°, respectively, increasing to 1.6 and 1.4 at 66°. At 68 cm, μ_C is everywhere less than 0.8 and drops as low as 0.1 in some places, with kilometer-scale spatial variations negatively correlated with those observed in the radar reflectivity images. μ_L is as large as 0.46 at 5.6 cm and 0.22 at 24 cm, but remains less than 0.1 at 68 cm.

In the AIRSAR scenes of the Swiss camp and the GISP II sites, at all three wavelengths, σ^0_{RL} are 10 to 30 times lower than at Crawford Point; μ_C is less than 0.4, and μ_L is less than 0.1. To the best of our knowledge, no natural terrestrial surface other than the Greenland percolation zone shows strong echoes with $\mu_C > 1$ and $\mu_L > 0.3$ (see Figure 1 caption). However, strong echoes with large values of μ_C and μ_L have been reported for the icy Galilean satellites since the

1970's (Ostro et al., 1992). More recently, radar observations of the Mars residual south polar ice cap (Muhleman et al., 1991), portions of Titan (Muhleman et al., 1990), and polar caps on Mercury (Slade et al., 1992) have revealed that surfaces with high radar reflectivity and $\mu_C > 1$ exist elsewhere in the solar system. Figure 1 shows that the mean values of disk-integrated radar reflectivities σ^0_{OC} and circular and linear polarization ratios μ_C and μ_L for Europa, Ganymede, and Callisto at 3.5 and 13 cm resemble those of the percolation zone at 5.6 and 24 cm, and dwarf the values reported for other terrestrial surfaces. Yet, Greenland's average values at 24 cm are several tens of a percent lower than at 5.6 cm, and $\mu_C < 1$ at 68 cm, indicating a change in the scattering process at the longer wavelengths, whereas 70-cm estimates of μ_C for the icy satellites apparently exceed unity (Campbell et al., unpublished data). Also, μ_C for the percolation zone decreases significantly from 66^o to 18^o, whereas no such difference has been noticed for the icy satellites (Ostro et al., 1992); and σ^0_{RL} is a much stronger function of the incidence angle than in the case of the icy satellites (Ostro et al., 1992).

3. INTERPRETATION

Zwally (1977) suggested that ice inclusions could explain low emissivities measured for the percolation zone by spaceborne microwave radiometers. Since then, surface-based radio sounding experiments, and airborne active and passive microwave measurements (Swift et al., 1985), have supported the hypothesis that volume scattering from subsurface ice layers and ice pipes is the major influence on the radar returns. Recent surface-based radar observations conducted at Crawford Point (Jezek and Gogineni, 1992) at 5.4 and 2.2 cm provided clear evidence that, at incidence angles between 10^o and 70^o, most of the scattering takes place in the most recent annual layer of buried ice bodies. Studies of the snow stratigraphy at Crawford Point at the time of the radar flight indicate that the ice inclusions from the previous summer melt were at 1.8 m below the surface. Ice layers and ice lenses, a millimeter to a few centimeters thick, extend at least several tens of centimeters across, parallel to the firn strata. Ice pipes, several centimeters thick and several tens of centimeters long, are vertically extended masses reminiscent of the percolation channels that conduct meltwater down through the snow during summer, feeding ice layers. The fact that radar returns measured at 68 cm are significantly weaker and have lower polarization ratios than those at 5.6 and 24 cm suggests that the discrete scatterers responsible for the radar echoes are of typical dimension less than a few tens of centimeters, similar to the scales of the solid-ice inclusions. The 68-cm echoes probably are dominated by single reflections from deeply buried layers of denser firn or concentrated ice bodies, whereas the 5.6- and 24-cm echoes probably are dominated by multiple scattering from the ice layers and pipes in the most recent annual layer. The relatively sharp decrease in μ_C and μ_L for θ less than 40^o perhaps reveals the presence of a strong, specular reflection from the ice layers at small incidence angles, which is also suggested by the strong dependence of radar reflectivity on incidence angle. Ice layers and pipes also form in the soaked zone, but the snow there is so saturated with liquid water that the radar signals are strongly attenuated, cannot interact with the buried ice formations, and hence yield echoes with low reflectivities and polarization ratios. In the dry-snow zone, the snow is dry, cold, porous, clean, and therefore very transparent at microwave frequencies, but does not contain solid-ice scatterers that could interact with the radar signals.

For the satellites, no in-situ measurements exist, but theoretical interpretations favor subsurface coherent volume scattering as the source of the radar signatures (Hapke, 1990), a phenomenon also known as weak localization (see van Albada et al., 1990 for a review). Coherent backscattering can theoretically produce strong echoes with $\mu_C > 1$ (the helicity of the incident polarization is preserved through multiple forward scattering) and $\mu_L \approx 0.5$, provided that (i) the scattering heterogeneities are comparable to or larger than the wavelength (Peters, 1992), and (ii) the relative refractive index of the discrete, wavelength-sized scatterers is smaller than 1.6 (Mishchenko, 1992). As noted by Ostro and Shoemaker (1990), prolonged impact cratering of the satellites probably has led to the development of regoliths similar in structure and particle-size distribution to the lunar regolith, but the high radar transparency of ice compared with that of silicates permits longer photon path lengths, and higher-order scattering. Hence coherent backscatter can dominate the echoes from Europa, Ganymede, and Callisto, but contributes negligibly to lunar echoes. Similarly, the upper few meters of the Greenland percolation zone are relatively transparent (unlike the soaked zone) and, unlike the dry-snow zone, contain an abundance of solid-ice scatterers at least as large as the radar wavelength, with a relative refractive index of about 1.3, so coherent backscatter also can dominate the echoes there. However, the detailed subsurface configurations of the satellite regoliths, where heterogeneities are the product of meteoroid bombardment, are unlikely to resemble that within the Greenland percolation zone, where heterogeneities are the product of seasonal melting and freezing.

Acknowledgements: We thank Dr. R. Thomas, Head of the Polar Research Program at NASA Headquarters, for supporting this research. Part of this work was carried out at the Jet Propulsion Laboratory, California Institute of Technology, under contract with the National Aeronautics and Space Administration.

REFERENCES

C. S. Benson, US Army Snow Ice Permafrost Res. Estab. Res. Rep. 70 (Hanover, NH, 1962).
K. C. Jezek and S. P. Gogineni, *IEEE Geosc. Rem. Sens. Soc. Newsletter* **85**, 6 (1992).
B. Hapke, *Icarus* **88**, 407 (1990).
M. I. Mishchenko, *Earth, Moon, and Planets* **58**, 127 (1992).
D. O. Muhleman, B. J. Butler, A. W. Grossman, and M. A. Slade, *Science* **253**, 1508 (1991).
D. O. Muhleman, A. W. Grossman, B. J. Butler, and M. A. Slade, *Science* **248**, 975 (1990).
S. J. Ostro *et al.*, *J. Geophys. Res.* **97**, 18277 (1992).
S. J. Ostro and E. M. Shoemaker, *Icarus* **85**, 335 (1990).
K. J. Peters, *Phys. Rev.* B **46**, 801 (1992).
E. Rignot, S. Ostro, J. van Zyl, and K. Jezek, *Science* **261**, 1710 (1993).
M. A. Slade, B. J. Butler, and D. O. Muhleman, *Science* **258**, 635 (1992).
C. T. Swift, P. S. Hays, J. S. Herd, W. L. Jones, and V. E. Delmore, *J. Geophys. Res.* **90**, 1983 (1985).
M. P. van Albada, M. B. van der Mark and A. Lagendijk, in *Scattering and Localization of Classical Waves in Random Media*, P. Sheng, Ed. (World Scientific, Singapore, 1990), p. 97.
H. J. Zwally, *J. Glaciol.* **18**, 195 (1977).

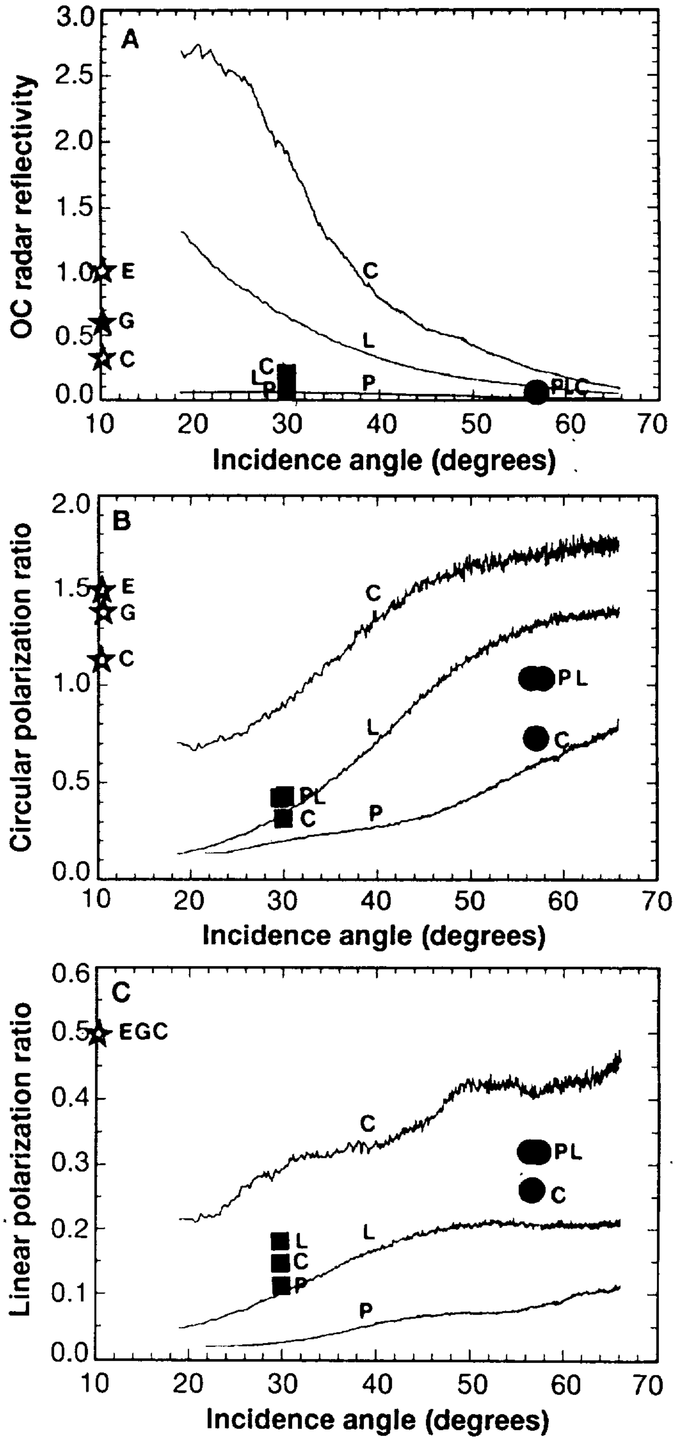

Figure 1. Average values of the (A) OC radar reflectivity σ^0_{RL}, (B) circular polarization ratio $\mu_C = \sigma^0_{RR}/\sigma^0_{RL}$, and (C) linear polarization ratio $\mu_L = \sigma^0_{HV}/\sigma^0_{HH}$ for the Greenland percolation zone obtained by averaging the radar measurements recorded by AIRSAR at Crawford Point along the flight path, at 5.6 (C-), 24 (L-), and 68 cm wavelength (P-), as a function of the incidence angle of the radar illumination. Radar backscatter values and polarization ratios measured from wavelength-sized roughness on a surface of lava (black squares) (J. J. van Zyl, C. F. Burnette, and T. G. Farr, *Geophys. Res. Lett.* **18**, 1787 (1991)) and from tropical rain forest (black dots) (A. Freeman, S. Durden, and R. Zimmerman, Proc. of the Int. Geos. Rem. Sens. Symp., Houston, Texas, May 26-29, IEEE New York Pub., 1686 (1992)) are also shown in the Figure. The values indicated for the icy satellites Europa (E), Ganymede (G), and Callisto (C) are disk-integrated average measurements at 3.5 and 13 cm wavelengths (Ostro et al., 1992).

N95- 23952

MAC EUROPE '91 CAMPAIGN: AIRSAR/AVIRIS DATA INTEGRATION FOR AGRICULTURAL TEST SITE CLASSIFICATION

S Sangiovanni*, M. F. Buongiorno**, M. Ferrarini*** and A. Fiumara*

*Earth Observation Division, Telespazio SpA
Via Tiburtina 965, Rome - Italy

**formerly at Telespazio SpA, Via Tiburtina 965, Rome - Italy
now at Istituto Nazionale di Geofisica, Via di Vigna Murata 605, Rome - Italy

***Electronic Engineering Dpt. - Università "La Sapienza"
Via Eudossiana 18, Rome - Italy

1. INTRODUCTION

During summer 1991, multi-sensor data were acquired over the Italian test site "Oltrepò Pavese", an agricultural flat area in Northern Italy. This area has been the Telespazio pilot test site for experimental activities related to agriculture applications.

The aim of the investigation described in the following paper is to assess the amount of information contained in the AIRSAR and AVIRIS data, and to evaluate classification results obtained from each sensor data separately and from the combined dataset. All classifications are examined by means of the resulting confusion matrices and Khat coefficients (Congalton et al., 1983). Improvements of the classification results obtained by using the integrated dataset are finally evaluated.

2. DATA SET DESCRIPTION

AIRSAR data were acquired with flight Nr. 91-118 on June 22nd. Four tracks of the area were available. We used the 45-1 track because it was the closest to the area of the ground truth acquisition. Among the three available bands, P band was not used because it was highly disturbed by an interference noise pattern.

AVIRIS data were acquired with flight 910719b on July 19th.

In order to obtain information about the **ground truth**, two "in situ" campaigns were performed. Due to slight errors in the flight tracks, the images do not exactly match the field survey area: in fact, about 45% only of the SAR images are covered by ground truth and this percentage decreases to about 20% in the AVIRIS images.

3. SAR DATA ANALYSIS

3.1. "Per Field" Classification

The discriminant analysis was performed on every combination of the 6 power "bands" (2 frequencies and 3 polarizations); the conclusions can be summarized: **1)** Khat values range from 0.555 to 0.815 as the number of features per observation is increased; the optimized choice is the L-VV, C-HH, C-HV combination, which allows a good classification accuracy (Khat value is 0.805) with a reasonably small amount of data. **2)** Although the results are quite good, problems still arise in the discrimination of alfalfa and corn from wheat. These problems were not solved even by adding more "bands". **3)** The Khat values obtained are quite optimistic since the same data set was used both for training and testing.

3.2 "Per Pixel" Classification

In this case we used all features available for the AIRSAR (that is 6 bands in the NML classifications and 18 for the polarimetric algorithms).

By the examination of the Table 1, we can draw the following conclusions: 1) the classifiers specifically designed for polarimetric data (Lee et al., 1992; Kong et al., 1987) do not seem to improve the classification accuracy. This could mean that phase information is not vital: in fact, the classification accuracies obtained with the NML classifier are very close to polarimetric ones, but the first uses less information (only the power features). 2) Speckle filtering is very useful to improve the classification accuracy as denoted by the 9% gain in the Khat values [(the speckle reduction filters that have been implemented are adaptive filters (Lee et al., 1991; Frost et al., 1981)].

4. AVIRIS DATA ANALYSIS

4.1. Data Reduction

From the original 224 AVIRIS bands, we selected 131 between 0.4 µm and 1.75 µm. The radiance to reflectance reduction was performed by means of the "flat field" technique (Crowley, 1990). For this work we identified a suitable flat field examining some sand deposits located near the Po river banks. Although this method is not very reliable, especially in the short wavelengths, it seems to be the best approach in order to retrieve the relative ground reflectance, since no information on local atmospheric parameters (such as aerosols, water vapor, etc.) were available.

We used the reflectance data obtained to draw spectral signatures of agricultural crops and other targets present in the area (an example is given in Figure 1). The analysis of the spectra shows a great agreement with experimental ones (Elvidge, 1990; Martin, 1990; Goetz, 1991).

The spectral analysis allowed us to select 14 significative bands that maximized the differences between crops in the reflectance spectra (see Figure 1). We obtained a further reduction by means of a Principal Components Analysis (Loughlin, 1991; Fung, 1987) performed on these bands; this analysis allowed us to define two combinations of components [PC2, PC3, PC6 (referred to as "refl") and PC1, PC2, PC3 (referred to as "ref2")]. The PC Analysis was also performed on the 14 radiance bands to investigate the effects of calibration on the classification accuracy.Other two combinations of components [PC3, PC4, PC5 ("rad1") and PC1, PC3, PC4 ("rad2")] were thus provided. In both cases, the selection was done by visual examination of the single PC images and by the analysis of the eigenvectors' matrix.

4.2. Data Classification

AVIRIS classifications were performed on the same classes as for SAR data and in a "per pixel" approach. The features used in the analyses are the PC combinations, both in reflectance and in radiance values, described above.

The Khat values obtained (see Table 2) are close to the ones given by the AIRSAR "per pixel" classifications and, though not expected, even the "unsupervised results" are very good. This could be explained as follows: 1) AVIRIS gives very specific information for each channel: this allows the classifier to recognize different objects without the need of a preliminary training. 2) In order to reduce the number of generated classes, the clustered image was post-processed by merging those clusters that seemed to belong to the same class.

5. DATA FUSION

5.1. Image Registration

We performed the following operations: 1) slant-to-ground range projection of the 6 AIRSAR power speckle-filtered images; 2) re-sampling of AIRSAR images to match the AVIRIS pixel spacing; 3) image-to-image registration with a cubic convolution filter.

Steps 1 and 2 were executed together with a new projection algorithm developed by Telespazio which allowed us to obtain less than 1 pixel in Mean Squared Error after co-registration.

5.2. Multi-Sensor Classification

For comparison purposes, we used the same classes as in the AVIRIS and AIRSAR "per pixel" classifications. The integrated classification was carried out on the six projected AIRSAR power images and the AVIRIS PC images. Fifteen combinations were classified using the NML and clustering algorithms

From the Table 3, it is evident that the multi-sensor integration gives good results: in fact, these values are generally and significantly higher than those achieved by AIRSAR and AVIRIS separate classifications. The extremely good accuracy obtained by the integrated data is also demonstrated by the absence of "critical pairs" in the best multi-sensor confusion matrix. This absence can be justified by noticing that each sensor data classification was not affected by the same "critical pairs", but in both cases it was very difficult to discriminate alfalfa from other crops (especially from wheat and corn).

6. CONCLUSIONS

In this work a multi-sensor analysis was carried out; first the separate data sets were processed and classified, then their integration and the consequent classification were performed.

The SAR data analysis showed (see Table 1) that polarimetric information does not seem to improve the classification accuracy: in fact, in spite of the great number of features available, the polarimetric classifiers show a little improvement with respect to the NML classifier performed on the power images only (speckle reduction techniques furtherly improve the classification results).

Among the L and C power information, the co-polarizations (HH, VV) seem to be useful for classes identification, while the HV polarization turned out to be useful in "critical pairs" discrimination. It also seems that crops classification is more accurate when using L band.

The great amount of AVIRIS data and its high spectral resolution, which are surely useful in the characterization of green vegetation, imply two major problems: a) reduction of the data, b) accurate atmospheric corrections. Many efforts are being devoted to implement simulation models that will allow us to obtain a more accurate atmospheric correction.

7. REFERENCES

Congalton, R.G., 1983, "Assessing Landsat classification accuracy using discrete multivariate analysis statistical techniques", *PE & RS* , vol. 49, n° 12, pp. 1671-1678

Crowley, S.K., 1990, "Techniques for AVIRIS data normalization in areas with partial vegetation cover", *JPL AVIRIS Workshop*, Pasadena (CA).

Elvidge, C.D., 1990, "Visible and infrared characteristics of dry plant materials", *Int. Journ. of Remote Sensing*, vol 12

Frost, V.S., J.A. Stiles, K.S. Shanmugan, J.C. Holtzman, S.A. Smith, 1981, "An adaptive filter for smoothing noisy radar images", *IEEE*, vol. 69, n° 1

Fung, T., L.E Drew, 1987, "Application of principal components analysis to change detection", *Photogrammetric Engineering and Remote Sensing*, vol 53, n° 12, December 1987, pp 1649-1658

Goetz, A.F.H., 1991, "Sedimentary facies analysis using AVIRIS data: a geophysical inverse problem", *JPL AVIRIS Workshop*, Pasadena (CA), May 20-21

Kong, J.A., H.A Yueh, A.A. Swartz, 1987, "Identification of terrain cover using the optimum polarimetric classifier", *Journ of E.M. Waves & Appl.*, vol 2, pp 171-194

Lee, J.S., M.R Grunes, S.A. Mango, 1991, "Speckle reduction in multipolarisation multifrequency SAR imagery", *IEEE GE 29*, pp. 535-544

Lee, J.S., M.R. Grunes, 1992, "Feature classification using multi-look polarimetric SAR imagery", *Proc. of IGARSS*, pp 77-79

Loughlin, W.P., 1991, "Principal component analysis for alteration mapping", *Proc. of ERIM "Eighth Thematic Conference on Geologic Remote Sensing"*, April 29 - May 2, 1991

Martin, M.E., J.D Aber, 1990, "Effects of moisture content and chemical composition on the near infrared spectra of forest foliage", *Proc. of SPIE,* vol 1298, Imaging Spectroscopy of Terrestrial Environment

Table 1. Khat values and 95% Confidence Intervals for AIRSAR "Per Pixel" Classifications

Classification	KHAT	Δ KHAT (%)
NML on LC bands	0.829	0.9
NML on LC Lee filtered	0.841	0.8
NML on LC Frost filtered	0.899	0.6
Lee's polarimetric	0.861	0.8
Kong's polarimetric	0.859	1.0

Table 2. Khat values and 95% Confidence Intervals for AVIRIS "Per Pixel" Classifications

Classification	KHAT	Δ KHAT (%)
NML on Rad1	0.8108	1.68
NML on Ref1	0.8261	1.62
NML on Rad2	0.8318	1.61
NML on Ref2	0.851	1.53
CLUSTER on Ref2	0.8408	1.61
CLUSTER on Rad2	0.841	1.58
CLUSTER on Ref2+Rad2	0.8509	1.56

Table 3. Khat values and 95% Confidence Intervals for Multi-Sensor "Per Pixel" Classifications

Classification	KHAT	Δ KHAT (%)
NML on Mix 1	0.8264	1.62
NML on Mix 2	0.881	1.39
NML on Mix 3	0.8892	1.34
NML on Mix 4	0.898	1.32
NML on Ref1+PC SAR	0.9284	1.10
NML on Ref2+PC SAR	0.9358	1.06
NML on Ref1+LC	0.9372	1.05
NML on Rad1+PC SAR	0.9403	1.02
NML on Rad2+PC SAR	0.9445	0.99
NML on Rad1+LC	0.9538	0.92
NML on Ref2+LC	0.9583	0.88
NML on Rad2+LC	0.9595	0.87
NML on Mix 5	0.9612	0.85
CLUSTER on Rad2+LC	0.821	1.67
CLUSTER on Ruf1+LC	0.9254	1.18

Table 4. Additional combinations referred as "Mix-Y" (Y= 1 to 5) in Table 3

Name	Features used
Mix-1	PC2-Reflect + C-HH + PC1-SAR
Mix-2	PC2-Reflect + PC3-Radiances + PC1-SAR
Mix-3	PC2-Reflect + PC3-Radiances + C-HH + PC1-SAR
Mix-4	PC2-Reflect + PC3-Radiances + C-HH + L-HH + PC1-SAR
Mix-5	PC2-Reflect + PC3-Radiances + C-HH + L-HH + C-HV + PC1-SAR

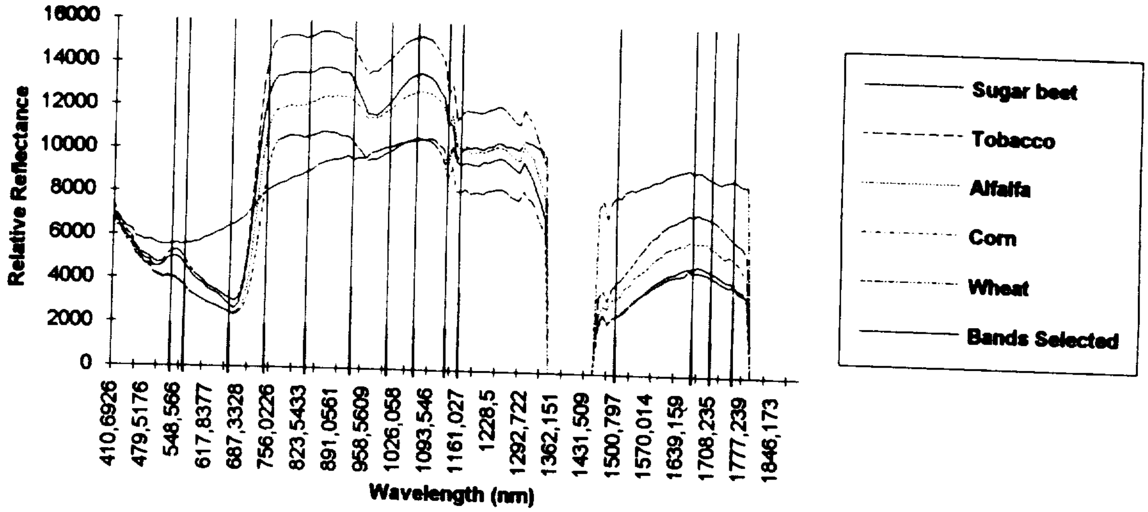

Figure 1. Typical crops spectral Signatures and bands selected for PCA

N95-23953

MEASUREMENT OF OCEAN WAVE SPECTRA USING POLARIMETRIC AIRSAR DATA

D.L. Schuler
Remote Sensing Division
Naval Research Laboratory
Washington, DC 20375-5351

1.0 BACKGROUND

Azimuthally traveling waves are seldom well imaged in either synthetic-aperture radar (SAR) or real-aperture (RAR) images of the ocean (Alpers et al., 1981). A polarimetric technique has been investigated (Schuler et al., 1993) which increases a radar's sensitivity to ocean wave tilting when the waves have a component of their propagation vector in the azimuthal direction. The technique offers improvement for polarimetric measurements of azimuthal wave slope spectra. A modification of this technique involving wave-induced changes of the polarization signature location offers a means of measuring azimuthal wave spectra for both polarimetric SAR and RAR. This method senses wave-tilts directly and does not require knowledge of the microwave modulation transfer function.

In the case of RAR images, cross section modulation by ocean waves is normally attributed to two principal sources, tilt modulation and, hydrodynamic modulation. The effect of these modulations is described mathematically by a complex modulation transfer function (MTF). For radar images of ocean waves both of these modulation sources roll-off to zero in the azimuthal direction. Therefore, complete two-dimensional k-space wave spectra derived from microwave data are often quite different than the physical ocean spectra. Evidence will be presented to show that a new source for backscatter modulations will result when the polarization properties of the scattering matrix are utilized specifically to sense wave tilts occurring in the azimuthal direction. The improvement in the fidelity of 2-D wave spectra created using optimal polarizations was investigated using a RAR ocean imaging model. The new method was derived from observations made on the properties of ocean polarization signatures. The new imaging technique reported here utilizes linear co-polar signature information to maximize a microwave instrument's sensitivity for azimuthally traveling waves.

Resolved wave tilts create a modulation of the cell polarization orientation which, in turn, modulates the backscatter intensity in an image. Critical to the success of the new techniques is the property that ocean linear co-polar signatures have regions which are highly sensitive to wave tilts. When an image is processed using a polarization orientation which maximizes this sensitivity, tilt perturbations due to azimuthally-traveling ocean waves have a large effect on the backscatter intensity.

This polarization orientation modulation acts as a new source-term for the overall microwave modulation transfer function. The magnitude and phase of this modulation have been quantitatively evaluated. The determination of the magnitude was demonstrated by making polarization gratings in P-band SAR images of the ocean. The polarization modulation transfer function contribution has also been evaluated using signatures developed from a theoretical tilted-Bragg model. The magnitude of the polarization modulation contribution to the MTF is equal to 2-5 for mid-range incidence angles. The effect is in phase with the tilt-modulation and has a phase of 90° relative to the hydrodynamic term.

2.0 APPLICATION TO WAVE SPECTRAL MEASUREMENTS

A model (Lyzenga, 1988) for the radar imaging of ocean waves has been modified to include both the amplitude and the phase effects of the new polarization modulation source term. Results using this model indicate that undesirable effects such as distortion and spectral-splitting of the actual spectrum may be greatly reduced for the case of azimuthally traveling waves.

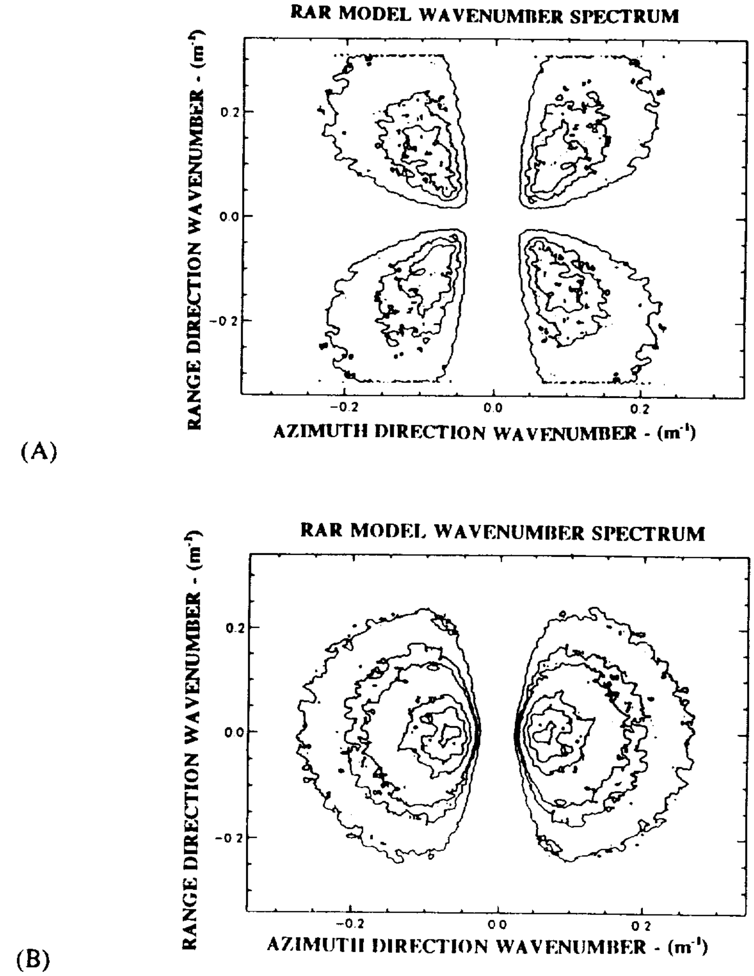

Fig1(A-B): Conventional Model RAR spectrum (A), and the Model RAR spectrum modified to include the new polarization term (B). The spectrum of (B) is similar in shape to the input waveslope spectrum, whereas the spectrum of (A) exhibits spitting and distortion about the $\Phi=0$ direction

Figure 1 shows comparisons made between conventional RAR spectra, and spectra developed with the new polarization modulation term included. Fig.1(A) shows the conventional RAR waveslope spectra, with the dominant wave ($\lambda = 100$m, significant waveheight $h_s = 3$m) traveling in the azimuthal direction ($\Phi = 0°$). Severe spectral splitting (abnormal four-lobed pattern) and distortion occurs because of the roll-off of the transfer function as the direction approaches $\Phi=0$. Fig.1(B) includes a polarization modulation term of magnitude 3.0 in phase with the tilt modulation, but having a $\cos\Phi$ dependence. Fig.1(B) indicates that polarization modulation MTF contributions are capable of compensating for distortions in the RAR spectra which are due to azimuthal roll-off of the modulation transfer function.

3.0 POLARIMETRIC SIGNATURE MODULATION

A JPL AIRSAR image (20 July 1988) of azimuthally traveling Pacific swell occurring off the coast of San Francisco was used to apply the new techniques to SAR images rather than RAR images, or models. The wave-induced intensity modulations in this image were strong and essentially uni-directional. The modulations were likely produced by velocity-bunching effects. A first attempt to enhance the wave modulations by changing the linear polarization through a range of values did not produce any significant changes. This was probably due to the strength of the velocity-bunching effects and a mismatch in phases between this effect and the polarization modulation. The original technique was then modified to detect changes in location of the polarization signature rather than intensity modulations. A strip image parallel to the azimuthal direction was formed which had pixel averaging (20) in the range direction and (2) in the azimuthal direction. Polarization signatures were formed for 350 cells formed parallel to the direction of wave propagation. Gates were set at the peak at other points in the signature to sense wave-induced movement parallel to the Orientation axis of the signature. Fig 2 shows a power waveslope spectrum of the strip. this SAR wave spectrum shows a strong peak at a wavenumber $k=.032\ m^{-1}$ indicating the presence of a dominant wave of 192 m wavelength.

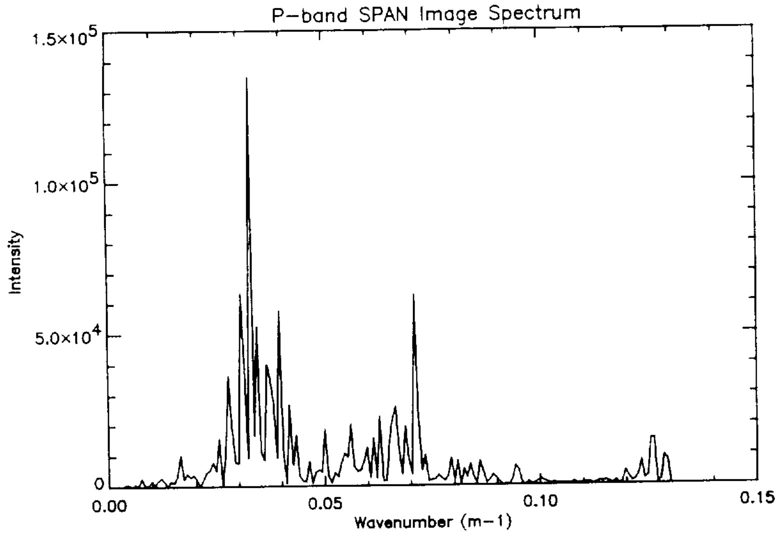

Fig. 2: SAR intensity waveslope spectrum for the image strip.

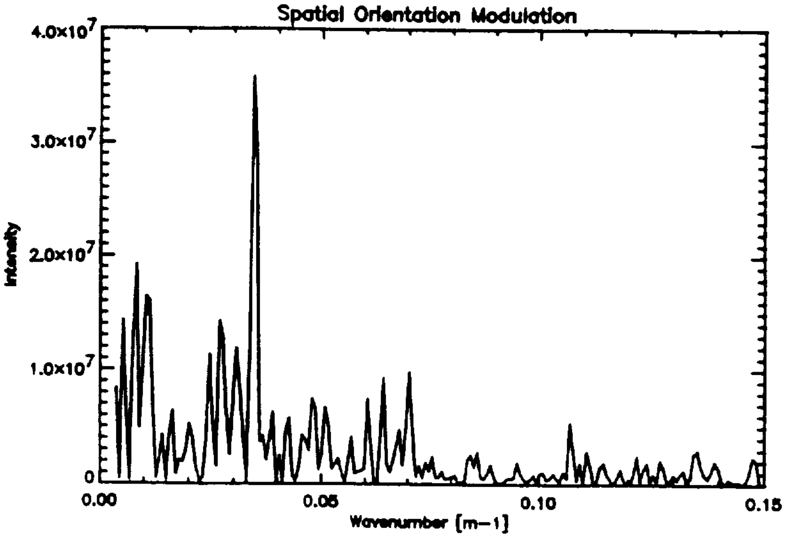

Fig. 3: Polarization orientation modulation spectrum for the same azimuthally-traveling waves.

Fig. 3 gives a polarization orientation modulation spectrum for the strip which, again, has a strong peak at the same wavenumber position. The signatures used to produce Fig.3 were all normalized to unity to minimize any intensity modulation. The peak is produced by signature location changes due to wave slopes. This preliminary study indicates that in cases where changes in the polarization signature morphology are slight, slope induced orientation changes can be detected - and possibly measured. The technique works for the ocean (or selected land areas) where the signature is sharply peaked and relatively constant.

4.0 CONCLUSIONS

A polarimetric technique for improving the visibility of waves, whose propagation direction has an azimuthal component, in RAR or SAR images has been investigated. The technique shows promise as a means of producing more accurate 2-D polarimetric RAR ocean wave spectra. For SAR applications domination by velocity-bunching effects may limit its usefulness to long ocean swell. A modification of this technique involving measurement of polarization signature modulations in the image is useful for detecting waves in SAR images and, potentially, estimating RMS wave slopes.

REFERENCES

Alpers, W.R., D.B. Ross, and C.L. Rufenach, 1981, "On the Detectability of Ocean Surface Waves by Real and Synthetic Aperture Radar", J. Geophys. Res., vol.86, pp.6481-6498.

Schuler, D.L., J.S. Lee, and K. Hoppel, 1993, "Polarimetric SAR Image Signatures of the Ocean and Gulf Stream Features", accepted for publication in IEEE Trans. Geosci. and Remote Sensing.

Lyzenga, D.R., 1988, "An Analytic Representation of the SAR Image Spectrum for Ocean Waves", J. Geophys. Res., vol.93, pp.13859-13865.

N95- 23954

AN IMPROVED ALGORITHM FOR RETRIEVAL OF SNOW WETNESS USING C-BAND AIRSAR

Jiancheng Shi, Jeff Dozier and Helmut Rott
Center for Remote Sensing and Environmental Optics (CSL/CRSEO)
University of California, Santa Barbara, CA 93106, USA
and
Institute for Meteorology and Geophysics
University of Innsbruck, Innrain 52, A-6020 Innsbruck, Austria

INTRODUCTION

Backscattering measurements by SAR from wet snow covered terrain are affected by two sets of parameters: (1) sensor parameters which include the frequency, polarization, and viewing geometry, and (2) snowpack parameters which include snow density, liquid water content, particle sizes and shapes of ice and water, type of the correlation function and its parameters of surface roughness.

The identified scattering mechanics of wet snow-covered terrain from the model predictions and measurements of the polarimetric properties (Shi et al, 1992) shows that the first-order surface and volume scatterings are dominated scattering source. We can construct, in general, the backscatter model of wet snow-covered terrain with two components:

$$\sigma_t^{pp} = \sigma_v^{pp} + \sigma_s^{pp} \tag{1}$$

where σ is the backscattering coefficient. pp indicates polarization. The subscript t, s, and v represent the total backscattering, the surface backscattering from the air-snow interface, and the volume backscattering from the snowpack, respectively. The relation between backscattering and snow wetness is controlled by the scattering mechanism. When the surface is smooth, volume scattering is the dominant scattering source. As snow wetness increases, both the volume scattering albedo and the transmission coefficients greatly decrease. This results in a negative correlation between the backscattering signals and snow wetness. When the surface is not smooth, increasing snow wetness results in greatly increased surface scattering interaction and surface scattering becomes the dominant scattering process. Therefore, a positive correlation between the backscattering signals and snow wetness will be observed. The characteristics of above relationships makes it difficult to derive an empirical relation from field measurements and a physical based algorithm is needed for a large region snow wetness estimation.

Our previous works (Shi et al., 1993) indicated that the ratios of σ^{vv} to σ^{hh} and σ^{vvhh} to σ^{hh} could be used for snow wetness retrieval at C-band. The development of the inversion model was based upon the relations of the first-order surface and volume backscattering model predictions. The small perturbation model was used to predict the relations between snow wetness and above ratios, which are independent of surface roughness and only dependent on the local incidence angle and snow dielectric property. Our resent study (Shi et al,. 1993) showed an over-estimating snow wetness by this method. The tested results had an average relative error about 23 percent and the maximum error could research 50 percent. This is because the small perturbation model can only be applied to smooth surface. The accuracy of this model is generally within 2 dB for surfaces with standard deviation of surface height less than 0.1 of the wavelength and small surface correlation length (kl less than 3) (Chen et al., 1988).

Due to the surface roughness parameters of most of natural surface are outside the range of the valid conditions for the Small Perturbation and Geometric Optical models, application of these surface scattering models are greatly limited to certain types of the surface roughness conditions. The recently developed Integral Equation Model (IEM) (Fung et al., 1991 and 1992) allows a much wider range of the surface roughness conditions. However, it does not allow to apply this model directly to infer geophysical parameters because of the complicity of this model and the limited independent observations provided by SAR measurements.

This study shows our continue efforts on developing and testing the algorithm for retrieval snow wetness using C-band JPL AIRSAR data. We show (1) a simplified surface backscattering model particularly derived for wet snow physical conditions from the numerical simulations by IEM model, and (2) snow wetness retrieval model test and comparison with ground measurements using C-band AIRSAR data,

INVERSION MODEL DEVELOPMENT

The volume backscattering coefficient is a function of the permittivity and the volume scattering albedo (depending on snow density, wetness, particle size, size variation and shape). Under the spherical grain or random oriented particles assumption, the relationship for the first-order volume backscattering signals of VV and HH polarizations can be also obtained:

$$D_T(\theta_i, \varepsilon_r) = \frac{\sigma_v^{vv}}{\sigma_v^{hh}} = \frac{\Upsilon_{vv}^2(\theta_i, \varepsilon_r)}{\Upsilon_{hh}^2(\theta_i, \varepsilon_r)} \tag{2}$$

where Υ_{vv}^2 and Υ_{hh}^2 are double pass of the power transmission coefficients.

The surface backscattering is a function of the permittivity of wet snow (depending on snow density and wetness) and the roughness of the air-snow interface which is described by the auto-correlation function of random surface height, the standard deviation of the surface height, and the correlation length. Due to complicity of IEM model and the limited number of independent observations from the polarimetric SAR, we need to minimize or combine these factors in order to develop an algorithm of measuring snow wetness.

Using IEM model, we simulated surface backscattering coefficients of σ_s^{vv} and σ_s^{vvhh} at C-band for the possible snow wetness and surface roughness conditions. The simulated backscattering coefficients cover the ranges for snow wetness from 1 percent to 13 percent, for the incidence angle from 25° to 70°, for the standard deviation of random surface height from 0.1 mm to 15 mm, and for the surface correlation length 0.5 cm to 25 cm. Through statistical analysis, we found a simplified form for the backscattering coefficients

$$\sigma_s^{hh} = |\alpha_{hh}|^2 \left[\frac{1.12 S_R}{(0.11 + S_R)}\right]^{1.2} \tag{3}$$

$$\sigma_s^{vvhh} = Re[\alpha_{vv}\alpha_{hh}] \left[\frac{1.06 S_R}{(0.17 sin(\theta_i) + S_R)}\right]^{1.2} \tag{4}$$

$$\sigma_s^{vv} = \frac{|\alpha_{vv}|^2 1.05 S_R cos(\theta_i)}{(0.46 sin^2(\theta_i) + 1.3 S_R cos(\theta_i))} \tag{5}$$

where α_{vv} and α_{hh} are same as that for the small perturbation model and given in (Tsang et al,. 1985). The S_R is the surface roughness parameter, which is $S_R = ks^2 W cos^2(\theta)$. W is the Fourier transform of the power spectrum of the surface correlation function.

As predicated by the models of the first-order surface and volume backscattering, the correlation coefficient in H and V channel is perfect correlated. The real part of the cross product of VV and HH complex scattering elements, $Re[S_t^{vv} S_t^{hh*}]$, can be related to the surface and volume backscattering coefficients by

$$\sigma_t^{vvhh} = Re[S_t^{vv} S_t^{hh*}] = \sigma_v^{vvhh} + \sigma_s^{vvhh} \tag{6}$$

The ratio of $\sigma_v^{vvhh}/\sigma_v^{hh}$ can be written as

$$D_{TV}(\theta_i, \varepsilon_r) = \frac{\sigma_v^{vvhh}}{\sigma_v^{vv}} = \frac{Re[T^2_{vvhh*}]}{\Upsilon^2_{vv}} \tag{7}$$

Using Equations (1) to (7), we can derive two inversion formula for snow wetness retrieval as

$$D_{TV}\sigma_t^{vv} - \sigma_t^{vvhh} = D_{TV}\sigma_s^{vv} - \sigma_s^{vvhh} \tag{8}$$

and

$$D_T\sigma_t^{hh} - \sigma_t^{vv} = D_T\sigma_s^{hh} - \sigma_s^{vv} \tag{9}$$

In Equation (8) and (9), there are only two unknowns: the snowpack permittivity and the surface roughness parameter S_R. Therefore, we can obtain the estimations of snow wetness and surface roughness parameter by solve the equation (8) and (9) simultaneously.

COMPARISON WITH AIRSAR MEASUREMENTS

The data used in this study for testing the algorithm are from the NASA/JPL airborne imaging polarimeter overflying the central part of the Ötztal test site on June 25, 1991. The experiment consisted of three flight passes at a flight altitude about 10,600 meter a.s.l. Two of the flight lines were aligned in E-W direction, shifted by 4 km. in latitude. Another was collected from an W-E flight line, resulting in opposite look direction.

At the time of the radar survey the snow cover was wet at all elevation zones. In ground sampled data, the liquid water content in the top snow layer (5 cm), obtained from average values at 0 and 5 cm, was ranged from 4.0 to 7.2 percent by volume. Snow grain radii were from 1.0 to 2 mm in the top snow layer. The snow densities and depths (over glacier ice) ranged from 460–530 kg m^{-3} and from 40–205 cmrespectively. In addition to snow physical parameters measurements, surface roughness was measured by a lasermeter. The standard deviations of surface height were 0.1–0.7 cm; correlation lengths ranged 1–23 cm.

To test the algorithm for measuring snow wetness over a large area, snow-covered area map was first obtained and non-snow-covered area was masked. Secondly, the stokes matrix for a given pixel was determined by the mean value within a 3 × 3 window in order to reduce the effect of image speckle. Figure 1 shows two maps of the inversion-derived snow wetness, which are derived from two images with E-W flight passes. The image brightness is proportional to the snow wetness by volume. The black region is non-snow-covered area. At most of the lower elevation region, the inferred liquid water content of the top snow layer was in the order of 5 to 7 percent by volume. It decreases to 1 or 4 percent at the higher elevations. This agrees well ground regional conditions. Both snow wetness maps derived from different incident angle showed a consistent results within 2 percent. Figure 2. shows the comparisons between the field measurements and the SAR derived snow wetness for the locations where the ground measurements were available. The line indicates where the snow wetness is exactly same from the ground and SAR derived measurements. The measurements above and below this line indicate an over-estimation and under-estimation, respectively. The relative error was within 25 percent from all measurements. In overall, the algorithm performed well and provided a consistent results, less than 2 percent for absolute values, at different incidence angles. The magnitude of the error is within the range we expected. Since the algorithm performed at different incident angle produces the consistent result, it is also possible to calibrate the algorithm.

CONCLUSIONS

This study shows recent results of our efforts to develop and verify an algorithm for snow wetness retrieval from a polarimetric SAR. Our algorithm is based on the first-order scattering model with consideration of both surface and volume scattering. It operates at C-band and requires only rough information about the ice volume fraction in snowpack. Comparing ground measurements and inferred from JPL AIRSAR data, the results showed that the relative error inferred from SAR imagery was within 25 percent. The inferred snow wetness from different looking geometries (two flight passes) provided consistent results within 2 percent. Both regional and point measurement comparisons between the ground and SAR derived snow wetness indicates that the inversion algorithm performs well using AIRSAR data and should prove useful for routine and large-area snow wetness (in top layer of a snowpack) measurements.

REFERENCES

Chen, M. F. and A. K. Fung, 1988, "A numerical study of the regions of validity of the Kirchhoff and small perturbation rough surface scattering models," *Radio Science*, vol. 23, pp 163–170.

Fung, A. K. and K. S. Chen, 1991, "Dependence of the surface backscattering coefficients on roughness, frequency and polarization states", *Int. J. Remote Sensing*, vol. 13, no. 9, pp. 1663–1680.

Fung, A. K., Z. Li, and K. S. Chen, 1992, "Backscattering from a randomly rough dielectric surface," *IEEE Transactions on Geoscience and Remote Sensing*, vol. 30, no. 2, pp. 356–369.

Shi, J. and J. Dozier, 1992, "Radar response to snow wetness," *Proceedings IGARSS '92*, vol. 2, pp. 927–929.

Shi, J., J. Dozier, and H. Rott, 1993, "Deriving snow liquid water content using C-band polarimetric SAR", in press *Proceedings IGARSS '93*.

Tsang, L., J. A. Kong, and R. T. Shin, 1985, in "Theory of microwave remote sensing," Wiley publication, New York, pp. 108. 1992.

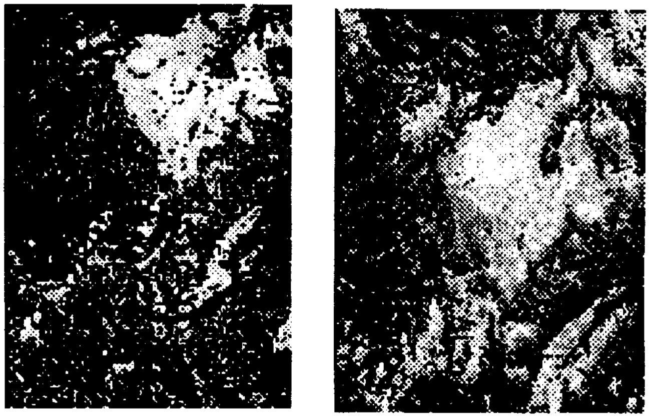

Figure 1. C-band SAR derived snow wetness maps.

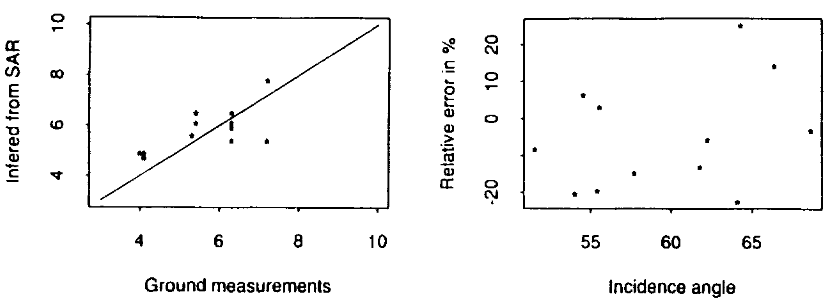

Figure 2. Comparison of ground measurements with SAR derived snow wetness.

N95- 23955

POLARIMETRIC RADAR DATA DECOMPOSITION AND INTERPRETATION

Guoqing Sun[1] and K. Jon Ranson[2]

[1] Science Systems & Application, Inc. 5900 Princess Garden Parkway,
Suite 300, Lanham, MD, 20706, USA.
[2] Biospheric Sciences Branch, GSFC Greenbelt, MD 20771, USA.

1. INTRODUCTION

Significant efforts have been made to decompose polarimetric radar data into several simple scattering components. The components which are selected because of their physical significance can be used to classify SAR image data. If particular components can be related to forest parameters, inversion procedures may be developed to estimate these parameters from the scattering components.

Several methods (van Zyl, 1989; Freeman and Durden, 1992; van Zyl, 1992) have been used to decompose an averaged Stoke's matrix or covariance matrix into three components representing odd (surface), even (double-bounce) and diffuse (volume) scatterings. With these decomposition techniques, phenomena, such as canopy-ground interactions, randomness of orientation and size of scatterers, can be examined from SAR data.

In this study we applied the method recently reported by van Zyl (1992) to decompose averaged backscattering covariance matrices extracted from JPL SAR images over forest stands in Maine, USA. These stands are mostly mixed stands of coniferous and deciduous trees. Biomass data have been derived from field measurements of DBH and tree density using allometric equations. The interpretation of the decompositions and relationships with measured stand biomass are presented in this paper.

2. DECOMPOSITION

van Zyl (1992) showed that for azimuthally symmetrical terrain in the monostatic case, the average covariance matrix of backscattering can be decomposed as:

$$[T] = C \begin{bmatrix} 1 & 0 & \rho \\ 0 & \eta & 0 \\ \rho^* & 0 & \xi \end{bmatrix} = \sum_{i=1}^{3} \lambda_i k_i \, k_i^{+} \qquad (1)$$

where $C = \langle S_{hh} S_{hh}^* \rangle$, $\rho = \langle S_{hh} S_{hv}^* \rangle$, $\eta = 2\langle S_{hv} S_{hv}^* \rangle / C$, $\xi = \langle S_{vv} S_{vv}^* \rangle / C$. The $\lambda_i, i=1,2,3$ are the eigenvalues of $[T]$. $k_i, i=1,2,3$ are the corresponding eigenvectors and + means *adjoint*. Since the eigenvectors are unitary vectors and the sum of the eigenvalues equals the total power of the backscattering, $\lambda_1, \lambda_2, \lambda_3$, are the backscattering powers contributed by odd, even and diffuse backscattering components, respectively. We also note that the λ_3 is exactly the backscattering power at cross-polarizations, i.e. $2\langle S_{hh} S_{hv}^* \rangle$. In terms of backscattered power, this algorithm decomposes the power from co-polarized returns into odd and even scattering components. For those targets with $\rho = 0$, depending on the $\xi > 1$ *or* $\xi < 1$, one of the two eigen values (either λ_1, or λ_2) equals the HH return and the other the VV return. When $\xi = 1$, the odd and even scattering components are equal.

3. RESULTS AND DISCUSSION

3.1. Decomposition and Forest Biomass

Figure 1 presents scatter plots of total above-ground fresh biomass of 47 forest stands versus $\lambda_1, \lambda_2, \lambda_3$ and σ^o at HH, HV and VV polarizations at L band. Table 1 summarizes the correlation coefficients for scattering components and measured biomass. Comparing the two plots in the third row demonstrates that λ_3 (diffuse scattering) is identical to the sum of the cross-polarization backscatter cross sections. The $\lambda 2$ (even scattering component) has higher correlation with biomass than the odd scattering component. In the first-order backscatter models, the odd scattering is from crown backscattering and direct backscattering from ground surface. If the canopy is dense and tall, crown backscattering will be the major source and the odd scattering should have higher correlation with forest biomass. This is not obvious from the data shown in Figure 1 or listed in Table 1.

3.2. Decomposition and Forest Classes

Table 2 lists the decomposition results of several classes at C, L, and P bands. Generally, the odd scattering is always the major component. The even scattering component is higher for forest stands with large and dense trees at L and P bands. The higher entropy values of dense forest stands at L and P bands show a high degree of disorder (randomness) of scatterers. At C band, except for Bog and Red Pine sites, all sites have the similar entropies.

3.3. Decomposition of modeled Scattering

Backscatter models (Sun, 1990) were used to simulate backscattering from the 47 stands. The tree density and size for a stand were from field measurements, but trees were assumed to be pure hemlocks and the ground surface to be a rough surface similar to an old cut area near these stands. The decomposition of SAR data and modeled scattering matrices at L band were compared in Figure 2. The simulated components have good correlation with biomass. Though the comparison between SAR and simulated data is crude, it seems that model gives reasonable results in terms of even and diffuse scattering but not for odd scattering.

4. SUMMARY

The decomposition method partitions the co-polarization return into odd and even scattering components. The partition depends on two parameters, i.e. ρ and ξ only. It helps to classify radar polarimetry return into general groups of scattering behavior.

The HV backscatter or diffuse components has the best correlation with forest biomass.

Comparing to HV backscatter, HH and VV backscatters have higher signal to noise ratio and are desirable for developing an inversion algorithm for forest parameter estimation. More works, however, need to be done to separate scattering components heavily influenced by ground surface from the co-polarization signatures.

REFERENCES

Freeman, A. and S. Durden, 1992, Fitting a three-component scattering model to polarimetric SAR data, *Summaries of the Third Annual JPL Airborne Geoscience Workshop,* Volume 3, AIRSAR Workshop, Ed. J. van Zyl, pp. 56-58.

Sun, G., 1990, Radar Backscatter Modeling of Coniferous Forest Canopies, Ph. D. Dissertation, University of California, Santa Barbara. 126 p.

van Zyl, J. J., 1989, Unsupervised classification of scattering behavior using radar polarimetry data, *IEEE Transactions on Geoscience and Remote Sensing, Vol. 27, No. 1*, pp. 36-45.

van Zyl, J. J., 1992, Application of Cloude's target decomposition theorem to polarimetric imaging radar data, *Proceedings of SPIE, Vol. 1748, Radar Polarimetry, Eds. H. Mott and* W. M. Boerner, 23-24 July 1992, San Diego, California, pp. 184 - 191.

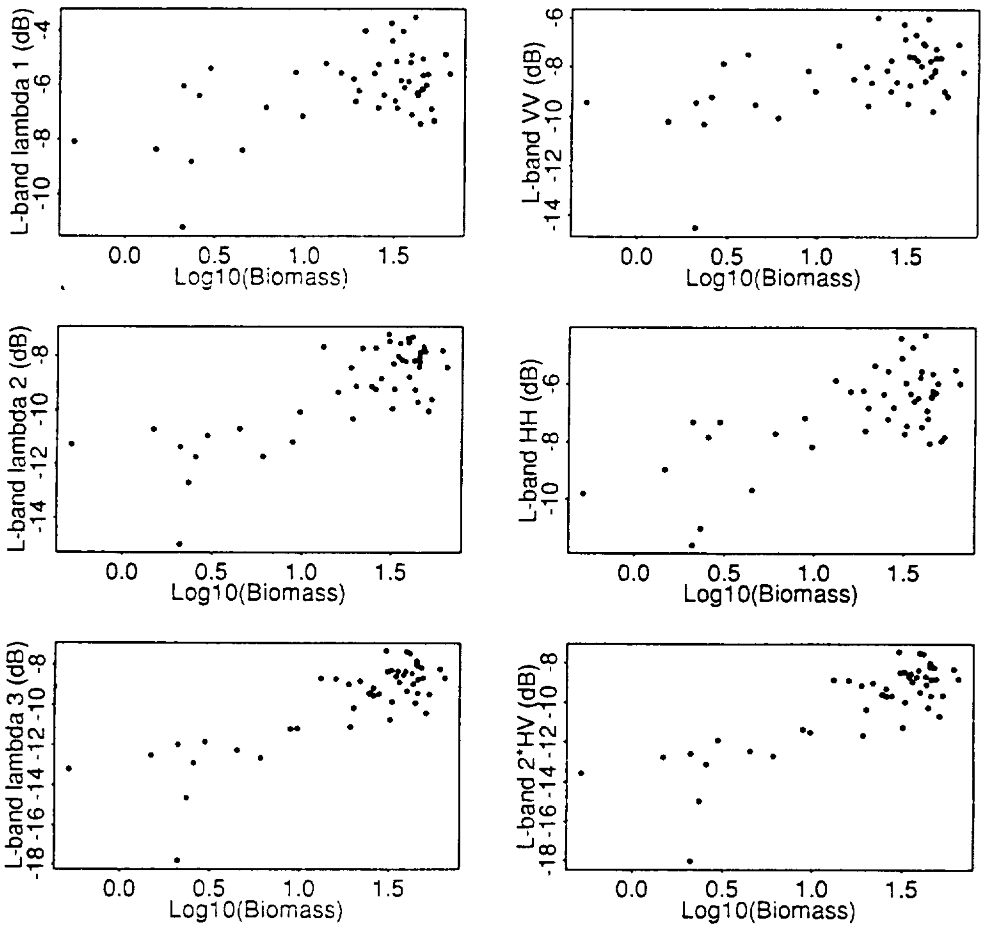

Figure 1. Comparisons of SAR original HH, VV and HV backscattering with decomposed scattering in terms of their relation to total above-ground fresh biomass.

Table 1. List of correlation parameters to biomass for variables in Figure 1 ($y = b_0+b_1x$).

	b_0	b_1	R^2	F-value	R.S.E
λ_1	2.470	0.193	0.281	17.54	0.436
λ_2	3.458	0.237	0.601	67.79	0.3245
λ_3	3.260	0.201	0.680	95.73	0.291
VV	2.971	0.202	0.316	20.80	0.425
HH	2.843	0.225	0.455	37.59	0.379

Table 2. Decomposition of SAR data at C, L and P bands.

Site	λ_1(%)	λ_2(%)	λ_3(%)	Total Power	Entropy
C Band					
Grass	57.94	23.09	18.97	0.2176	0.8829
Bog	78.15	12.02	9.83	0.5508	0.6147
Regen	58.71	23.16	18.13	0.3183	0.8748
Clear	61.84	20.34	17.82	0.4676	0.8451
Aspen	57.73	20.49	21.78	0.4632	0.8865
Mixed	63.55	19.74	16.71	0.4382	0.8259
Hemlock	62.64	20.73	16.63	0.4385	0.8352
Red Pine	49.38	21.59	29.03	0.2596	0.9452
Spruce	60.71	20.01	19.28	0.5368	0.8576
L Band					
Grass	81.88	10.56	7.56	0.0700	0.5429
Bog	84.00	8.03	7.97	0.3086	0.5011
Regen	53.14	25.56	21.30	0.1900	0.9230
Clear	61.32	21.48	17.20	0.3105	0.8492
Aspen	42.54	30.73	26.73	0.3921	0.9820
Mixed	46.42	29.89	23.69	0.3746	0.9634
Hemlock	45.69	28.27	26.04	0.4263	0.9698
Red Pine	44.06	27.68	28.24	0.5585	0.9774
Spruce	50.73	27.13	22.14	0.5488	0.9394
P Band					
Grass	89.64	6.87	3.49	0.0848	0.3631
Bog	88.48	6.32	5.20	0.1622	0.3975
Regen	60.42	25.01	14.57	0.1516	0.8480
Clear	63.24	22.16	14.60	0.2245	0.8230
Aspen	52.37	23.18	24.45	0.3627	0.9303
Mixed	49.13	30.07	20.80	0.3474	0.9440
Hemlock	48.83	28.37	22.80	0.4596	0.9508
Red Pine	58.95	24.64	16.41	0.6692	0.8677
Spruce	53.43	25.28	21.29	0.4608	0.9210

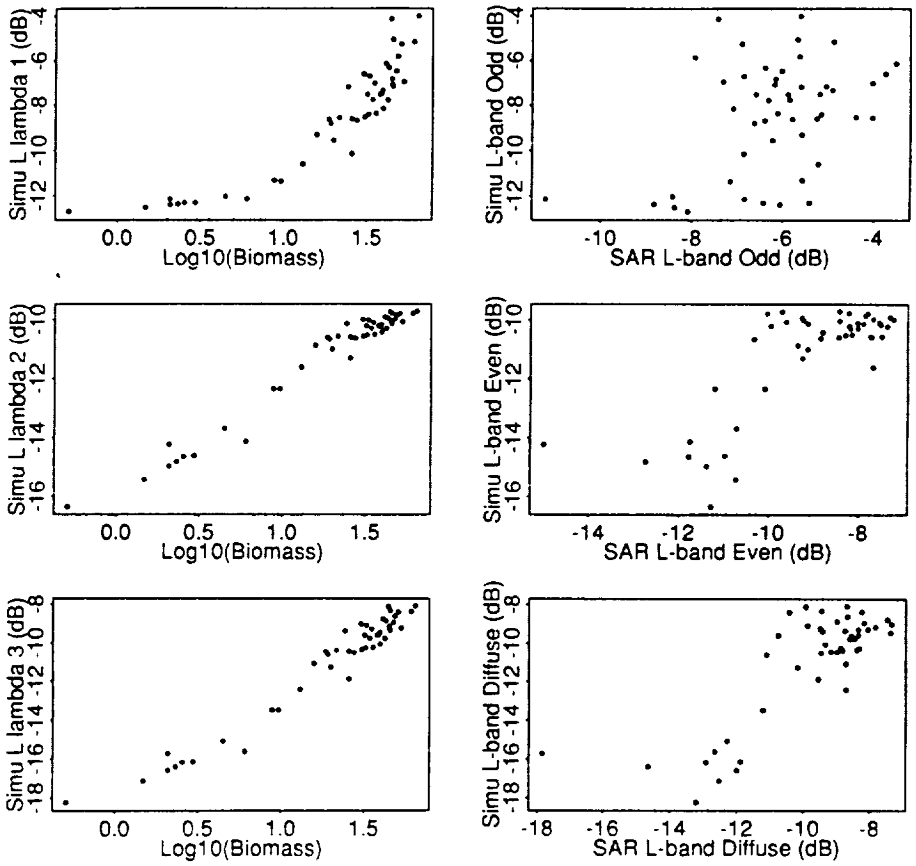

Figure 2. Decompositions of modeled backscattering and comparison with SAR data.

C-2

N95- 23956

SYNERGY BETWEEN OPTICAL AND MICROWAVE REMOTE SENSING TO DERIVE SOIL AND VEGETATION PARAMETERS FROM MAC EUROPE 91 EXPERIMENT

TACONET[1], O., BENALLEGUE[2], M., VIDAL[3], A., VIDAL-MADJAR[1], D.,
L. PREVOT[4],M. NORMAND[2]
1 Centre de Recherches en Physique de l'Environnement Terrestre et Planétaire
10-12, avenue de l'Europe 78140 VELIZY (France)
2 CEMAGREF, Division Hydrologie- BP 121 F-92185 Antony Cedex (France)
3 CEMAGREF/LCT, 361, rue J-F Breton .B.P. 5095 34033 Montpellier Cedex 1
4 INRA, Bioclimatologie, BP 91, 84140 MONTFAVET (France)

I. INTRODUCTION

The ability of remote sensing for monitoring vegetation density and soil moisture for agricultural applications is extensively studied. In optical bands, vegetation indices (NDVI, WDVI) in visible and near infrared reflectances are related to biophysical quantities as the leaf area index, the biomass. In active microwave bands, the quantitative assessment of crop parameters and soil moisture over agricultural areas by radar multiconfiguration algoritms remains prospective. Futhermore the main results are mostly validated on small test sites (Ulaby et al. 1984), but have still to be demonstrated in an operational way at a regional scale.

In this study, a large data set of radar backscattering has been achieved at a regional scale on a french pilot watershed, the Orgeval, along two growing seasons in 1988 and 1989 (mainly wheat and corn). The radar backscattering was provided by the airborne scatterometer ERASME, designed at CRPE, (C and X bands and HH and VV polarizations). Empirical relationships to estimate water crop and soil moisture over wheat in CHH band under actual field conditions and at a watershed scale are investigated. Therefore the algorithms developped in CHH band are applied for mapping the surface conditions over wheat fields using the AIRSAR and TMS images collected during the MAC EUROPE'91 experiment. The synergy between optical and microwave bands is analysed.

2. THE ORGEVAL CAMPAIGNS ' 88,89 and 91

The characteristics of the scatterometer ERASME is presented in Table 1. The French test site is the Orgeval experimental watershed of 5 by 5 km^2 (France), mainly covered by wheat and corn with silt loamy soils. 49 fields of wheat and 12 fields of corn are identified. During 1988 (AGRISCATT), the scatterometer ERASME was performed along a 17 km axis through the basin during June and July with 17 test fields (wheat and corn). In 1989, it was performed along 14 crossed-axis covering the watershed (21 test fields) for every month from March to December 1989.

During the Mac-Europe Campaign'91, flights of the NASA airborne sensors (the multispectral radiometer TMS, the synthetic aperture radar AIRSAR) have been done, simultaneously with flights of ERASME.The two intensive periods were two weeks, the first mid June and the second mid July. 2 test fields (wheat and corn) were instrumented. Only two enough clear TMS images are available, the 17 July and the 22 July. The concomittant AIRSAR image is the 16 July.Ground truth measurements related to soil and vegetation are soil moisture, soil profiles with a 2 meter pin-profiler, leaf area index, crop height, biomass and water content.

3. EMPIRICAL RELATIONS IN CHH BAND

Considering the distribution of radar cross sections at 20 and 40 degrees of incidence angles with the vegetation water content (Figures 1 and 2), it appears that the behaviour of radar backscattering can be divided in two cases, low vegetation cover and high vegetation cover. For vegetation water content lower than 2, the cross sections for both 20 and 40 degrees are highly variable. The vegetation water content is not the

Table1 Radar Characteristics of ERASME

Type	Forward looking FM/CW
Frequencies	5.35 GHz and 9.65 GHz
Transmitted Power	11.2 dBm at C band 20 dBm at X band
Modulation	Sawtooth, 3ms of period
Antenna Axis Position	23°, 38° and 45°
Range Resolution	0.97m at 23° 1.30m at 38° and 45°
Antenna Range	±10° in elevation ±2° in azimuth
Altimeter Antenna	Nadir Horn
Pixel Size	20m by 10m
Accuracy	1dB ±7° apart the axis

Figure 1- Radar backscattering at 20 degree of incidence from Orgeval'88-89 related to vegetation water content in kg/m^2 and classified with soil moisture in cm^3/cm^3

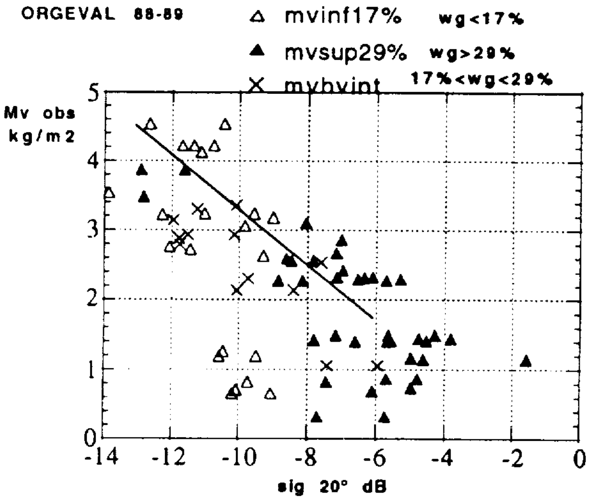

dominant parameter. The relevant parameter for radar cross sections is the soil moisture. For vegetation water content Mv higher than 2, it appears a linear relation between the radar cross sections and the vegetation water content. The radar backscattering is decrasing with increasing crop coverture. The soil moisture is no more an influent parameter.

3.1 Case of low vegetation cover

The relation of cross section with soil moisture Wg for bare soil is established using data points with the lowest values of vegetation cover (Mv<1kg/m2). A linear relation is obtained at 20 and 40 degree as proposed by Ulaby (1978):
The 2 obtained relations at 20 and 40 degrees are:

$$\sigma^0\text{soil}(20)= -12.1+0.18\ \text{Wg} \qquad (1)$$

$$\sigma^0\text{soil}(40)=-13.8+0.14\ \text{Wg} \qquad (2)$$

with comparable slopes and a shift of about 2dB.
This simple linear relation is obtained only for wheat culture. Linear relations between radar cross sections and soil moistures are no longer available for bare soils in the cases of corn sowing or of ploughs.

Linear relation between radar cross sections and soil moistures are obtained with low vegetation cover, (Mv< 3 kg/m2) (Figure 3). The relations at 20 and 40 degrees are:

$$\sigma^0\text{soil}(20)= -15.6+0.29\ \text{Wg} \qquad (3)$$

$$\sigma^0\text{soil}(40)=-14.9+0.14\ \text{Wg} \qquad (4)$$

The cloud model has been adjusted over wheat, taking only the attenuated part by the vegetation:

$\sigma^0= t^2\ \sigma^0\text{soil}$ and $t^2 = \exp(-2B\ \text{Mv}/\cos\theta)$ and $\sigma^0\text{soil}$ in dB= C1 - C2 θ + D Wg
with θ the incidence angle.

$$\sigma^0 \text{ in dB}= -8.69\ B\ \text{Mv}/\cos\theta\ -\text{C1} - \text{C2}\ \theta + \text{D Wg} \qquad (5)$$

The adjusted coefficients are:B=0.09,C1=-8.32,C2 =0.147,D=0.193 (comparable with results of Prévot et al,1993).

3.2 Case of high vegetation cover

For dense canopy (Mv>3kg/m2), the soil moisture is no more a relevant

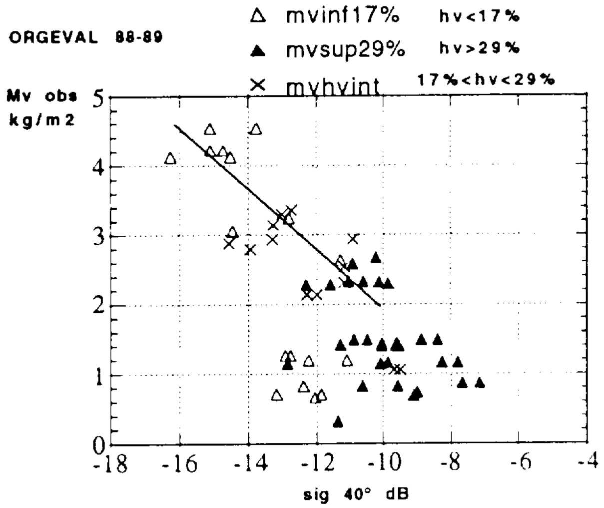

Figure 2- Radar backscattering at 40 degree of incidence from Orgeval'88-89 related to vegetation water content in kg/m^2 and classified with soil moisture in cm^3/cm^3

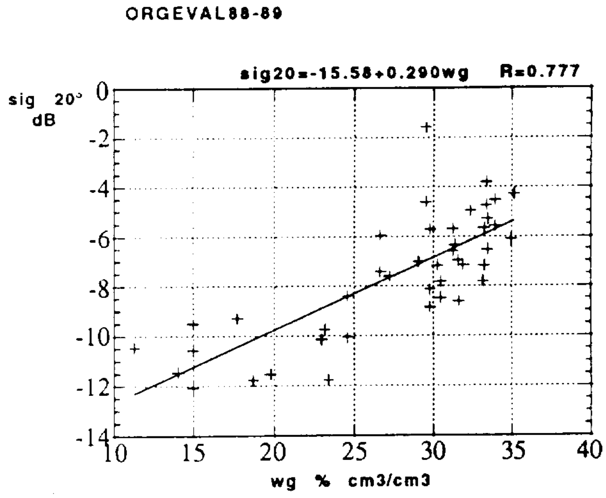

Figure 3: Linear regression between radar cross section and soil moisture over wheat for low cover canopy (vegetation water content<3 kg/m^3)

parameter to parameterize the radar cross section (see Figures 1 and 2). The cross sections at 40 degrees are related quasi linearly to vegetation water content. The radar backscattering is attenuated when the foliage density is increasing (Prévot et al., 1993). At 20 degrees, radar cross section is highly variable for the same foliage density indicating that other structural parmeters of canopy have to be accounted. Experimental linear relation between radar cross section and vegetation water content can be proposed from the data set.

At 40 degrees, $Mv=-0.35\sigma^0 dB-1.44$ (6)

But as the dependance of the cross sections with the soil moisture disappears, the formulation given by the attenuated part of the cloud model fitted for Mv<3kg/m^2 is no more available.

4. APPLICATION TO THE ORGEVAL'91/MAC-EUROPE EXPERIMENT

A map of the 49 fields of wheat over the basin is given in Figure 4. The synergy between the TMS (17 July) and the AIRSAR (16 July) images is investigated. The TMS image has been radiometrically calibrated and corrected from atmospherical diffusion in visible/near infrared bands. Approximate calibration of LAI (leaf area index) versus NDVI (Normalized Vegetation index) and vegetation water content (Mv) versus LAI are obtained over the reference field:

$LAI=-4.1+11.4\ NDVI$ (7)

$Mv=2.32+0.25\ LAI$ (8)

Spatial variations of NDVI and Mv over the wheat parcels are derived (Figure 5). As the magnitude of the estimated Mv are between 2.8 and 3.4 kg/m^2, only a map of the vegetation water content can derived from the radar cross section of the AIRSAR images (2 images around 45 degree of incidence with 2 flight directions, perpendicular and parallel to the average rows direction in the watershed). The algorithm related radar cross section and Mv (Eq. 7) has been used. An intercalibration between the AIRSAR and ERASME data is done before, as the AIRSAR data are systematically lower of about -3.5dB. Therefore AIRSAR data are decreased of -3.5dB and after of +1dB to approximate the cross sections at 40 degrees needed in Eq. 7. The value of -1 dB has been calculated from statistical relation between the ERASME data at 40 and 45 degree.

It has been noted that the derived vegetation (LAI,Mv) parameters from microwave algoritms are lower and more scattered than those deduced from the optical vegetation index. Nevertheless the accuracy of relationships using optical vegetation index is also to be assessed.

Figure 4- Map of wheat fields over the Orgeval

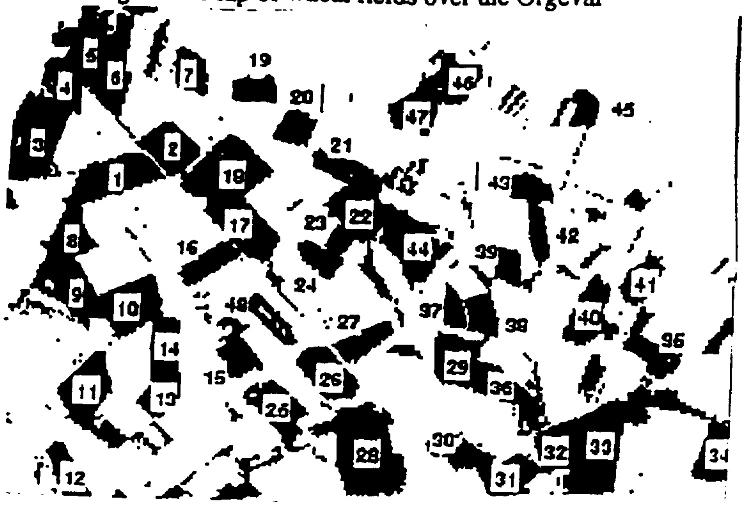

Figure 5: Spatial variations of NDVI and deduced vegetation water content Mv (kg/m^2) over wheat fields.

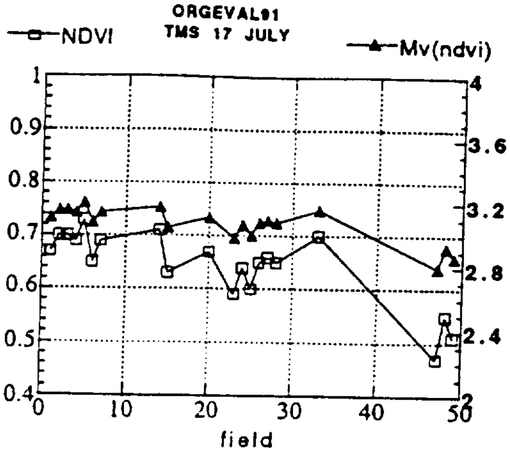

5- CONCLUSION

A complementary use of the optical and microwave bands is proposed. Over wheat, the knowledge of the vegetation index values appear necessary to discriminate dense or low vegetation cover over the wheat fields and choose the adequate microwave algoritm to derive either the soil moisture, either the water content of the vegetation. In CHH band, radar data at 20 and 40 degree can be used to derive soil moisture for low cover. Radar data at 40 degree are used to derive water content and are not saturating as soon as optical vegetation index NDVI.

Figure 6: Intercomparison of radar cross section from AISAR and ERASME

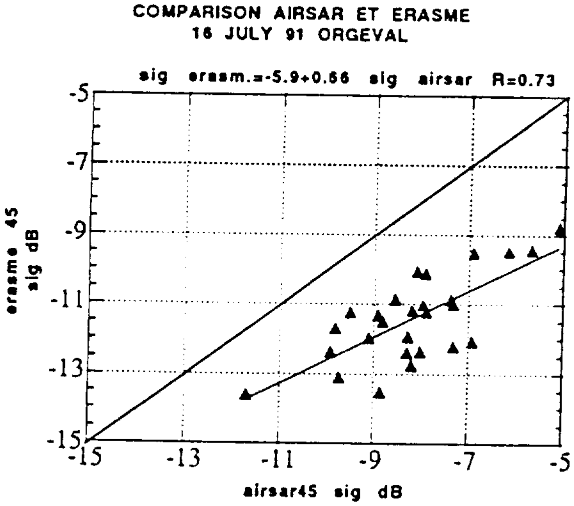

Figure 7: Simultaneous estimation of Leaf Area Index and vegetation water content from optical (TMS)and microwave (AIRSAR) images.

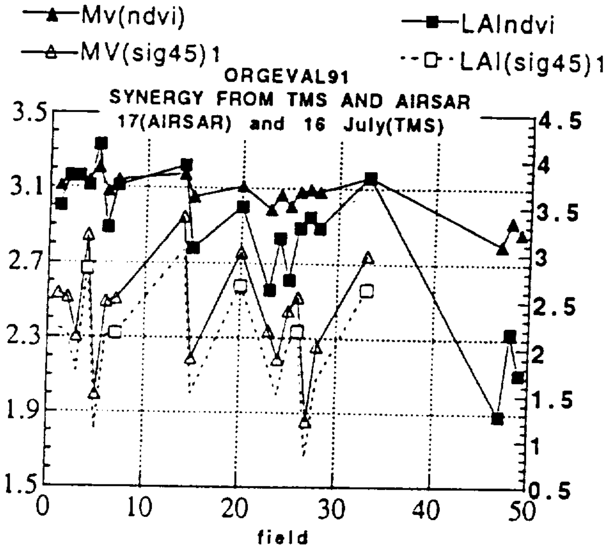

REFERENCES

Prévot, L., M. Dechambre, O. Taconet, D. Vidal-Madjar, M. Normand and S. Galle, 1993," Estimating the characteristics of vegetation canopies with airborne radar measurements, *Int. J. of Remot. Sens.*, to be published.

Ulaby,F., T. et al., 1978,"Microwave backscatter dependence on surface roughness, soil moisture and soil texture: Part 1-bare soil, *IEEE Trans. Geosci. Electron.*, vol. 16, no.4, pp.286-295.

Ulaby, F. T., C. T. Allen, G. Eger and E. Kanemasu, 1984, "Relating the microwave backscatteringf coefficients to leaf area index",*Remote Sens. Environ.*, vol.14, pp.113-133.

N95- 23957

SAR TERRAIN CLASSIFIER AND MAPPER OF BIOPHYSICAL ATTRIBUTES

Fawwaz T. Ulaby, M. Craig Dobson, Leland Pierce and Kamal Sarabandi

Radiation Laboratory
Department of Electrical Engineering and Computer Science
The University of Michigan
Ann Arbor, Michigan 48109-2122

1. INTRODUCTION

In preparation for the launch of SIR-C/X-SAR and design studies for future orbital SAR, a program has made considerable progress in the development of an SAR terrain classifier and algorithms for quantification of biophysical attributes. The goal of this program is to produce a generalized software package for terrain classification and estimation of biophysical attributes and to make this package available to the larger scientific community. The basic elements of the SAR terrain classifier are outlined in Figure 1. An SAR image is calibrated with respect to known system and processor gains and external targets (if available). A Level 1 classifier operates on the data to differentiate: urban features, surfaces and tall and short vegetation. Level 2 classifiers further subdivide these classes on the basis of structure. Finally, biophysical and geophysical inversions are applied to each class to estimate attributes of interest.

The process used to develop the classifiers and inversions is shown in Figure 2. Radar scattering models developed from theory and from empirical data obtained by truck-mounted polarimeters and the JPL AirSAR are validated. The validated models are used in sensitivity studies to understand the roles of various scattering sources (i.e., surface, trunk, branches, etc.) in determining net backscatter. Model simulations of σ° as functions of the wave parameters (λ , polarization and angle of incidence) and the geophysical and biophysical attributes are used to develop robust classifiers. The classifiers are validated using available AirSAR data sets. Specific estimators are developed for each class on the basis of the scattering models and empirical data sets. The candidate algorithms are tested with the AirSAR data sets. The attributes of interest include: total above ground biomass, woody biomass, soil moisture and soil roughness.

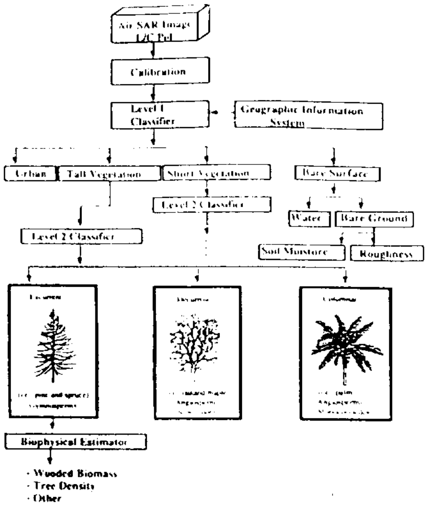

Figure 1. SAR terrain classifier

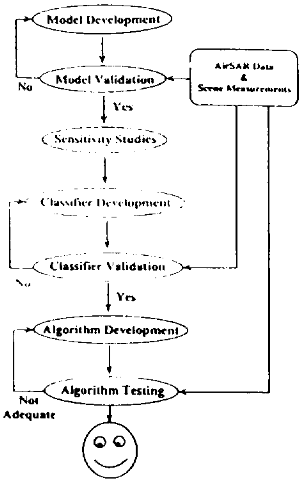

Figure 2. Development and validation process

2. LEVEL 1 CLASSIFIER

After calibration, an SAR image is classified in two stages. The Level 1 classifier operates at a pixel level to distinguish urban, tall vegetation, short vegetation and bare surfaces. The classifier has been designed for use with SIR-C/X-SAR. Hence, the data inputs are polarimetric L- and C-band data. JPL AirSAR 4-look data for Pellston, Michigan are used to train the classifier. The classifier uses: σ° (hh, vv and hv) at L- and C-bands, the peak co-polarized relative phase difference and texture. The FORTRAN classifier uses a knowledge-based, binary decision tree to differentiate the four terrain classes as shown in Figure 3. Figure 4 shows the classification of the training image. The classification accuracy is found to be in excess of 90% (see Table 1) for both the training data and independent test areas within the scene. Classifier errors generally involve assignment of short vegetation to either bare surface or tall vegetation classes. Application of the classifier to other images obtained at a SIR-C/X-SAR supersite near Raco, Michigan yield equally impressive results.

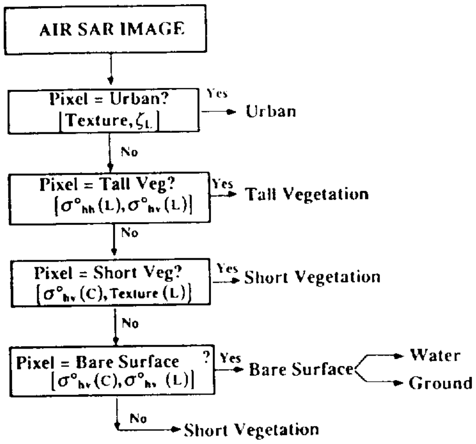

Figure 3. Level 1 classifier design

Figure 4. Classified AirSAR images from Pellston, MI. Urban = white, Tall Vegetation = light grey, Short Vegetation = dark gray, Bare surfaces = black.

Table 1. Level 1 Classifier Results

Training Areas

	True Class			
Classified As	Urban	Tall Veg	Short Veg	Bare Surface
Urban	99.3	0.22	0	0.06
Tall Veg	0	98.32	0	0
Short Veg	0.50	1.46	94.74	0.87
Bare Surface	0.20	0	5.26	99.07

Independent Test Areas

	True Class			
Classified As	Urban	Tall Veg	Short Veg	Bare Surface
Urban	99.1	0	0.85	0.01
Tall Veg	0.1	98.04	2.84	0.01
Short Veg	0.63	1.96	90.77	0.18
Bare Surface	0.17	0	5.54	99.79

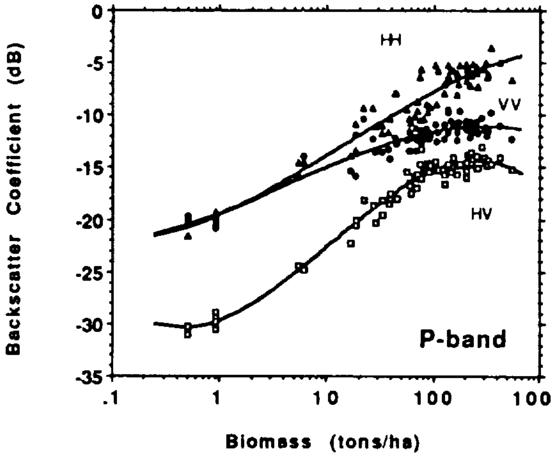

Figure 5. P-band response to forest biomass. Data from loblolly pines (Duke Forest) and maritime pines (Landes Forest).

3. LEVEL 2 CLASSIFIER

The Level 2 classifier is used to select appropriate estimator algorithms for a given pixel. It operates on the premise that multifrequency SAR is sensitive to surface and canopy structure (i.e., geometric attributes). AirSAR studies of pines at the Landes Forest in Bordeaux and the Duke Forest in North Carolina show a power-law dependence of σ° on aboveground biomass. σ° is found to saturate at biomass levels that scale with wavelength: P-band ≈ 100 tons/ha, L-band ≈ 50 tons/ha and C-band ≈ 10 tons/ha. The P-band response shown in Figure 5 indicates that biomass estimators are feasible below the saturation level. For the pine forests (excurrent tree form), AirSAR data indicates a dependence on crown structure only at C-band. Natural forests in particular are not mono-specie. Examination of AirSAR data from test sites in northern Michigan at Raco and Pellston demonstrates that the different branch and trunk structure of decurrent tree forms yield distinctive biomass relationships at long wavelengths. Hence, it is necessary to subclassify tall vegetation into distinctive SAR structural categories prior to application of estimator algorithms.

The level 2 classifier for tall vegetation is based upon model results using MIMICS, a 1st order vector radiative transfer model for closed canopies. Simulations for grass, shrubs, and excurrent and decurrent tree forms use growth models for canopies ranging from 0 to 200 tons/ha. The model yields modified Mueller matrices from which σ° and relative phase properties can be calculated for net backscatter as well as the component source terms. An example of the simulated data is shown in Figure 6.

Model results at P-, L-, and C-bands and $20^{\circ} \le \theta \le 60^{\circ}$ provide a number of potential classifiers for separation of tall vegetation into shrubs, excurrent trees and decurrent tree forms. Testing of these classifiers with mixed-specie AirSAR data from Raco and Pellston, Michigan shows the spectral gradient ($\sigma^{\circ}_{\lambda_1} - \sigma^{\circ}_{\lambda_2}$) to be a sensitive discriminant of tree form. The gradient from P-band to C-band yields the best results as shown in Figure 7. L-band is not a suitable substitute for P-band because of attenuation by the crown layer of branches and leaves.

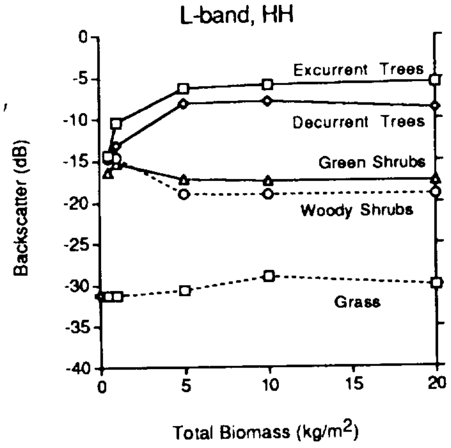

Figure 6. MIMICS simulations of backscatter from various vegetation classes at $\theta=40^{\circ}$.

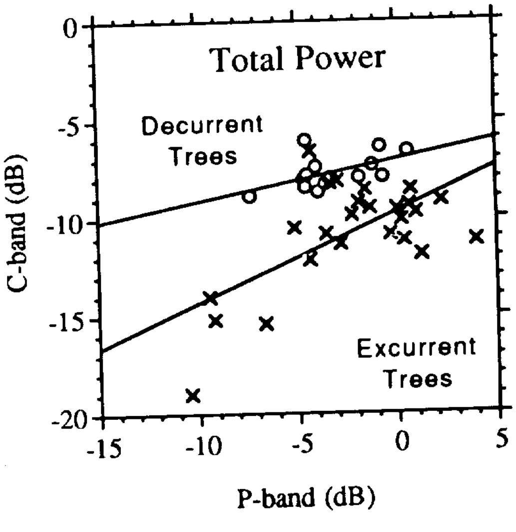

Figure 7. The spectral gradient is greater for excurrent tree forms.

4. LEVEL 2 MAPPER OF SURFACE PROPERTIES

A suite of estimator algorithms are being designed to operate on each sub-class. For vegetated regions, the algorithms yield estimates of biomass, stem density, canopy height, etc. For bare surfaces, estimator algorithms quantify surface roughness and near-surface soil moisture. The surface algorithms have been developed on the basis of truck-mounted polarimeter data. Semi-empirical formulations using polarization ratios yield estimates of surface roughness and soil permittivity. Soil moisture is inferred from permittivity. Some results of this algorithm are shown in Figure 8 for scatterometer data (Oh, 1992). Polarimetric SAR data is required and long wavelengths are preferred (i.e., P- and/or L-band).

5. CONCLUSIONS

An SAR-based terrain classifier and biophysical attribute mapper has been designed on the basis of theoretical models and empirical evidence. The level 1 and 2 classifiers take advantage of multifrequency, polarimetric SAR as a structure mapper. Tests of the classifiers on AirSAR data from two distinct sites in northern Michigan at different times of year produce excellent results.

Estimator algorithms for surface attributes have been developed and tested using scatterometer data. Evaluations of the algorithms using AirSAR data from Chickasha, OK and Davis, CA are currently underway. Estimator algorithms for canopy biophysical attributes are in development and will be tested on AirSAR data prior to the SIR-C/X-SAR launch in 1994. The classifier and estimators require polarimetric data at L- and C-bands. The addition of P-band is found to yield superior results for forested areas due to increased penetration and sensitivity to trunk attributes.

REFERENCES

Oh, Y., K. Sarabandi, and F.T. Ulaby, 1992, "An Empirical Model and an Inversion Technique for Radar Scattering from Bare Soil Surfaces," *IEEE Trans. Geo. Rem. Sens.*, vol. 30, no. 2, pp.370-381.

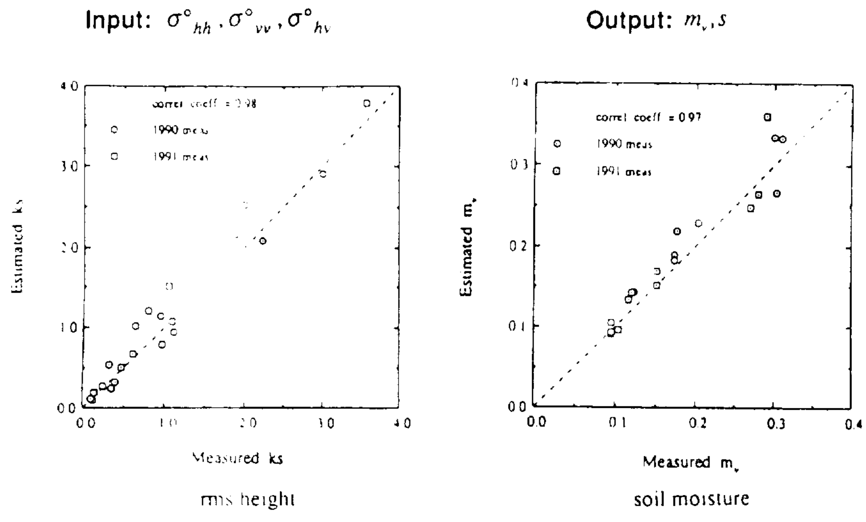

Figure 8. Results of surface estimator algorithm.

N95- 23958

Classification and Soil Moisture Determination of Agricultural Fields

A.C. van den Broek and J.S. Groot

Physics and Electronics Laboratory TNO
P.O. Box 96864, 2509 JG The Hague, The Netherlands

1 Introduction

During the Mac-Europe campaign of 1991 several SAR experiments were carried out in the Flevoland test area in the Netherlands. The testsite consists of a forested and a agricultural area with more than 15 different crop types. The experiments took place in June and July (mid to late growing season).

The area was monitored by the spaceborne C-band VV polarised ERS-1, the Dutch airborne PHARS with similar frequency and polarisation and the three-frequency (P-, L- and C-band) polarimetric AIRSAR system of NASA/JPL. The last system passed over on June 15, July 3, 12 and 28. The last two dates coincided with the overpasses of the PHARS and the ERS-1. Comparison of the results showed that backscattering coefficients from the three systems agree quite well (van den Broek and Groot, 1993).

In this paper we present the results of a study of crop type classification (section 2) and soil moisture determination in the agricultural area (section 3). For these studies we used field averaged Stokes matrices extracted from the AIRSAR data (processor version 3.55 or 3.56).

2 Classification of agricultural fields

Field averaged Stokes matrices contain five non-zero cross products (σ_{hh}=$<S_{hh}S^*_{hh}>$, σ_{vv}=$<S_{vv}S^*_{vv}>$, σ_{hv}=$<S_{hv}S^*_{hv}>$, ρ=$<S_{hh}S^*_{vv}>$), where the last cross product is complex. The $<S_{co}S^*_{cross}>$ products are zero due to azimuthal symmetry. We use here two classification methods: a Gaussian maximum likelihood (GML) method which uses the polarimetric information directly and the so-called polarimetric contrast classification (PCC) method which uses this information more indirectly. For the study of crop type classification we have selected 330 agricultural fields with 8 crop-type classes (see Table)

crop type	#fields	crop type	#fields
rapeseed	13	sugar beet	63
grass	41	corn	15
potato	86	barley	19
wheat	84	beans	9

2.1 Gaussian maximum likelihood classification

This method deals with feature vectors of arbitrary dimensionality. We can use single features as C-band σ^0_{vv} (ERS-1), full polarimetric vectors as X=(σ^0_{hh},σ^0_{vv},σ^0_{hv}, ρ) or multi-temporal vectors as X=($\sigma^0_{15/6}$,$\sigma^0_{3/7}$, $\sigma^0_{12/7}$,$\sigma^0_{28/7}$) for one particular polarisation combination. We obtain ensemble statistics for every crop-type class by calculating the mean vector μ_i=E[X$_i$] and the covariance matrix C_{ij}=E[(x$_i$-μ_i)(x$_j$-μ_j)†] with E the expectation value. Next we calculate for every field the distance function D defined by

$$D = -\frac{1}{2}\log|C| - \frac{1}{2}(X_i - \mu_i)C^{-1}_{ij}(X_j - \mu_j) \tag{1}$$

to all crop-type classes. The field is assigned to that crop-type class for which this distance is a minimum.

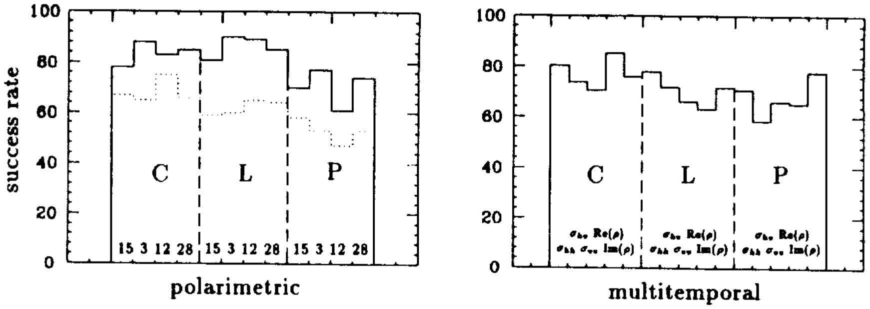

Figure 1: Classification results with the GML (full line) and PCC (dotted line) method using polarimetric (Fig. 1a, left) and multitemporal features (Fig. 1b, right).

2.2 Polarimetric contrast classification

This method was originally introduced by Kong (1990). It uses the so-called optimum contrast λ between two Stokes matrices M_a and M_b, which is defined by

$$\lambda = \frac{s^T M_a s}{s^T M_b s} \tag{2}$$

where the polarisation state of Stokes vector s is chosen such that λ is an extremum. In this method first the ensemble averages of the Stokes matrices for all crop-type classes are calculated. Then for each field we calculate the optimum contrast with all crop-type classes and the field is assigned to that class for which the optimum contrast is a minimum.

2.3 Results

Single feature classification success percentages are between 30 and 50%. Generally the σ^0_{hh} results are better than the σ^0_{vv} results. The best results are obtained for the C- and L-band σ^0_{hv} on July 3.

The C- and L-band polarimetric success percentages are on average 60% for the PCC method and 80% for the GML method (see Fig. 1a). The P-band results are significantly lower for both methods, since the backscatter of the soil dominates that of the vegetation here.

When single features of the 4 dates are combined into multi-temporal feature vectors success percentages of 70 to 80% are found (see Fig. 1b), so that it can be concluded that single day polarimetric classification is more powerful than 4 day multitemporal classification in the mid to late growing season. This situation may change when also data obtained in the beginning of the growing season is used.

3 Soil moisture determination of vegetated soil

For bare soil it is in principle possible using radar to measure the top-layer soil moisture content if the soil roughness is known, since the radar backscatter from soil primarily depends on the soil moisture content and soil roughness. However, when the soil is vegetated we have to know the transmissivity of the vegetation layer and also the relative contributions in the backscatter of the vegetation and of the soil. This information cannot be obtained from single frequency and single polarisation systems (e.g. the ERS-1), but maybe obtained from the three-frequency polarimetric AIRSAR system. Every measurement with this system delivers 15 features (5 features for each frequency band, see Sect. 2), which are certainly not all independent, so that the dimensionality of the data-set is less than 15. If the dimensionality of the data-set remains high enough, however, the information can possibly be used to solve for the different contributions in the backscatter of vegetated soil.

3.1 Description of the method

In order to extract the different contributions in the backscatter from vegetated soil we adopt the simple model of Freeman and Durden (1992, hereafter the FD model). This model transforms the polarimetric information (σ^0_{hh},σ^0_{vv},σ^0_{hv},ρ) into backscattering coefficients for diffuse, odd- and even-bounce scattering, which are related to the interaction of the microwave radiation with the vegetation, with the ground and with both the vegetation and the ground, respectively. Here we assume this is true for at least the C- and L-band. For the P-band the diffuse scattering is certainly also affected by the soil. The diffuse scattering in the model is estimated by assuming that the scatterers in the vegetation medium can be represented by uniformly oriented and distributed small dipoles (needles). The ratio of the cross- and co-polarised backscattering coefficient, which we call here the vegetation structure parameter τ, is in this case 1/3. The derived backscattering coefficient for the vegetation is directly related to this parameter.

The derived backscattering coefficient for the soil is related to the true backscattering coefficient by

$$\sigma^0_{true} = \Upsilon_f\, \sigma^0_{soil}(m_v, \sigma', f, \theta) = e^{-\alpha f}\, \sigma^0_{soil}(m_v, \sigma', f, \theta) \tag{3}$$

where Υ_f is the two-way transmissivity of the vegetation layer depending on the frequency f, σ' the soil roughness, θ the incidence angle and m_v the volumetric soil moisture content. If we assume similarly as in the FD model that the vegetation backscattering is due to uniformly oriented small needles the transmissivity is described by Υ_f=$e^{-\alpha f}$. If we have in addition an accurate model describing the backscattering coefficients of the soil as a function of the depending parameters, and if the soil roughness σ' is known Eq. (3) contains only two unknowns α and m_v. In that case we can solve for α and m_v, once the C- and L-band contributions of the soil are known from the FD model [1]. As soil model we use the empirical model of Oh et al. (1992) which is valid for incidence angles > 20° and frequencies > 1 Ghz.

During the campaign soil roughness measurements were performed for some agricultural fields with different crop types in Flevoland which are however generally valid since the soil composition and cultivation are quite homogeneous in Flevoland. We also obtained soil moisture measurements of a small number of fields for the principal crop types (potatoes, wheat, sugar beet and maize) in a part of the observed agricultural area. Since the soil for potatoes is cultivated in furrows and ridges, which is not described by the model of Oh et al. and the scattering by wheat and maize is often dominated by even bounce scattering (especially in the L-band), we choose to use sugar beet in this study. We found 22 sugar beet fields in the selected area, which were vegetated during the three July overpasses.

3.2 Results

The soil roughness σ' is estimated to be 1.2 cm. (Vissers and van der Sanden, 1993). Unfortunately, the uncertainty is rather large. Using this value for σ' we solved for m_v and α requiring that the residue is less than 0.1 dB in both the C- and L-band. In this way we obtained solutions for 7, 8 and 18 fields for July 3, 12 and 28, respectively. In Fig. 2a we show histograms of m_v, Υ_C and Υ_L for July 28. The average soil moisture content is 0.5 $\mathrm{g\,cm^{-3}}$ and the average transmissivity is 0.45 and 0.80 in the C- and L-band, respectively.

The measured soil moisture content in three sugar beet fields is about 0.25 (Vissers and van der Sanden, 1993) so that the derived value is too high, although values derived from radar measurement may be somewhat higher due to the big water-rich roots of the sugar beet plant. Also the value for the transmissivity in the C-band is rather high, since Bouman (1991) found that the vegetation layer of sugar beet in the C-band is probably opaque, so that values less than 0.3 are expected for Υ_C.

It appears that the solutions are rather sensitive to the value of the soil roughness parameter σ' and to the vegetation structure parameter τ. If we estimate this value from measurements in the C-band,

---

[1] A problem may be that the penetration depth is wavelength dependent ($\sim \lambda/3$), so that different frequencies probe different soil moisture contents. We assume here that these differences are small in this context.

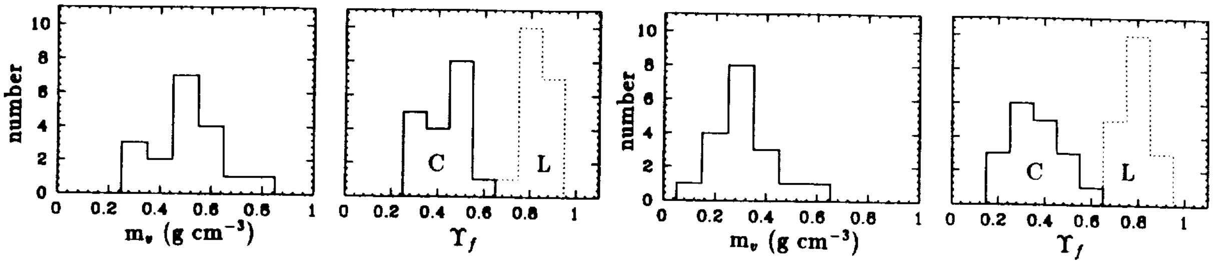

Figure 2: Histograms of m_v,Υ_C and Υ_L (July 28), for σ'=1.2 cm, τ = 1/3 (Fig. 2a, left) and σ'=1.5 cm, τ = 1/4 (Fig 2b, right).

assuming that the contribution of the vegetation dominates that of the soil (Bouman, 1991) we find values of 0.2 - 0.3 for τ, which is smaller than the value of 1/3 in the FD model. Clearly the structure of the sugar beet vegetation is also of importance and cannot simply be represented by small needle scatterers. If we now change the values for the vegetation structure parameter τ to 1/4 and the soil roughness σ' to 1.5 cm we obtain reasonable results for July 28 (see Fig. 2b).

For July 3 and 12 no solutions were obtained in most cases, since on average the C-band soil contribution in the FD model is enhanced compared to the L-band soil contribution. This situation can be explained when the vegetation structure parameter is lower for the C-band than for the L-band, which would imply that in the period between July 12 and 28 a change in the structure parameters has occurred. Indeed, measurements with the ERS-1 in 1992 show a drop in backscattering for sugar beets during this period, which is probably related to a change in the vegetation structure (Rijckenberg, private communication).

We conclude therefore that there is an addional free parameter in the FD model, which depends on the vegetation structure and probably also on the frequency. Vegetation models like MIMICS (Ulaby et al., 1990) may help to determine this parameter. Furthermore we need to know the soil roughness quite accurately in order to apply this method successfully.

4 References

(1) Bouman B.A.M., 1991, *Linking X-band Radar Backscattering and Optical Reflectance with Crop Growth Models*, Ph. D. Thesis, Univ. of Wageningen, The Netherlands

(2) Freeman A., Durden S., 1992, "Fitting a Three-component Scattering Model to Polarimetric SAR Data", *Proceedings of the Third Annual JPL Airborne Geoscience Workshop*, JPL Publication 92-14, Vol. 3, pp. 56-58

(3) Kong J.A. (Ed.), 1990, *Polarimetric Remote Sensing (PIER 3)*, Elsevier, New York, pp. 351-368

(4) Oh Y., Sarabandi K., Ulaby F.T., 1992, "An Empirical Model and an Inversion Technique for Radar Scattering from Bare Soil Surfaces", *IEEE Tr. Geo. Rem. Sens.*, vol. 30, no. 2, pp. 370-381

(5) Ulaby F.T., Sarabandi K., McDonald M.W., Dobson M.C., 1990, "Michigan Microwave Canopy Scattering model",*Int. J. Remote Sensing*, vol. 11, no. 7, pp. 1223-1253

(6) van den Broek A.C., J.S. Groot, 1993, "Intercalibration of Satellite and Airborne SAR", accepted for publication in *Canadian Journal of Remote Sensing*

(7) Vissers M.A.M., van der Sanden J.J., 1993, *Groundtruth Collection for the JPL-SAR and ERS-1 Campaign in Flevoland*, BCRS report no. 92-26.

N95- 23959

RELATING P-BAND AIRSAR BACKSCATTER TO FOREST STAND PARAMETERS

Yong Wang, John M. Melack, and Frank W. Davis

Center for Remote Sensing and Environmental Optics
University of California at Santa Barbara, Santa Barbara, CA 93106.

Eric S. Kasischke and Norman L. Christensen, Jr.

School of the Environment, Duke University, Durham, NC 27706.

1. Introduction

As part of research on forest ecosystems, the Jet Propulsion Laboratory (JPL) and collaborating research teams have conducted multi-season airborne synthetic aperture radar (AIRSAR) experiments in three forest ecosystems including temperate pine forest (Duke Forest, North Carolina), boreal forest (Bonanza Creek Experimental Forest, Alaska), and northern mixed hardwood-conifer forest (Michigan Biological Station, Michigan). The major research goals were to improve understanding of the relationships between radar backscatter and phenological variables (e.g. stand density, tree size, etc.), to improve radar backscatter models of tree canopy properties, and to develop a radar-based scheme for monitoring forest phenological changes.

In September 1989, AIRSAR backscatter data were acquired over the Duke Forest. As the aboveground biomass of the loblolly pine forest stands at the Duke Forest increased, the SAR backscatter at C-, L-, and P-bands increased and saturated at different biomass levels for the C-band, L-band, and P-band data (Dobson et al. 1992). Due to the 4-page-length limit, we only use the P-band backscatter data and ground measurements to study the relationships between the backscatter and stand density, the backscatter and mean trunk dbh (diameter at breast height) of trees in the stands, and the backscatter and stand basal area.

2. Study area and forest stand data

The tree stands used in this study are located in the Duke University Forest, which is located west of Durham, North Carolina (36° 00' N, and 79° 00' W). The Duke Forest contains forest stands with a total area of 3400 hectare, one-quarter of which are pure stands of loblolly pine, *Pinus taeda L.* These pine stands range in age from < 1 to > 100 years in age.

This forest has been the site of ongoing research focused on developing a better understanding of the potential use of imaging radars for monitoring southern U.S. pine forests. Airborne SAR data were collected over this forest in 1984 and 1989 (Kasischke and Christensen 1990, Kasischke et al. 1993a), and satellite data have collected with both the ERS-1 and JERS-1 SARs since 1991 (Kasischke et al. 1993b). This site represents one Terrestrial Ecology Supersite that will be imaged by SIR-C/X-SAR system in 1994 (Evans et al. 1993).

A total of 23 pine stands are used in this study. The densities of the pine trees in these stands range between 200 and 1844 trees/hectare. The average dbh of tree trunks in the stands ranges between 13.7 and 33.9 cm. The average tree height in the stands ranges from 11.7 to 25.6 m, and the average canopy depth from 5.3 to 9.2 m. The ground surface in the selected 23 stands is level, which minimizes topographic effects on the SAR data.

3. Results

3.1. JPL AIRSAR backscatter data

JPL AIRSAR data were acquired on 2 September 1989. The data were collected between 11:30 and 14:30, local time. The AIRSAR data were processed and calibrated by using 8 ft. (2.44 m) trihedral corner reflectors. The estimated calibration uncertainty was ± 2.0 dB for P-band (0.68 m wavelength) backscatter. The standard 4-look compressed data with pixel spacing of 12.1 m (azimuth) and 6.7 m (slant range) were provided by JPL. To compute the mean of SAR data for a stand, we located the stand on the SAR imagery, and the largest possible window within the stand was extracted. For each stand, at least 200 image pixels were averaged.

3.2. Stand density vs. P-band SAR backscatter

There is almost no relationship between the P-band backscatter and stand density (Figure 1). Of the 23 stands, as the stand density increases, tree size parameters (e.g. dbh, tree height, and canopy depth) vary irregularly (Kasischke 1992). Thus, the stand density is not a good parameter to explain the variation in the SAR backscatter.

3.3. Stand mean dbh vs. P-band SAR backscatter

As the mean trunk dbh of trees in the stands increases, the P-HH and P-HV backscatter increases. The P-HH and P-HV backscatter is saturated at stand mean dbh $\geq$ 25 cm (approximately) (Figure 2a, c). The observed increase in backscatter may be attributed to the increase of tree sizes. There is almost no relationship between the P-HV backscatter and stand mean dbh (Figure 2b).

3.4. Stand basal area vs. P-band SAR backscatter

The P-HH and P-HV backscatter increases when the stand basal areas increase. There are large variations in the HH and HV backscatter for a given stand basal area (Figure 3a, c). The P-VV backscatter show almost no trend as the stand basal area varies (Figure 3b).

4. Concluding remarks

For loblolly pine stands at the Duke Forest, there is almost no correlation between the observed AIRSAR P-HH, P-HV, and P-VV backscatter and stand density, and no correlation between the P-VV backscatter and stand mean dbh or stand basal area. The P-HH and P-HV backscatter increases as the stand mean dbh or the stand basal area increases. The complex behavior of observed P-band backscatter from the loblolly pine stands shown in this study can not be explained by a single stand parameter (such as stand density, stand mean dbh, and stand basal area). Ongoing studies on the backscatter by using forthcoming spaceborne and airborne SAR data, particularly multi-frequency, multi-angle, and multi-polarization data, and by using a theoretical canopy backscatter model coupled with the collected ground measurements (Wang et al. 1993) should help complete the picture.

5. References

Dobson, M. C., Ulaby, F. T., Le Toan, T., Beaudoin, A., Kasischke, E. S., and Christensen, Jr., N. L., 1992, Dependence of radar backscatter on coniferous forest biomass, *IEEE Trans. on Geosci. and Remote Sensing*, 30(2):412-415.

Evans, D., Elachi, C., Stofan, E. R., Holt, B., Way, J., Kobrick, M., Ottl, H., Pampoloni, P., Vogt, M., Wall, S. van Zyl, J. J., and Schier, M., 1993, The Shuttle Imaging Radar-C and X-SAR Mission, *EOS Transactions*, 74:145.

Kasischke, E. S. and Christensen, Jr., N. L., 1990, Connecting forest ecosystem and microwave backscatter models, *Int. J. of Remote Sensing*, 11:1277-1298.

Kasischke, E. S., 1992, Monitoring changes in aboveground biomass in loblolly pine forests using multichannel synthetic aperture radar data, Ph.D. dissertation, The University of Michigan, 190 pp.

Kasischke, E. S., Christensen, Jr., N. L., and Haney, E., 1993a, Modeling of geometric properties of loblolly pine tree and stand characteristics for use in radar backscatter models, *IEEE Trans. on Geosci. and Remote Sensing*, in press.

Kasischke, E. S., Christensen, Jr., N. L., Bourgeau-Chavez, L. L., and Haney, E., 1993b, Observation on the sensitivity of ERS-1 SAR image intensity to changes in aboveground biomass in young loblolly pine forests, *Int. J. of Remote Sensing*, in press.

Wang, Y., Kasischke, E. S., Davis, F. W., Melack, J. M., and Christensen, Jr., N. L., 1993, Evaluating the potential for retrieval of loblolly pine forest biomass using SAR data and a canopy backscatter model, to be submitted to *IEEE Trans. on Geosci. and Remote Sensing*.

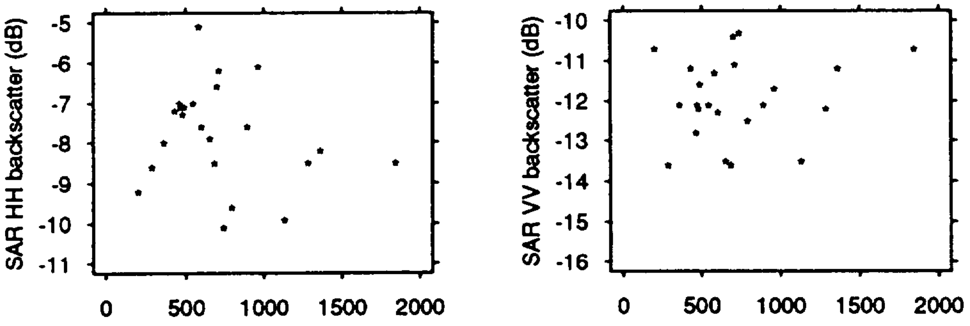

(a). Stand density (trees/ha)

(b). Stand density (trees/ha)

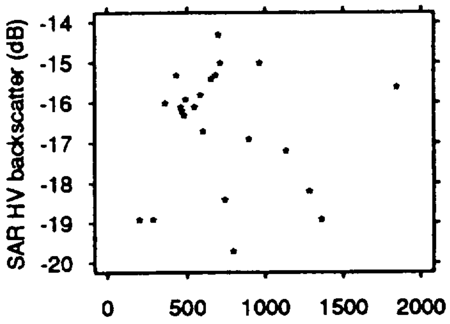

(c). Stand density (trees/ha)

Figure 1. Stand density vs. P-band SAR backscatter for loblolly pine forests at the Duke Forest

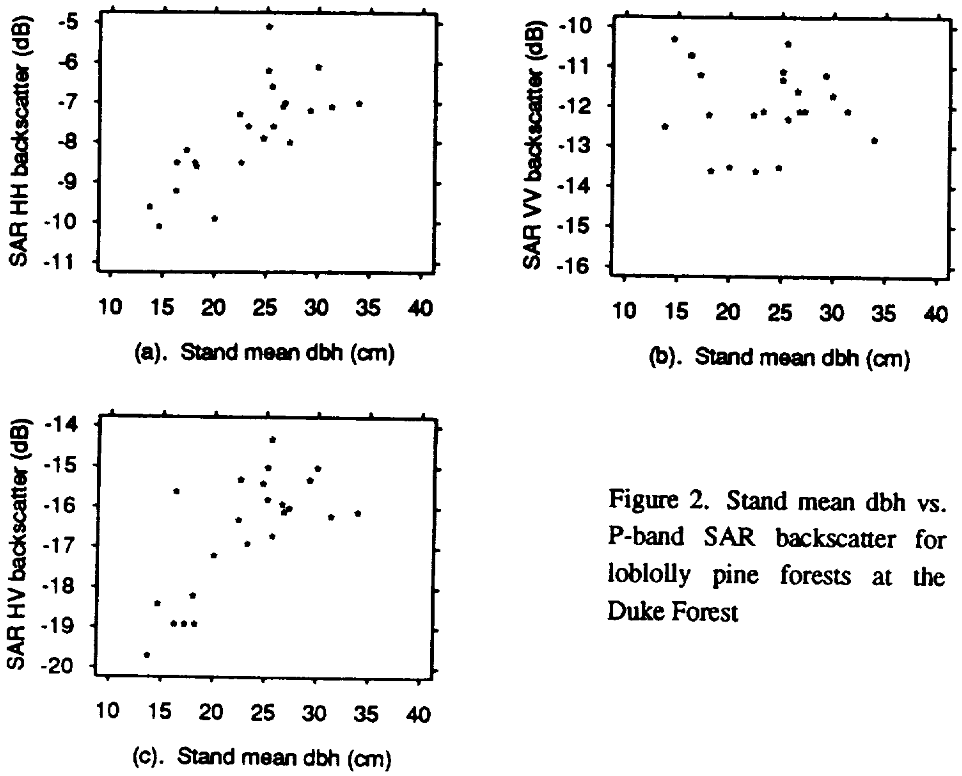

Figure 2. Stand mean dbh vs. P-band SAR backscatter for loblolly pine forests at the Duke Forest

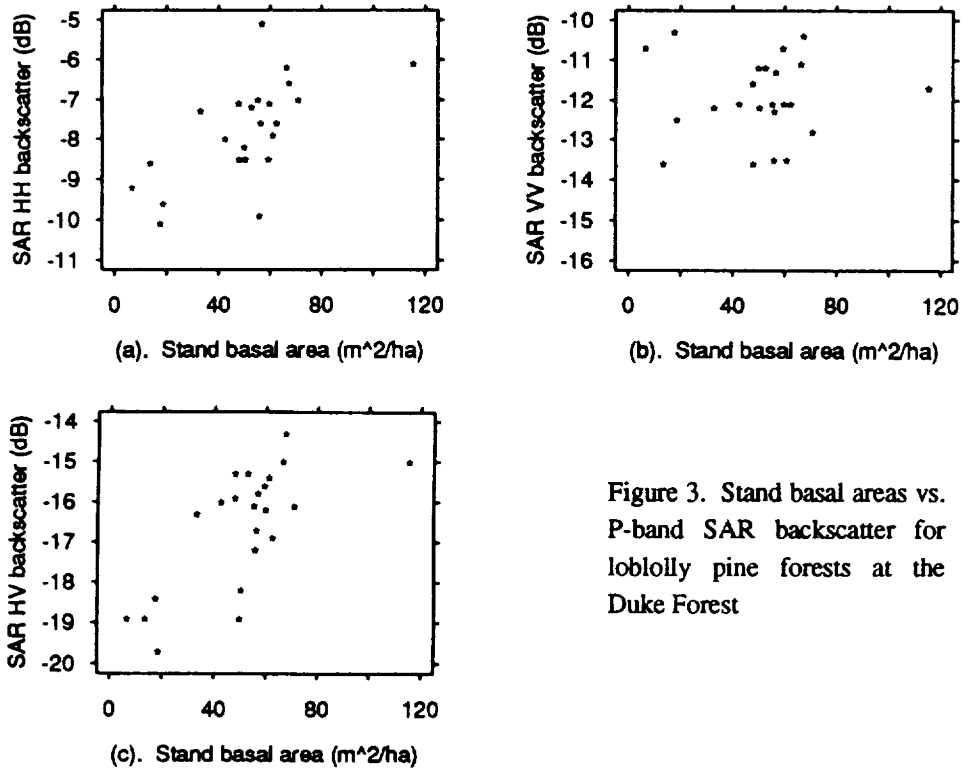

Figure 3. Stand basal areas vs. P-band SAR backscatter for loblolly pine forests at the Duke Forest

N95- 23960

SOIL MOISTURE RETRIEVAL IN THE OBERPFAFFENHOFEN TESTSITE USING MAC EUROPE AIRSAR DATA

Tobias Wever & Jochen Henkel

Department for General and Applied Geology
Working Group for Remote Sensing
80333 Munich, Germany

1. INTRODUCTION

Soil moisture content is an important parameter in many disciplines of science like hydrology, meteorology, agriculture and others. Microwave remote sensing technique has a high potential in measuring the dielectric constant of soils, which is strongly governed by the soil moisture (Ulaby et al. 1982). Much excellent work has been done on investigating the relationship between backscattering coefficient and soil moisture (Schmugge et al. 1980, Ulaby et al. 1986, Dobson et al. 1985, Rao et al. 1992, Shi et al. 1992). Most of these studies are measured in a laboratory or are carried out with a multitemporal data set. This means, that the variation in the backscattering coefficient is only related to the soil moisture because all other parameters influencing the backscattering like surface roughness, vegetation cover, plant geometry, phenology of plants and row direction are kept constant. In this study the sensitivity of the backscattering coefficient to soil moisture of corn fields is investigated. In the framework of the MAC-Europe Campaign in June 1991, the NASA/JPL three-frequency polarimetric AIRSAR system collected data over the test site Oberpfaffenhofen (Germany). The AIRSAR campaign in Oberpfaffenhofen was complemented with intensive ground truth measurements. The sampled corn fields are nearly in the range of the same incidence angle (≈20°) and belong to different soil types. The evaluation was carried out at a single data set. The results show, that the backscattering, measured at P-band can be described with only two parameters very well. The main parameter, influencing the backscattering is the soil moisture content, the second subordinated parameter is the row direction.

2. ANALYSES AND RESULTS

For the assessment of the AIRSAR data for soil moisture retrieval all frequencies (C-, L- and P-band) were investigated. Also different polarizations and processing steps were used. Multiparameter least square regression analysis was carried out to fit the values of soil moisture (grav. % and vol. %) with these (σ°) of the AIRSAR system. The objective was to identify the best frequency and polarization respectively the best processing steps for soil moisture retrieval over corn fields. 17 corn fields with different SMC and different row directions relative to the look direction have been sampled. All fields are placed within a range with a similar incidence angle near 20 degrees to avoid effects referring to the incidence angle. To get different SMC's, the cross section of sampled fields covers three different types of soils: a loess soil, a waste gravel soil upon glacial gravel terraces and a drained ground-water soil. One problem is the spatial registration of the SMC on the ground. Due to the fact, that only point measurements of SMC are possible, the accuracy of the ground acquisition of SMC depends on the quantity of measurements.

The backscattering coefficient at C-band is mainly influenced by the interaction between the incident wave and the vegetation cover, which is expressed by the good perceptibility of the land use. The row direction takes no measurable effects and the differences in the soil moisture are masked from the vegetation cover.
The same investigations were done for the L-band at all polarization combinations. Also at this frequency the backscattering coefficient is mainly influenced by the differences in the vegetation cover. However the canopy loss is smaller, which is expressed by the week perceptibility of soil boundaries representing differences in soil moisture content. The same is valid for the row direction tracing weekly on fields with the same vegetation cover, in this case corn.

Summarized it can be said that at L- and especially at C-band and an incidence angle of approximate 20° the attenuation coefficient of vegetation canopies is to high for monitoring soil moisture without modelling.
Our measurements with P-band look very promising. The attenuation coefficient of vegetation canopy is relative small, because now the soil moisture is the dominant part influencing the backscattering (fig. 2). The second subordinated parameter is the row direction (tab. 1). A multiparameter least square regression analysis with the parameters row direction, soil moisture content and the backscattering coefficient was carried out. Figure 1 shows, that 92% of the backscattering can be described with the parameter row direction and gravimetric SMC at HH-HV polarization and with HH polarization 90% of the backscattering. Table 1 illustrates the composition of the total backscattering referring to the difference of HH-HV polarization. It can be seen, that the main part of the signal can be counted back to the SMC. To get the single least square fit for gravimetric SMC the fields have to be calibrated to one fixed row direction (in this case 45°). Figure 4 shows the linear least square fit between gravimetric SMC and σ° at HH-HV polarization. The correlation coefficient of the relative to the row direction corrected data amounts to 0.83 at HH- respectively 0.85 at HH-HV polarization. Figure 3 demonstrates the linear dependence of row direction and the backscattering coefficient.
A comparison of the correlation coefficients illustrates the improvement taking a nonlinear fit. The decreasing slope in the region of lower SMC concerning the nonlinear fit might be derived from the effects of bound water (fig. 5, tab. 2).

Fairly extensive studies demonstrate that the volumetric SMC represents the dielectric properties of different soils better than the gravimetric SMC (e.g. Scott & Smith 1992). This study apparently do not confirm this thesis, but this effect might be derived from the little number of sampled fields referring to a statistical approach and the greater inaccuracy in measurement of the volumetric SMC on the ground due to the small sample volume (100 cm^3) we have used (fig. 6).
The dotted lines in the figures are representing the average standard deviation of the ground measurements.

A approach was carried out to detect the row direction automatically. With the correlation coefficient between the HH and VV polarization there is a parameter for the assessment of the row direction. For corn fields the influence of the row direction is one order higher at VV polarization as for other polarizations. This is caused by the strong interaction between the incidence wave and the vertical corn stalks. These interactions depend on the row direction, because the spacing between corn plants within a row is much smaller than the spacing between the rows of corn. At HH polarization the influence of row direction is smaller and shows a more linear dependance. These results are corresponding with a similar study of Brunfeldt & Ulaby (1984). The regression between the correlation coeffizients of HH- and VV polarization and the row direction for each field was calculated. The correlation coefficient of this regression amounts to 0.67. Using this regression line the angle between the row direction and the look direction can be assessed. A multiparameter least square regression analysis was carried out taking the parameters calculated row direction, grav. SMC and the backscattering coefficient of HH-HV polarization. The correlation coefficient amounts to 0.79 which means that about 80% of the backscattering can be described without complex modelling of the vegetation cover only by the data itself. Taking into account a relative great insecurity represented by the measurements of the SMC on the ground these results suggest that for soil moisture retrieval from SAR imagery P-band is very suitable using HH- or HH-HV polarization. With the two parameters soil moisture and known row direction about 90% respectively 80% of the total backscattering can be described depending on the use of gravimetric- or volumetric SMC. Further investigations have to be done to confirm these results with other plant canopies. Supposing that the influence of row direction is very high at corn due to the marked differences in spacing between corn plants within a row and the spacing between the rows of corn, soil moisture retrieval with P-band is promising even better results about other land use canopies, especially at smaller incidence angles because the influence of row direction becomes smaller.

3. REFERENCES

Brunfeldt D. R. & F. T. Ulaby (1984), "The Effect of Row Direction on the Microwave Emission from Vegetation Canopies," IGARSS Symposium, Strasbourg, 27-30 Aug.

Dobson M. C., F. T. Ulaby, M. T. Hallikainen and M. A. El Rayes (1985), "Microwave Dielectric Bahavior of Wet Soils - Part II: Dielectric Mixing Models," IEEE Transactions on Geoscience and Remote Sensing, Vol. GE-23, No. 1.

Rao K. S., W. L. Teng and J. R. Wang (1992), "Processing of Polarimetric SAR Data for Soil Moisture Estimation over Mahantango Watershed Area," Summaries of the Third Annual Geoscience Workshop, JPL Publication 92-14, Vol. 3.

Schmugge T. J., T. J. Jackson and H. L. McKim (1980), "Survey of Methods for Soil Moisture Determination," Water Resources Research, Vol. 16, No. 6.

Scott W. R. & G. S. Smith (1992), "Measured Electrical Constitutive Parameters of Soils as Functions of Frequency and Moisture Content," IEEE Transaction on Geoscience and Remote Sensing, Vol. 30, No. 3.

Shi J., J. J. van Zyl and E. T. Engman (1992), "Evaluation of Polarimetric SAR Parameters for Soil Moisture Retrieval," Summaries of the Third Annual Geoscience Workshop, JPL Publication 92-14, Vol. 3.

Ulaby F. T.,R. K. Moore and A. K. Fung (1982), "Microwave Remote Sensing: Active and Passive," Vol. II, Addison-Wesley, Readings, M. A.

Ulaby F. T.,R. K. Moore and A. K. Fung (1986), "Microwave Remote Sensing: Active and Passive," Vol. III, Artech House, Norwood, M. A.

field	row direction (degrees)	soil moisture (grav. %)	influence of soil moisture (dB)	influence of row direction (dB)	residue (dB)
1	35	17,34	7,70	2,05	0,81
2	23	14,91	6,62	1,35	0,83
3	23	13,61	6,04	1,35	0,65
4	15	15,83	7,03	0,88	0,61
5	45	15,66	6,96	2,64	1,20
6	66	16,39	7,28	3,87	0,45
7	75	20,54	9,12	4,40	1,57
8	75	20,27	9,00	4,40	0,26
9	75	20,54	9,12	4,40	0,08
10	4	20,57	9,14	0,23	0,80
11	80	21,09	9,37	4,69	1,38
12	32	15,93	7,08	1,88	2,39
13	40	22,3	9,90	2,35	0,01
14	5	26,78	11,89	0,29	1,59
15	28	21,81	9,69	1,64	1,03
16	73	27,58	12,25	4,28	0,19
17	27	23,11	10,26	1,58	1,36

Table 1. Composition of the total backscattering at HH-HV polarization.

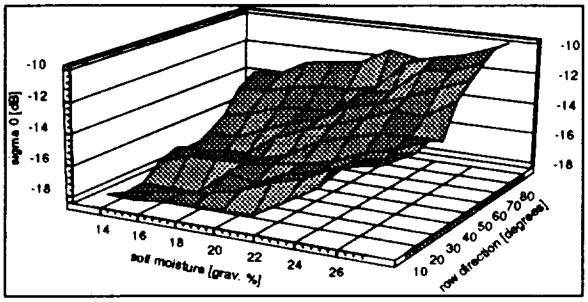

Fig. 1. Multiple linear regression for HH-HV polarization.

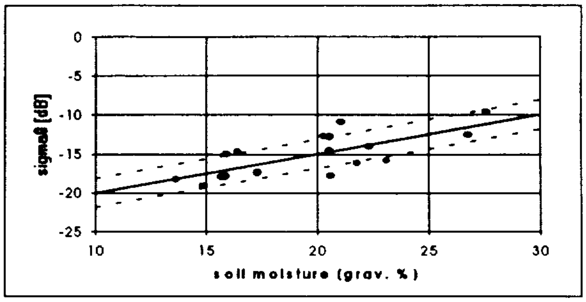

Fig. 2. Linear regression for HH-HV polarization.

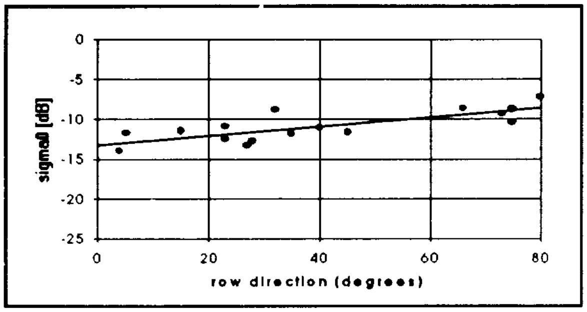

Fig. 3. Linear regression of row direction relative to the look direction versus σ° at HH-HV polarization after calibration to one fixed SMC.

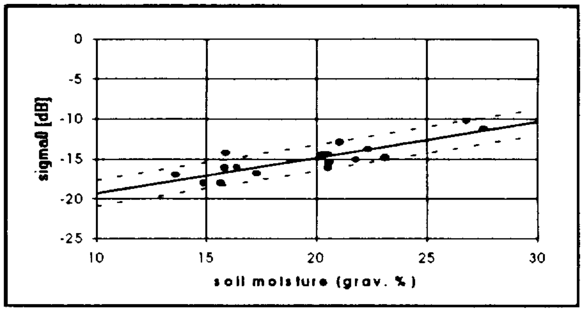

Fig. 4. Linear regression of grav. SMC versus σ° at HH-HV polarization after calibration to one fixed row direction (45°).

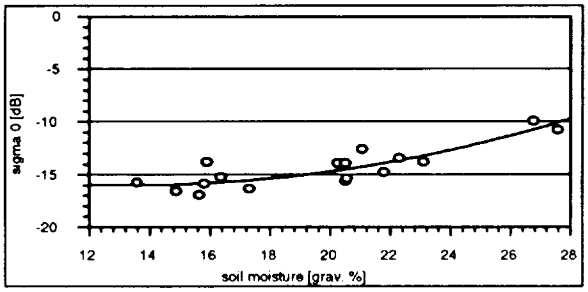

Fig. 5. Nonlinear regres. of grav. SMC versus σ° at HH polarization after calibration to one fixed row direction (45°).

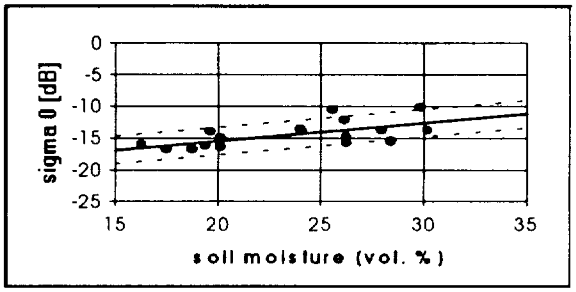

Fig. 6. Linear regres. of vol. SMC versus σ° at HH-HV polarization after calibration to one fixed row direction (45°).

data (P-band)	linear regression			nonlinear regression	multible linear regression		
	grav. %	vol. %	row direction	grav. %	grav.% / row d.	vol.% / row d.	grav.% / calc. row d.
HH	0.73	0.65	0.64	x	0.90	0.79	0.80
HH-HV	0.73	0.68	0.66	x	0.92	0.82	0.79
HH (calibrated)	0.83	0.64	0.77	0.89	x	x	x
HH-HV (calibrated)	0.85	0.69	0.80	0.87	x	x	x

Table 2. Correlation coefficients of the linear and nonlinear regression analyses.

N95- 23961

MICROWAVE DIELECTRIC PROPERTIES OF BOREAL FOREST TREES

G. Xu, F. Ahern
Canada Centre for Remote Sensing
588 Booth Street, Ottawa, Canada K1A 0Y7
J.Brown
Dendron Resource Survey Ltd.
880 Lady Ellen Place, Suite 206, Ottawa, Canada K1Z 5L9

INTRODUCTION

The knowledge of vegetation dielectric behaviour is important in studying the scattering properties of the vegetation canopy and radar backscatter modelling. Until now, a limited number of studies (Dobson et al., 1989, Hess et al., 1990, McDonald et al., 1992, Lang et al., 1993) have been published on the dielectric properties in the boreal forest context. This paper presents the results of the dielectric constant as a function of depth in the trunks of two common boreal forest species: black spruce and trembling aspen, obtained from field measurements. The microwave penetration depth for the two species is estimated at C, L and P bands and used to derive the equivalent dielectric constant for the trunk as a whole. The backscatter modelling is carried out in the case of black spruce and the results are compared with the JPL AIRSAR data. The sensitivity of the backscatter coefficient to the dielectric constant is also examined.

DIELECTRIC MEASUREMENT AND OBSERVATION

The dielectric measurements of the black spruce and trembling aspen were carried out during the June of 1990 at the experimental forests of Petawawa National Forest Institute (PNFI), Ontario, Canada. The experiment was part of the SAR-boreal project initiated at the Canada Centre for Remote Sensing in 1988 in preparation for operational RADARSAT applications in forestry. The portable dielectric probe (PDP) of Applied Microwave was used for these measurements. The dielectric measurements were made on the standing trees by incrementlly boring into the trunk and obtaining the samples of the relative dielectric constant at each depth. The measurement proceeds along the radial axis from the outer bark to the centre of tree trunks at the breast height of the tree (1.3 meters from ground).

Figures 1 shows the profiles of real part of the relative dielectric constant inside the trunk of black spruce and aspen at C, L and P bands respectively. The imaginary part is found to have high linear correlation with the real part of the dielectric constant in general and is not illustrated here due to the space limitation. It is seen that the dielectric constant peaks near the cambium layer and is much lower in both the outer bark and sapwood regions. The heartwood region of the aspen displays a higher dielectric constant than in the sapwood region, which is consistent with the field observation that the heartwood region of aspen is often found to contain significantly more moisture content than in the sapwood region. The dielectric profiles fluctuate, reflecting the inhomogeneity of the medium.

PENETRATION DEPTH AND EQUIVALENT DIELECTRIC CONSTANT

Depending on the microwave penetration depth and the physical size of the tree components such as the branches and trunks, the microwave interacts with the portion or the whole of these vegetation materials. It is therefore necessary to consider the microwave penetration depth at different frequencies and incorporate it into the derivation of the equivalent dielectric constant of different tree components for the radar backscatter modelling.

The microwave penetration depth is estimated using the formula (Ulaby et al., 1986, Pg.2019):

$$\delta = \frac{1}{2\alpha} = \frac{c}{4\pi f \mid Im\sqrt{\epsilon' - j\epsilon''} \mid} \qquad (1)$$

where α is the absorption constant of the medium, c is the speed of the light, f is the microwave frequency, ϵ' and ϵ'' are the real and imaginary part of the equivalent dielectric constant of the medium.

As a first approximation to the equivalent dielectric constant, the measured trunk moisture content of trunk wood samples of two species together with the corresponding dry density (Gonzalez, 1990) are input to the dual dispersion dielectric model developed by Ulaby and El-Rayes (Ulaby et al., 1987) to derive the equivalent dielectric constant for these species. Table 1 lists the calculated dielectric constant at C, L and P bands. These dielectric constants are then substituted into the Eqn.1 to obtain the estimated microwave penetration depth, as is shown in Table 1.

Since the power of an electromagnetic plane wave inside a lossy medium decays at a rate of $e^{-2\alpha r}$ where r is the distance from the surface of the medium, we compute the equivalent dielectric constant of the tree trunk with the microwave power decay rate as a weighing factor, that is:

$$< \epsilon > = \frac{\int \epsilon(r) e^{-2\alpha r} dr}{\int e^{-2\alpha r} dr} \qquad (2)$$

where the integral is taken from the bark surface to the centre of the trunk. Applying Eqn.2 to the sampled dielectric profile, we obtain the equivalent weighted dielectric constant. This is illustrated in Table 1.

BACKSCATTER MODELLING AND SENSITIVITY ANALYSIS

An example is given here to illustrate the effect on the radar backscatter with the dielectric constant derived from two different approaches, namely the dielectric model and the PDP sampled data. The Michigan Microwave Canopy Scattering (MIMICS) model (Ulaby et al., 1990) is applied to a typical black spruce stand in the Canadian boreal forest environment. Table 2 shows the backscatter coefficients predicted from the MIMICS model and obtained from the JPL AIRSAR data which were acquired in May, 1991 over the boreal forest test site near Whitecourt, Alberta. Despite the different approaches in deriving the dielectric constant, the results show a very good agreement in the predicted backscatter coefficient, with a discrepancy within one dB for like polarization and less than two dB for the cross polarization for all three microwave frequency. The predicted backscatter coeffcients agree exceptionally well with the SAR observation at C band, in particular with the dielectric constant derived based on the microwave penetration depth. The MIMICS model, however, is seen to over-predict the backscatter coefficient for like polarization at L band and under-predict the backscatter coeffcient for cross polarization at L and P bands, which is presumably caused by the fact that the MIMICS model does not account for the multiple (triple and over) scattering mechanisms in the computation of the backscatter coefficient.

Table 3 illustrate the effect of the dielectric constant on the backscatter coefficient. The dielectric constant of the black spruce is perturbed by 10 percent and the corresponding change in the predicted backscatter coefficient is calculated. It shows that the backscatter is more sensitive to the change in dielectric constant for like polarization at C band than at L and P bands. Among two like polarizations at C band, the backscatter is more sensitive to the change in dielectric constant for HH polarization than for VV polarization.

ACKNOWLEDGMENTS

The authors wish to thank I.MacRae, J.Drieman, C.Skelly, D.Leckie, S.Yatabe and B.Rice for assisting the dielectric measurements.

REFERENCES

Dobson, M.C., McDonald, K., Ulaby, F.T. 1989. Modeling of Forest Canopies and Analysis of Polarimetric

SAR data. **ERIM Contract Report**, No:211000-1

Gonzalez, J.S. 1990. Wood Density of Canadian Tree Species. **Information Report NOR-X-315, Northern Forestry Centre, Forestry Canada**

Hess, L. and Simonett, S. 1990. Dielectric Properties of Two Western Coniferous Tree Species. **Proc. of IGARSS' 90 Symposium**, p.503

Lang, R.H., Landry, R., Kilic, O., Chauhan, N., Khadr, N., Leckie, D. 1993. Effect of Species Structure and Dielectric Constant on C-band Forest Backscatter. **Proc. of IGARSS'93 Symposium**

McDonald, K.C., Zimmermann, R., Way, J. 1992. An Investigation of The Relationship Between Tree Water Potential and Dielectric Constant. **Proc. of IGARSS' 92 Symposium**, pp.523-525

Ulaby, F.T., Moore, R.K., Fung, A.K. 1986. Microwave Remote Sensing, Vol.III. **Artech House, Inc.**

Ulaby, F.T., El-Rayes, M. 1987. Microwave Dielectric Spectrum of Vegetation-Part II: Dual-Dispersion Model. **IEEE Trans. on Geoscience and Remote Sensing**, Vol.GE-25,5:550-557

Ulaby, F.T., Sarabandi, K., McDonald, K., Whitt, M., Dobson, M. 1990. Michigan Canopy Scattering Model. **Int. J. Remote Sensing**, Vol.11, 7:1223-1253

Band	Spruce Mg.=0.31 Dry D.=0.46		Aspen Mg.=0.43 Dry D.=0.42	
C	Penetration Depth=0.86 cm		Penetration Depth=0.71 cm	
	ε_1=10.65-j3.47	ε_2=17.14-j6.06	ε_1=15.50-j5.03	ε_2=14.42-j5.08
L	Penetration Depth=3.06 cm		Penetration Depth=2.63 cm	
	ε_1=13.31-j4.59	ε_2=14.05-j4.10	ε_1=18.88-j6.35	ε_2=14.77-j3.78
P	Penetration Depth=6.08 cm		Penetration Depth=4.89 cm	
	ε_1=15.80-j7.10	ε_2=15.10-j3.64	ε_1=21.89-j10.4	ε_2=17.71-j4.75

Table 1. The estimated microwave penetration depth and equivalent dielectric constant of black spruce and trembling aspen tree trunks.

Mg.: the gravimetric moisture content (%)

Dry D.: dry density (g/cm^3)

ε_1: the equivalent trunk dielectric constant predicted from the dielectric model

ε_2: the equivalent trunk dielectric constant derived from the PDP measurement

BAND	$\sigma^\circ(\varepsilon_1)$	$\sigma^\circ(\varepsilon_2)$	AIRSAR
C-HH	-9.38	-8.59	-8.85
C-VV	-8.79	-9.24	-9.97
C-HV	-16.46	-16.52	-15.33
L-HH	-2.49	-1.81	-8.6
L-VV	-8.69	-8.04	-12.33
L-HV	-24.48	-22.77	-16.52
P-HH	-5.43	-6.00	-9.16
P-VV	-13.39	-13.70	-12.75
P-HV	-28.87	-27.31	-18.22

Table 2. The backscatter coefficient (in dB) predicted with MIMICS model and obtained from AIRSAR observation for black spruce stand.

Band	$\sigma^\circ(\varepsilon_1)$	$\Delta\sigma^\circ(+10\%\varepsilon_1)$	$\Delta\sigma^\circ(-10\%\varepsilon_1)$
C-HH	-9.38	-0.71	0.88
C-VV	-8.79	-0.32	0.39
C-HV	-16.46	0.01	-0.06
L-HH	-2.49	-0.17	0.14
L-VV	-8.69	0.09	-0.14
L-HV	-24.48	0.82	-0.91
P-HH	-5.43	0.29	-0.16
P-VV	-13.39	0.37	-0.24
P-HV	-28.87	0.31	-0.19

Table 3. **The sensitivity of backscatter coefficient to the change in dielectric constant. The dielectric constant is pertubed 10 percent and the corresponding backscatter change (in dB) is shown.**

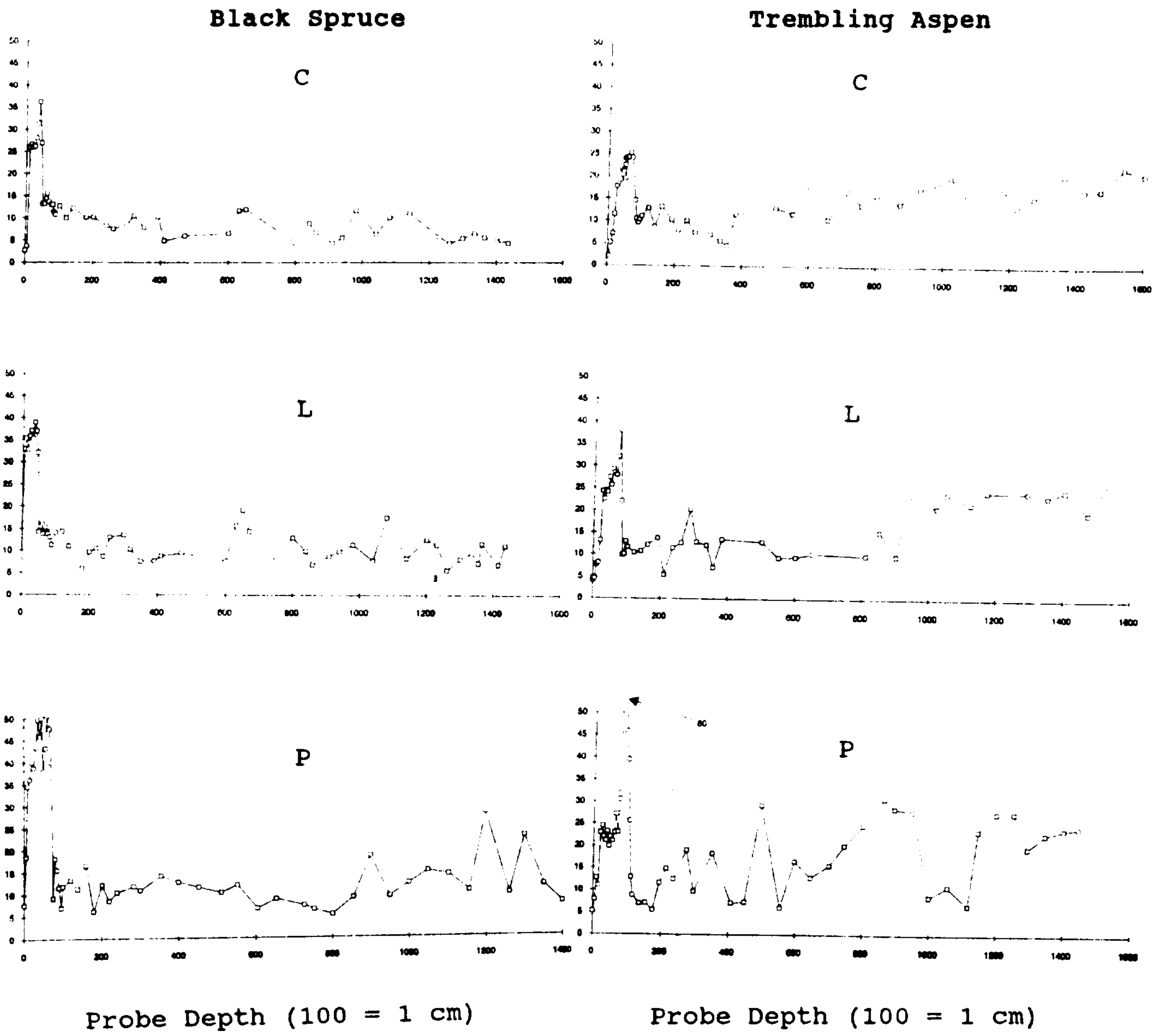

Figure 1. Dielectric profiles (real part) of black spruce and trembling aspen tree trunks. The vertical scale is the real part of PDP sampled dielectric constant.

SLIDE CAPTIONS

Slide No.	Caption	Senior Author
1	3-component RGB image of the study area; AVIRIS data collected in August 1990. Blue = AVIRIS band 12; green = band 48; red = band 213.	Beratan
2	Jasper Ridge example: The five endmember spectra and their corresponding abundance images.	Boardman
3	Color composites of the simulated and actual TM scenes.	Kalman
4	Selected linear spectral unmixing results for both the empirical line and atmospheric-model calibrated data.	Kruse
5	Classification map, produced by a self-organizing ANN.	Merényi
6	A two-band image showing the spatial relationship between the derived lignin and water fractions across the site.	Wessman
7	(A) shows the composite rendered on the digital elevation model with tags (B–E) for the location of the enlarged subareas of the horizontal (non-rendered) composite. (B)–(E) show zoom-up (≈factor 5) parts with different aspect and slope angles.	Meyer
8	Fractional abundance images and associated spectra of semi-arid landscape endmembers, August 7, 1990.	Yuhas
9	AVIRIS image cube of Rogers Dry Lake, CA, calibration site.	Green
10	AVIRIS image cube of Moffett Field, CA, data set showing San Francisco Bay and Moffett Field runways.	Green
11	The classified June 2nd image next to a vegetation map (mapped in the field) for comparison.	Sabol, Jr.
12	AIRSAR views of Aeolian terrain.	Blumberg